AN EXPERIMENTAL INVESTIGATION OF THE EFFECTS OF MASSIVE FILM COOLING ON THE AERODYNAMICS OF A TURBINE AIRFOIL

James Edward Hartsel

Ohio State University Research Foundation
Columbus, Ohio

August 1970

AN EXPERIMENTAL INVESTIGATION OF THE EFFECTS OF MASSIVE FILM COOLING ON THE AERODYNAMICS OF A TURBINE AIRFOIL

JAMES EDWARD HARTSEL

THE OHIO STATE UNIVERSITY
RESEARCH FOUNDATION
COLUMBUS, OHIO

AUGUST, 1970

CONTRACT F33615-69-C-1004

AIR FORCE AERO PROPULSION LABORATORY
AIR FORCE SYSTEMS COMMAND
WRIGHT-PATTERSON AIR FORCE BASE, OHIO

Unclassified

Security Classification

DOCUMENT CONTROL DATA - R & D

(Security classification of title, body of abstract and indexing annotation must be entered when the overall report is classified)

1. ORIGINATING ACTIVITY (Corporate author)	2a. REPORT SECURITY CLASSIFICATION
The Ohio State University Research Foundation 1314 Kinnear Road Columbus, Ohio 43212	Unclassified
	2b. GROUP N/A

3. REPORT TITLE

An Experimental Investigation of the Effects of Massive Film Cooling on the Aerodynamics of a Turbine Airfoil

4. DESCRIPTIVE NOTES (Type of report and inclusive dates)

Final Report - August 1, 1968 through January 31, 1970

5. AUTHOR(S) (First name, middle initial, last name)

James E. Hartsel

6. REPORT DATE	7a. TOTAL NO. OF PAGES	7b. NO. OF REFS
August 1970	172	20

8a. CONTRACT OR GRANT NO.	9a. ORIGINATOR'S REPORT NUMBER(S)
F33615-69-C-1004 b. PROJECT NO.	
c.	9b. OTHER REPORT NO(S) (Any other numbers that may be assigned this report) AFAPL-TR-70-47
d.	

10. DISTRIBUTION STATEMENT

Approved for public release; distribution unlimited

11. SUPPLEMENTARY NOTES	12. SPONSORING MILITARY ACTIVITY
	Air Force Aero Propulsion Laboratory Wright-Patterson Air Force Base, Ohio 45433

13. ABSTRACT

The effects of massive film cooling through multiple rows of discrete holes on the aerodynamics of a typical two-dimensional turbine airfoil have been studied experimentally using a single blade positioned in a contoured channel. The channel walls, shaped to simulate the presence of adjacent airfoils in a cascade, were both porous and movable to allow adjustment of the flow direction and airfoil surface pressure. Electrically heated air was used as the primary flow, while room temperature coolant air was emitted from five rows of discrete holes on each airfoil surface to film cool the regions aft of mid-chord. Hole geometries angled in the spanwise, chordwise, and vertical directions were employed to achieve coolant-to-inlet mass flow rate ratios as high as 0.05 for blowing from the single blade. Measurements were made of the static pressure distributions, wake total pressure defects, and airfoil suction surface temperatures. The no-blowing heat transfer to the airfoil surfaces were also obtained experimentally, using a transient thin-skin thermometry technique.

The results show that suction surface blowing causes both loss of lift and increased wake momentum losses by enlargement of the turbulent boundary layer in the region of positive pressure gradient, but no significant effect was observed for pressure surface mass addition. At low blowing rates all geometries tested gave nearly equal losses, but as suction surface blowing was increased the superiority of the 30° chordwise angular orientation was apparent. Evidence was also found that 30° spanwise angled injection may be helpful in reducing losses at high blowing rates, but not to the extent of the reduction observed for chordwise injection. Measured total pressure losses agree reasonably well with the prediction of a simple mixing analysis based on momentum conservation.

The present film-cooling effectiveness results show that discrete hole film cooling is considerably less effective than continuous slot injection, falling 0.25 to 0.45 below the continuous slot value of film cooling effectiveness η. No relative cooling superiority could be found for any particular blowing hole geometry. The results indicate that, for the type of film cooling application examined, the amount of coolant rather than the blowing hole geometry is the primary parameter governing cooling effectiveness.

DD FORM 1 NOV 65 1473

Unclassified

Security Classification

14 KEY WORDS	LINK A		LINK B		LINK C	
	ROLE	WT	ROLE	WT	ROLE	WT
Massive film cooling						
Discrete holes						
Two-dimensional turbine airfoil						
Surface pressure						
Mass flow rate ratios						
Heat transfer						
Thermometry						
Turbulent boundary layer						

AN EXPERIMENTAL INVESTIGATION OF THE EFFECTS OF MASSIVE FIIM COOLING ON THE AERODYNAMICS OF A TURBINE AIRFOIL

James Edward Hartsel

ic

ABSTRACT

The effects of massive film cooling through multiple rows of discrete holes on the aerodynamics of a typical two-dimensional turbine airfoil have been studied experimentally using a single blade positioned in a contoured channel. The channel walls, shaped to simulate the presence of adjacent airfoils in a cascade, were both porous and movable to allow adjustment of the flow direction and airfoil surface pressure. Electrically heated air was used as the primary flow, while room temperature coolant air was emitted from five rows of discrete holes on each airfoil surface to film cool the regions aft of mid-chord. Hole geometries angled in the spanwise, chordwise, and vertical directions were employed, to achieve coolant-to-inlet mass flow rate ratios as high as 0.05 for blowing from the single blade. Measurements were made of the static pressure distributions, wake total pressure defects, and airfoil suction surface temperatures. The no-blowing heat transfer to the airfoil surfaces were also obtained experimentally, using a transient thin-skin thermometry technique.

The results show that suction surface blowing causes both loss of lift and increased wake momentum losses by enlargement of the turbulent boundary layer in the region of positive pressure gradient, but no significant effect was observed for pressure surface mass addition. At low blowing rates all geometries tested gave nearly equal losses, but as suction surface blowing was increased the superiority of the 30° chordwise angular orientation was apparent. Evidence was also found that 30° spanwise angled injection may be helpful in reducing losses at high blowing rates, but not to the extent of the reduction observed for chordwise injection. Measured total pressure losses agree reasonably well with the prediction of a simple mixing analysis based on momentum conservation.

The present film-cooling effectiveness results show that discrete hole film cooling is considerably less effective than continuous slot injection, falling 0.25 to 0.45 below the continuous slot value of film cooling effectiveness η. No relative cooling superiority could be found for any particular blowing hole gemoetry. The results indicate that, for the type of film cooling application examined, the amount of coolant rather than the blowing hole geometry is the primary parameter governing cooling effectiveness.

ACKNOWLEDGMENTS

The author wishes to express his appreciation to the following members of the faculty and staff of The Ohio State University Aeronautical and Astronautical Research Laboratory: Drs. John D. Lee and Robert M. Nerem, for their advice and encouragement; Mr. Frank B. Kroeger, for lending his electronic expertise to the instrumentation of the experimental program; Mr. Thomas H. Kendall, for his assistance in the design of the experimental facility; and Mr. Harry D. Blessing for his skilled craftsmanship in fabricating the facility and test models. Appreciation is also expressed to Messrs. George C. Van Fossen, R. Joseph Shaw, Hudson L. Conley, and Robert C. Prior for their assistance in the acquisition and reduction of the experimental data.

The author gratefully acknowledges the United States Air Force Aero Propulsion Laboratory, Wright-Patterson Air Force Base, Ohio, which provided the financial support for this effort through Contract F33(615)-69-C-1004.

TABLE OF CONTENTS

TABLE OF CONTENTS - (Continued)

LIST OF FIGURES

LIST OF FIGURES - (Continued)

LIST OF FIGURES - (Continued)

LIST OF FIGURES - (Continued)

LIST OF FIGURES - (Continued)

LIST OF TABLES

LIST OF TABLES - (Continued)

LIST OF TABLES - (Continued)

NOMENCLATURE

Symbol	Description
a	speed of sound (Appendix A)
A	area (Appendix A)
A_H	cross sectional area of one hole = $\pi d^2/4$
b	equivalent slot height for one row of holes = A_H/z
B	blowing parameter = 10^3 Fb/$\frac{c}{2}$
c	nominal airfoil chord = 2 inches
c_p	specific heat of air at constant pressure
C_H	Stanton number = $\frac{\dot{q}}{\rho_e u_e c_p (T_{aw}-T_w)}$
d	diameter of blowing hole
F	mass flux ratio of coolant and inlet flows = $\frac{(\rho u)_c}{(\rho u)_1}$
h	heat transfer coefficient = $\frac{\dot{q}}{T_{aw}-T_w}$
K	a constant
$\dot{m}$	mass flow rate
M	mass flux ratio of coolant and boundary layer edge flows = $\frac{(\rho u)_c}{(\rho u)_e}$
M	Mach number (Appendix A)
n	number of upstream blowing rows
N	number of blowing holes per surface
P	pressure, also denotes pressure surface blowing
$\dot{q}$	surface heat transfer rate per unit area

NOMENCLATURE - (Continued)

Symbol	Description
R_e'	Reynolds number per foot
R_{e_x}	local Reynolds number (based on x) = $\frac{\rho_e u_e x}{\mu_e}$
s	equivalent slot height for n upstream hole rows = nb
S	denotes suction surface blowing
S + P	denotes blowing on both suction and pressure surfaces
T	temperature
t	time
u	velocity
x	surface distance from leading edge
$x_1, x_2, \cdots, x_n$	surface distance upstream to (1, 2,$\cdots$, nth) row of holes
y	coordinate normal to surface or flow direction
z	spanwise distance between centerlines of discrete holes
γ	ratio of specific heats
η	effectiveness ratio = $\frac{T_{w_o}-T_{\infty}}{T_{w_o}-T_c}$
θ	inclination of hole from spanwise surface tangent
μ	viscosity
ξ	coolant-to-inlet mass flow rate ratio = $\frac{\dot{m}_c}{\dot{m}_1}$
ρ	density
τ	minimum metal thickness between adjacent holes within one row

Symbol	Description
φ	inclination of hole from chordwise surface tangent
ω	integrated total pressure loss coefficient $= \int_{-0.3}^{+0.3} \frac{P_{t_1} - P_{t_2}}{P_{t_1} - P_2} \, d\left(\frac{y}{y_2}\right)$, $(y_2 = 1 \text{ inch})$

Subscripts

aw	adiabatic wall
c	coolant
e	edge of boundary layer
j	upstream of blowing (Appendix A)
k	downstream of blowing (Appendix A)
n	nth row of holes
t	total or stagnation
w	wall (surface of airfoil)
o	no blowing
1	inlet (upstream measuring station)
2	exit (downstream measuring station)

I. INTRODUCTION

The use of cooled turbine blades has made possible present-day turbojet engines with turbine inlet temperatures greater than 2000°F, and substantial further improvements in allowable maximum temperatures are foreseen through the use of advanced cooling schemes. The types of cooling either employed or being investigated include internal fuel flow, convection, impingement, transpiration, and film cooling. The latter four generally use compressor-bleed air and are most effectively used in combinations of several methods on the same airfoil. A typical blade might use a combination of convection, impingement, and film cooling. Several possible combinations are shown in Fig. 1 as examples of turbine airfoils cooled by the various methods which employ air as the coolant.

The selection of the method(s) to be used in cooling a turbine airfoil involves the consideration of a number of factors and depends on much more than merely the heat transfer distribution over the blade and the cooling effectiveness of the available methods. Certainly two of the primary considerations are the structural and aerodynamic complications resulting from the cooling. The structural problems are introduced by the necessary channels, passages, and orifices required by the cooling geometry. The structural limitations are especially severe for transpiration cooling schemes because of the strength limitations of porous materials. The aerodynamic limitations are primarily a problem for film and transpiration cooling, but exist also for convective and impingement schemes since even for these non-mass transfer cooling techniques the coolant air must be expelled from the blade, usually near either the trailing edge or the tip of the blade. In any case, whenever air is injected into the turbine flow, some alteration of the flow field from that existing for no injection must occur. The problem, simply stated, is to minimize the flow field alterations, since such alterations are, by their very nature, generally not desirable.

The aerodynamic effects of coolant expulsion from the turbine airfoil depend significantly on the method and amount of coolant injection into the mainstream. The mass transfer cooling techniques of film and transpiration cooling are the most harmful to the flow field since they must emit the coolant air from some portion of the airfoil "working" (lifting) surface. The effects of transpiration cooling on the airfoil flow field might be expected to be less severe than those of film cooling since considerably less coolant flow is required to cool the same surface by an equal amount.[1] In addition, film cooling must inject the coolant mass through discrete holes or slots, thus disturbing the flow and introducing almost instantaneous, abrupt increases in the thickness of the boundary layer. This increase is bound to cause a greater disturbance in both the viscous and inviscid flows than would normally be caused by transpiration cooling.

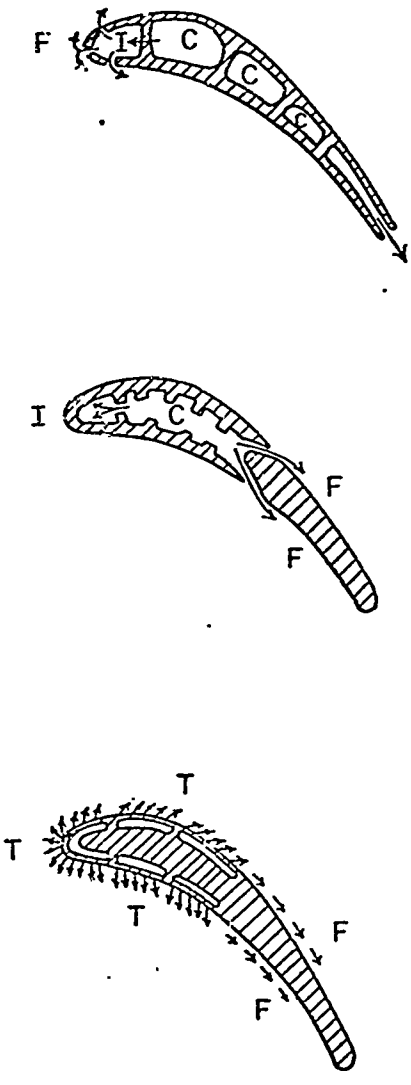

Fig. 1 - Three possible turbine airfoil cooling schemes employing combinations of Impingement (I), Transpiration (T), Convection (C), and Film (F) Cooling

It might be asked at this point if there are any reasons for even considering film cooling, since it appears to have the disadvantages of being both less effective as a cooling technique and more disruptive aerodynamically than the other mass transfer method; i.e., transpiration. There are clearly some advantages to film cooling. Structurally, it is much easier to design and fabricate a film-cooled blade. Even a transpiration-cooled blade, such as the one shown in Fig. 1, would probably rely on the residual film-cooling effect for the trailing-edge region, because of the obvious difficulty of constructing a porous emission surface and coolant feed ducting in the space available in the thin trailing-edge region of the blade. Also, the physical danger of local pore obstruction could result in a local catastrophic failure due to overheating if the residual cooling effect of adjacent porous regions were insufficient. Film cooling, on the other hand, is also effective over some region downstream of the mass addition location, and can thus cool remotely. Furthermore, the larger, discrete holes or slots used in film cooling make the blockage by a foreign object far less likely.

The effect of film cooling on the aerodynamic characteristics of a typical turbine blade should be somewhat dependent on the mass addition geometry and blowing rate. It is obvious that the boundary layer will be affected since much of the coolant will be entrained in this layer. The thickening of this viscous layer in an almost stepwise fashion should lead to an apparent "thickening" of the airfoil profile and thus alter the static pressure distribution and hence the airfoil lift. This effect may be quite negligible for small blowing rates, but as higher turbine inlet temperatures are required, the increased blowing rates may radically alter the static pressure distribution. It would seem logical that at a sufficiently high blowing rate the boundary layer could even be completely separated from the blade surface. Since an efficient turbine blade operates at a relatively high lift-to-drag ratio, it is quite probable that massive blowing on the suction (low pressure) surface could induce stall by boundary layer "blow-off." For this reason, film cooling mass addition on current turbine blades is primarily limited to a region relatively near the leading edge where the pressure gradient is favorable (negative). This limitation of film cooling to the leading edge region results in reduced cooling effectiveness in the mid-chord and aft regions of the blade, regions which are also difficult to cool by other means. Furthermore, in the aft region there is quite likely a turbulent boundary layer, thus complicating the heating problem. In short, film cooling appears to be a desirable method of cooling not only the leading edge, but also the aft region of a turbine airfoil, providing the aerodynamic effects do not seriously degrade the airfoil performance.

The basic film-cooling problem has been widely studied both analytically and experimentally by many workers in the field. The majority of the analytical studies have dealt with determination of the adiabatic wall temperature distribution over a flat plate downstream of the injection region.[1-4] The convenient model for injection geometry in any

theoretical study is the slot, which allows the problem to be treated two-dimensionally. The more general problem of discrete hole injection has not appeared amenable to theoretical solution to date.

Experimental studies of film cooling have included both slot and discrete hole geometries,[5-12] however, even here the primary emphasis has been on the two-dimensional slot. Again the majority of the studies has been concerned with the adiabatic wall temperature distribution downstream of the injection region on a flat plate with a turbulent boundary layer, although some studies, such as that by Haering,[10] have included the effects of pressure gradient and surface curvature. The importance of these experimental investigations lies in the fact that correlations of the primary similarity parameters giverning film-cooling effectiveness have been determined sufficiently well to allow for engineering calculations. Although the experimental studies have been primarily of flat plate flows, Haering,[10] as an example, has found that for tangential slot geometries in a transonic nozzle the effect of negative pressure gradient on the film cooling is not important (he also states that, based on his unpublished data obtained under separated flow conditions, a strong positive pressure gradient does show a severe adverse effect on film cooling). Such results thus suggest the use of available flat plate correlations to predict the adiabatic wall temperature over airfoil shapes such as turbine blades, providing the injection is from a tangential slot-like geometry and no severe positive pressure gradients are present.

The problem of predicting film-cooling effectiveness becomes much more difficult to attack when discrete holes are used to inject the coolant instead of a continuous slot. Experimental investigations such as that of Metzger and Fletcher[12] show that discrete hole geometries are considerably less effective than a continuous slot in cooling the region downstream of the injection, but interest in discrete hole film cooling remains high because of structural considerations. It has been shown that multiple slots can allow a considerable reduction in the coolant required to cool a surface by a specified amount,[13] and a similar effect, perhaps to a lesser degree, could be expected to hold for multiple rows of discrete holes. However, when multiple rows of discrete holes are considered, the problem becomes inordinately complex from an analytical viewpoint, and the experimental approach has here also been the most effective means for studying the problem.

When all of the aforementioned film-cooling studies are examined, it is surprising to note how little published work has been devoted to the effect of film cooling on the aerodynamics of a typical turbine airfoil; e.g., the pressure distribution and external flow over an airfoil-shaped body. This is in spite of the fact that a decrease of only a few percentage points in turbine efficiency due to the aerodynamic effects of cooling could more than negate the increase in thrust and decrease in specific fuel consumption obtained by the increased turbine inlet temperature allowed by cooling. Thus it appeared that an experimental investigation of multiple-row, discrete hole film cooling of a

turbine airfoil could make a significant contribution by revealing the aerodynamic effects of blowing on the lift and drag of a typical turbine airfoil. Such an experimental investigation could also provide some indication of the validity of the numerous single-slot, flat-plate film-cooling effectiveness correlations when applied to a curved surface which is cooled by multiple rows of holes. Although such correlations are probably adequate for engineering design purposes when applied to single-slot injection in the leading edge region of a turbine airfoil, their applicability to multiple-row hole geometries has not yet been verified.

It should be noted that although the aerodynamic effects of film cooling on turbine airfoils have not been examined in detail in the open literature, several recent papers have reported experimental data on the aerodynamic performance of transpiration-cooled blades. The survey of Barnes and Came[14] presents the results of several experimental cascade investigations which show that for small coolant-to-primary mass flow rate ratios ($\xi < 0.03$) the total pressure loss coefficient increases linearly with ξ. Furthermore, a recent study by Provenzale and Thirumalaisamy[15] of the aerodynamic performance of an annular cascade of transpiration-cooled stator blades shows that for coolant flows as high as 5.4% of the primary flow the static pressure distribution over the airfoils remains essentially unchanged. However, it is impossible to predict what effect an equivalent amount of film cooling would have on the static pressure distribution, particularly when the unique dependence of film cooling on the injection geometry is considered.

In order to parametrically investigate the problem of the aerodynamic effects of massive multiple-row discrete hole film cooling, the approach adopted for the present investigation has been to:

1. select a typical turbine airfoil shape and fix the desired number of rows of film cooling ports;

2. vary the injection hole geometry on a series of models, keeping the model profile and the location of the rows of holes identical for all models; and

3. conduct tests at several inlet temperature-to-coolant temperature ratios, measuring the blade temperature, the static pressure distributions, and the wake total pressure.

In considering the thermal and aerodynamic performance of a film cooled airfoil, there are a number of parameters which are of interest. These have been reasonably well identified by the various investigators in the once separate fields of mass transfer cooling and turbine development. The generally accepted measure of the actual film cooling performance is the effectiveness η, defined by

$$\eta = \frac{T_{w_o} - T_w}{T_{w_o} - T_c} \quad . \tag{1}$$

The independent correlating parameters for η are numerous, but available evidence for slot injection geometries indicates that those of primary importance are the mass flux ratio M, the slot height to the surface distance downstream of injection x, and the Stanton number for no blowing C_{H_o}.[16] The above parameters have been used successfully to correlate most of the single-slot data obtained to date, and it is reasonable to expect that they will also play a major role in correlating multiple-row, discrete hole data, although a change of form or the inclusion of additional parameters may indeed be necessary.

The parameter generally used in turbine airfoil studies to account for losses due to mass transfer cooling and viscous effects is the total pressure loss coefficient. This parameter may be written in its simplest form as

$$\omega \propto \frac{P_{t_1} - P_{t_2}}{P_{t_1} - P_2} \quad , \tag{2}$$

where conditions 1 and 2 are upstream and downstream of the airfoil, respectively. Measurement of this quantity may be carried out along the coordinate normal to the downstream flow by the use of a traversing probe and the resultant curve integrated to give a more accurate accounting of the loss in total flow momentum due to both the airfoil profile and the coolant injection.

A third major airfoil characteristic which is indicative of turbine blade performance is the static pressure distribution. Relatively easy to measure for a stationary airfoil, this profile gives a direct indication of the lifting efficiency of the blade.

With the above-noted measurements, these three characteristics of a film-cooled airfoil--the cooling effectiveness η, the wake total pressure loss coefficient ω, and the static pressure distribution--can be evaluated and a meaningful comparison of the thermal and aerodynamic efficiencies of widely differing injection geometries can be carried out. For the present study it was decided to employ five rows of coolant holes on each surface of the film-cooling models, an arrangement which might be typical of advanced cooling schemes which in the future would employ massive film cooling ($\xi > 5\%$). Separate models were used to measure the heat transfer rate in the absence of film cooling to obtain the no-blowing Stanton number, C_{H_o}. This latter measurement was felt to be a desirable part of the experimental program, not only because C_{H_o} is used in correlating film cooling data, but also to provide definite information concerning the state of the boundary layer over the airfoil.

The basic experiment as thus far described appears ideally suited for a cascade study. However, limitations imposed by the available facilities suggested an alternate approach, that of a single blade tested in a contoured channel in which the walls were both movable and perforated in order to adjust the surface pressure distribution, and contained film coolant ports to simulate blowing from adjacent blades. This approach was used to obtain the present experimental results. The emphasis in this study is placed on the aerodynamic effects, particularly for massive blowing rates. Although data obtained in such a facility cannot be expected to predict the performance of any particular turbine stage, the fundamental effects of massive blowing on the losses associated with the airfoil flow field were readily observable. The goal of this study, then, is to improve the basic understanding of the problem in such a manner that future film-cooled turbine blade design might begin with a reasonable prediction of the maximum tolerable blowing rate and the most effective injection geometry to accomplish the necessary cooling.

II. EXPERIMENTAL APPARATUS

A. THE HIGH-TEMPERATURE TURBINE AIRFOIL TEST FACILITY

The High-Temperature Turbine Airfoil Test (HTTAT) Facility used in this investigation was designed and built at The Ohio State University Aeronautical and Astronautical Research Laboratory (OSUAARL) expressly for the purpose of this investigation. The facility provided continuous inlet flow about a single two-dimensional turbine blade of two-inch span. The blade was positioned in the middle of a two-dimensional (constant width) channel which was contoured to simulate the presence of adjacent blades in a cascade or an actual turbine stage. The choice of the single-blade channel, as opposed to the cascade testing method, was dictated by the limited air and power available.

A typical two-inch chord turbine airfoil was selected for the program, thus requiring a flow width of at least two inches if an aspect ratio of 1 was to be obtained. Located at OSUAARL is a 600 kW, 2500°F maximum temperature resistance heater, normally used to supply a continuous flow of heated air for a 12-inch hypersonic wind tunnel. Since this energy source of known characteristics was readily available, the approach taken was to design the test facility to mate with this heater.

A stagnation pressure of 3 atmospheres was used for all design calculations since this pressure would allow direct venting of the facility to the atmosphere through a choked exit, eliminating the need for a diffuser or vacuum pump system. In addition, a reasonably high pressure level was desired in order to maintain the Reynolds numbers necessary to simulate actual turbine conditions. Thus, to achieve the maximum operating temperature an inlet area of less than 3.5 in.^{2} was all that was possible without pushing the heater to its maximum power of 600 kW, and the design of the HTTAT test cabin was based on the following conditions:

inlet area = 3.3 in.^{2}
maximum inlet stagnation temperature = 2500°F
inlet stagnation pressure = 3 atmospheres
nominal inlet Mach number = 0.35
blade chord = 2 inches
blade span = 2 inches

A transition section was added to the exit of the existing heater to adjust the flow from the circular cross section of the double-pass heater to the rectangular cross section of the test cabin. Three screens were incorporated into the transition section to achieve uniform flow properties and allow higher operating pressures in the heater. Several more screens were located in the heater proper, so that a total pressure drop of more than 60% was achieved from heater core to test cabin inlet.

Once the inlet area and channel width were selected, the next step in the facility design was the contouring of the test section channel. A diagram of the final contour is shown in Fig. 2, where the adjacent blades in a typical cascade have been superimposed on the diagram. The test section wall contour was based on the blade mean camber line and a total flow deflection of 76.2°. The nominal blade angle of attack was 54.5° and the stagger angle of the simulated cascade was 16.7°.

In order to facilitate operation in the transonic flow regime and to adjust the flow to the 76.2° turning angle, porous, movable walls were incorporated in the aft portion of the test cabin. This allowed adjustment of the flow direction and permitted fine adjustment of the static pressure distribution over the airfoil. The porous walls, more commonly found in transonic wind tunnels, minimize the effect of the walls and allow the downstream flow to more closely simulate that of the flow leaving a cascade. In addition, plenum chambers bounding the porous walls were joined by an external tube, allowing equalization of their pressures and providing a nearly constant pressure boundary for the wake of the blade.

The test cabin itself was composed of four major components: concave and convex contoured walls, and two flat side walls. All four major pieces were fabricated from stainless steel with wall thicknesses of one inch or more. Figure 3 shows the four major pieces of the cabin with a turbine blade in position and one wall removed for viewing. The two sidewalls contained circular mountings for 2.5-inch diameter quartz windows, centered on the blade to allow the capability for Schlieren photography of the flow field at low stagnation temperatures. At elevated temperatures the quartz windows were replaced by metal inserts with slots, contoured to the blade profile, through which the ends of the airfoil extended to receive coolant air and instrumentation.

The walls of the test cabin contained four rows of film coolant ports identical to those on one of the blades tested and located at approximately the same position in which they would be found if adjacent blades were present.

A stationary total pressure probe and a static pressure tap were located at the test cabin inlet to monitor the inlet flow conditions. Movable total pressure survey probes were located downstream of the airfoil, as shown in Fig. 4. Numerous static pressure taps throughout the test cabin assisted in determining flow conditions and facility characteristics.

The flow exited the test section through a constant-area channel six inches in length followed by a rectangular converging nozzle, dumping the flow into a six-inch diameter diffuser duct which was vented directly to the atmosphere. The total pressure was maintained sufficiently high to ensure choked flow at the nozzle exit, so mass flow control and inlet Mach number could be varied by both adjustment of the

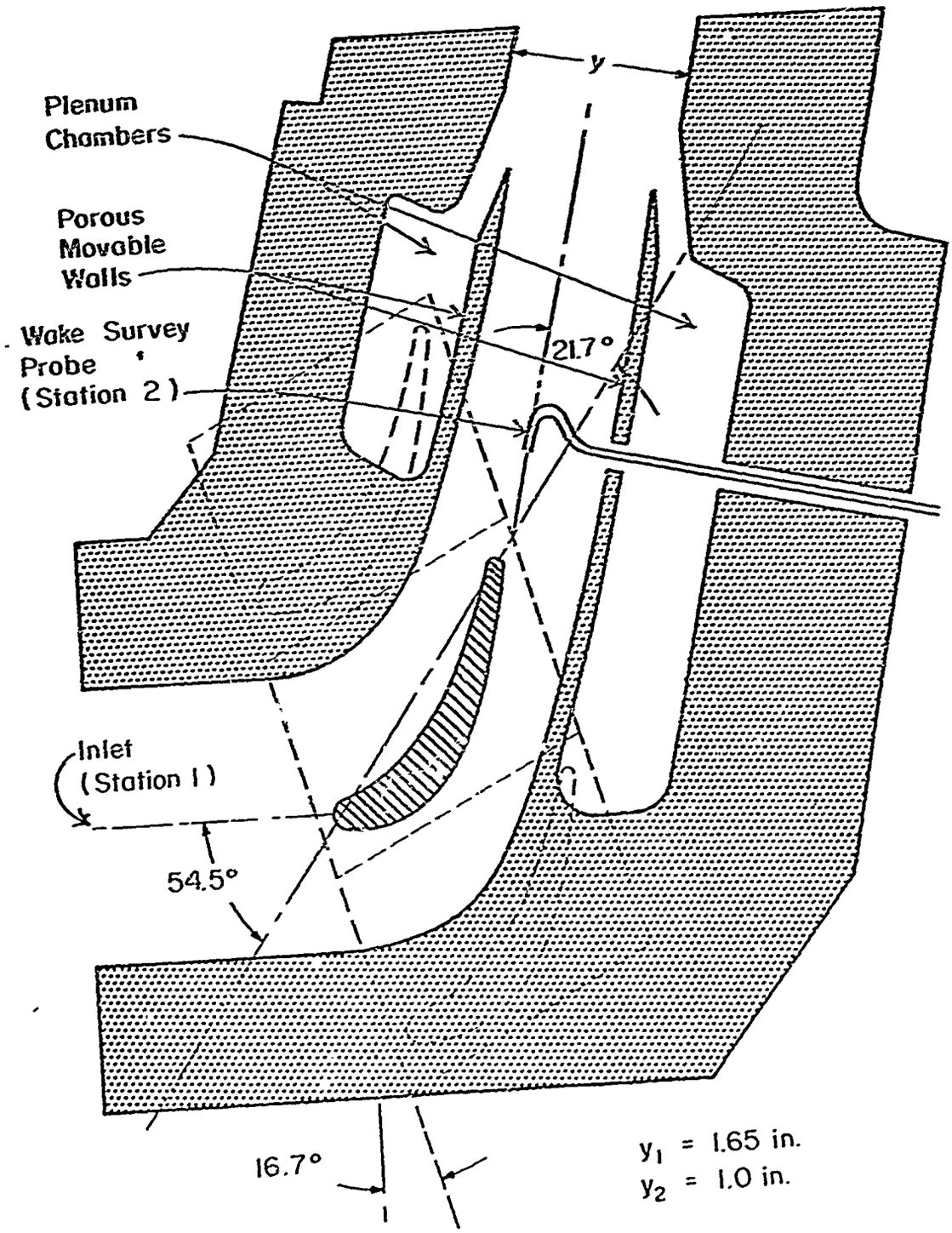

Fig. 2 - Profile of test cabin and related cascade

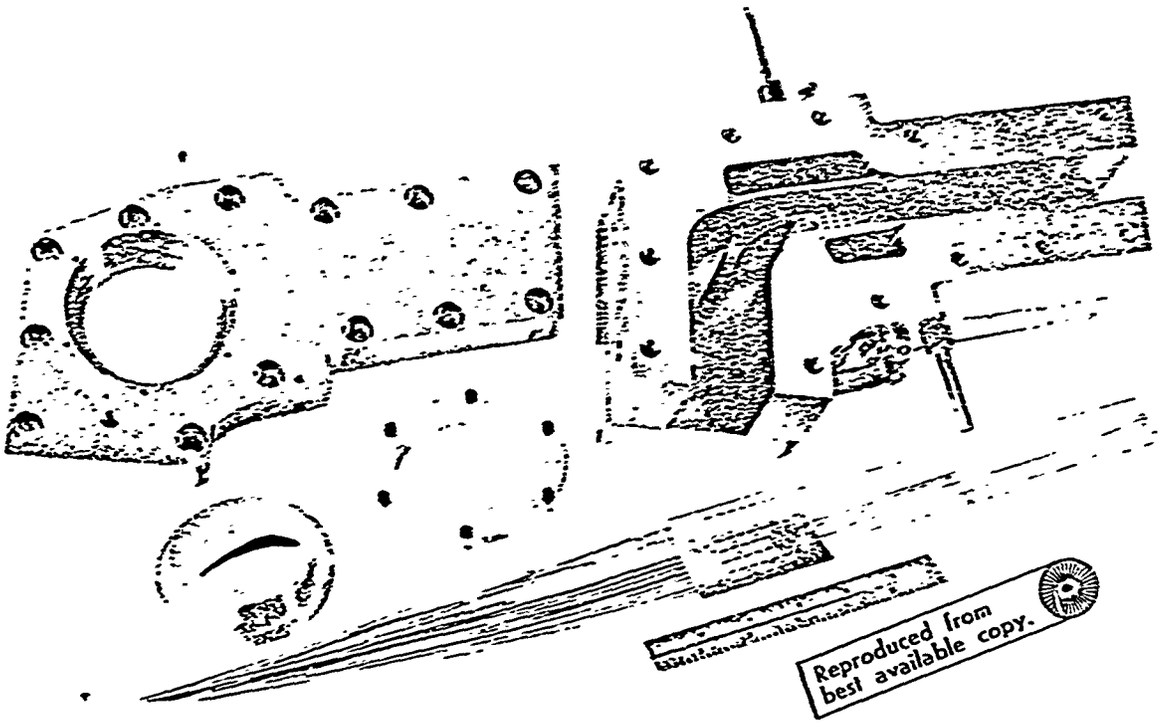

Fig. 3 - Pre-assembly view of HITAT facility test cabin showing mounted and unmounted film-cooling models, sidewall mounting plate, and 6-inch scale in foreground

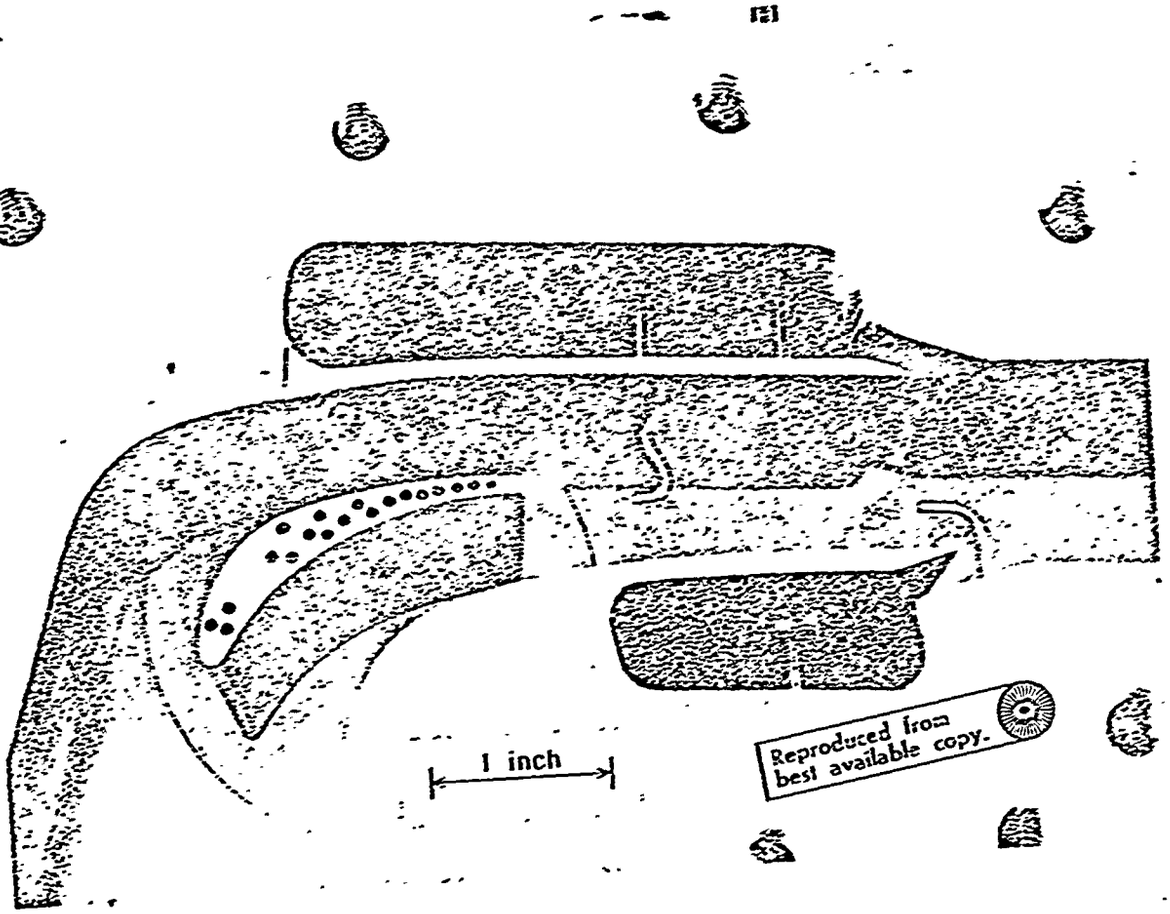

Fig. 4 - Closeup view of turbine airfoil mounted in contoured test cabin channel showing pressure survey probes, movable porous walls, and plenum chambers

total pressure and variation of the choked exit area. Two different converging nozzles, with choke areas of 1.54 and 1.70 in.^{2}, were used to obtain either subsonic or transonic flow over the suction surface of the airfoil. These conditions corresponded to blade pressure ratios (inlet total-to-downstream static pressure ratios) of $P_{t_1}/P_2 = 1.5$ and 1.7, respectively.

A view of the complete HYMAF Facility is shown in Fig. 5.

B. DESIGN AND FABRICATION OF MODELS

The basic turbine airfoil selected for testing was a typical two-inch blade, shown with its coordinates in Table I. This blade was an attractive choice since static pressure distribution data obtained in cascade testing using this profile had been previously published.[17]

Four different types of data were required for this study. These include measurements of the static pressure distribution, wake total pressure profile, and temperatures at selected points on the blade, all in the presence of film cooling, and heat transfer measurements for the no-blowing case where only transient temperatures need be measured. Two sets of models, one for the film cooling study and another set for the no-blowing heat transfer measurements, have thus been used.

1. Film-Cooling Models

Measuring pressure and temperature simultaneously on the film-cooled models required spanwise channels for supplying coolant air to the film-cooling ports, plus separate spanwise channels for the pressure ports and thermocouples. The latter two measurements should be made near the centerplane of the blade to eliminate sidewall effects, thus model design and fabrication become more difficult because of space limitations. The testing approach desired was to accomplish static pressure, temperature, and wake survey measurements simultaneously with blowing from all five rows of holes on both surfaces. This approach reduced the number of pressure ports and thermocouples that could be located in the blade centerplane region, but still allowed a minimum of ten pressure ports and seven thermocouples per blade, along with the simultaneous mass addition from both surfaces.

The four film-cooling models were contoured from stainless steel bar stock by conventional machining methods. Spanwise channels for coolant air were drilled completely through the blade to allow coolant air supply from both ends of the blade, and blind channels for access to pressure ports and thermocouples were drilled coaxially from opposing sides to within 1/8 inch of the blade centerplane. Thermocouples and pressure ports were then located no further than 1/4 inch from the centerplane. Rows of film-cooling ports at the desired spacing and angular orientation to the surface and flow direction were then

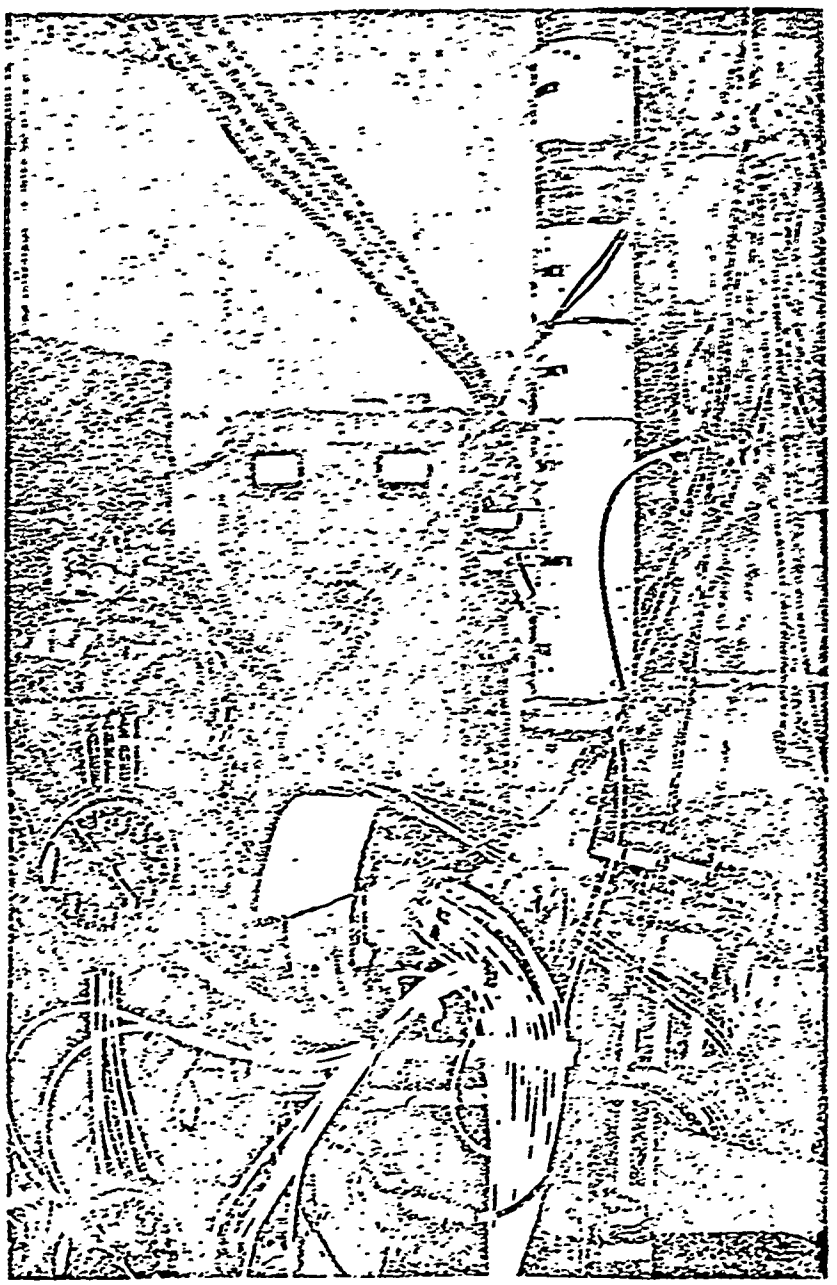

Fig. 5 - View of HITAT facility showing, left to right: stagnation heater, test cabin with mass addition and pressure measurement lines, and water-cooled vertical diffuser duct

Table I - Coordinates of the Turbine Airfoil

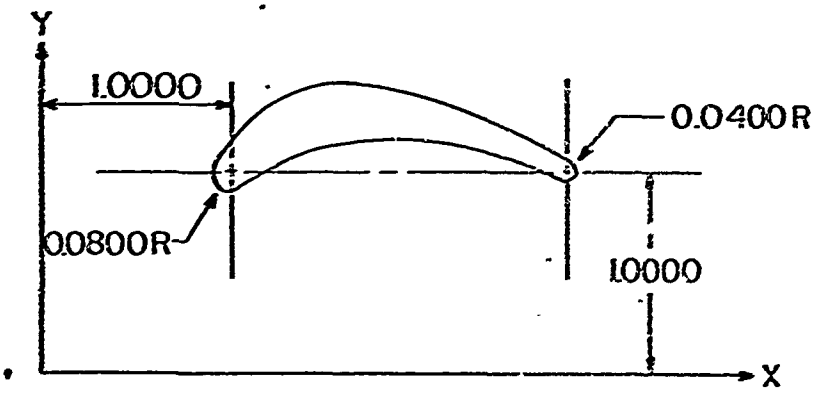

Station	X	Y	Station	X	Y
1	0.9200	1.0000	26	2.8334	1.0900
2	1.0440	0.9335	27	2.8093	1.0370
3	1.0917	0.9605	28	2.7006	1.0380
4	1.1403	0.9864	29	2.5966	1.1360
5	1.1867	1.0100	30	2.5050	1.1755
6	1.2342	1.0325	31	2.4126	1.2135
7	1.2807	1.0528	32	2.3182	1.2492
8	1.3275	1.0715	33	2.2226	1.2824
9	1.3748	1.0885	34	2.1260	1.3120
10	1.4220	1.1037	35	2.0282	1.3390
11	1.4700	1.1170	36	1.9275	1.3640
12	1.5432	1.1337	37	1.8270	1.3872
13	1.6173	1.1460	38	1.7290	1.4065
14	1.7140	1.1560	39	1.6102	1.4210
15	1.8057	1.1606	40	1.5050	1.4202
16	1.9010	1.1614	41	1.4005	1.4042
17	1.9980	1.1575	42	1.3325	1.3850
18	2.0928	1.1485	43	1.2663	1.3595
19	2.1877	1.1362	44	1.2040	1.3280
20	2.2825	1.1202	45	1.1445	1.2915
21	2.3767	1.1000	46	1.0850	1.2487
22	2.4697	1.0755	47	1.0335	1.2006
23	2.5616	1.0467	48	0.9945	1.1482
24	2.6654	1.0084	49	0.9568	1.0910
25	2.7774	0.9625	50	0.9288	1.0372

drilled down through the blade surface by electrical discharge machining (EDM), a process whereby the metal is literally burned away by large electrical current flow.

Figure 6 shows qualitatively the basic features of a film-cooling model. Thermocouples were located either on the blade camber line or within 0.010 to 0.025 inch of the surface. To locate some of the thermocouples near the surface, access holes were drilled from the opposite surface to within the desired surface clearance, the thermocouples were installed, and the access holes were then filled with a temperature-resistant insulating cement and smoothed flush with the surface contour.

The detailed dimensions of the blowing geometries for the film cooling models are presented in Fig. 7 and Table II. These geometries were chosen to present contrasts in the angular orientation of the injectant fluid to both the blade surface and the flow direction. Certainly the case of blowing normal to the surface should be included since this is the limiting case for injections having inclinations in either the streamwise or spanwise directions. Although the choice of the discrete hole injection angles is purely arbitrary, it is still necessary to prescribe or adopt a basic rule for specifying the size and number of holes for each angular orientation. This necessity results primarily from the physical limitation that some minimum metal thickness must be maintained between adjacent holes in a row for the case of spanwise blowing. When holes are drilled at some angle θ from the local surface, inclined in the spanwise direction, the number of holes per unit of surface span must decrease by cos θ if the same hole-to-hole metal thickness is to be maintained.

The method adopted for the present study was to specify the hole size and spacing in such a manner that for a given coolant mass flow rate all geometries will possess approximately the same coolant mass flux normal to the blade surface, where the normal component of coolant mass flux $(\rho u)_{cy}$ is proportional to the total coolant mass flow rate $\dot{m}_c$ as

$$\dot{m}_c = K(\rho u)_{cy} \tag{3}$$

Some justification for this criterion can be seen in the fact that transpiration cooling effectiveness for a flat plate is correlated remarkably well by the vertical coolant mass flux in the form[18]

$$\eta \propto \frac{(\rho u)_{cy}}{(\rho u)_e} \frac{1}{C_{H_o}} ,$$

where, for transpiration cooling, $(\rho u)_c = (\rho u)_{cy}$. Since $(\rho u)_e$ is

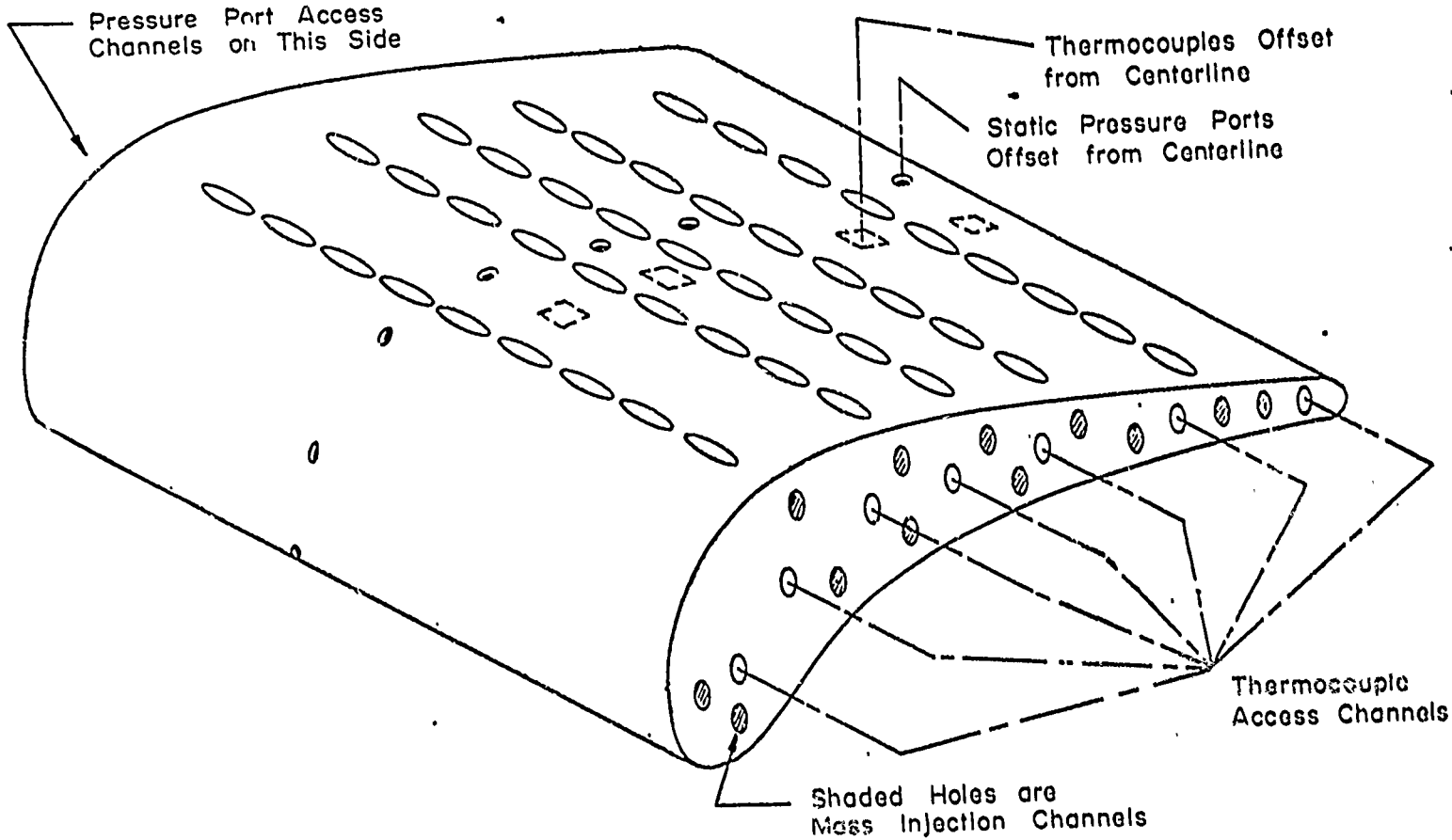

Fig. 6 - Basic features of the film-cooling models

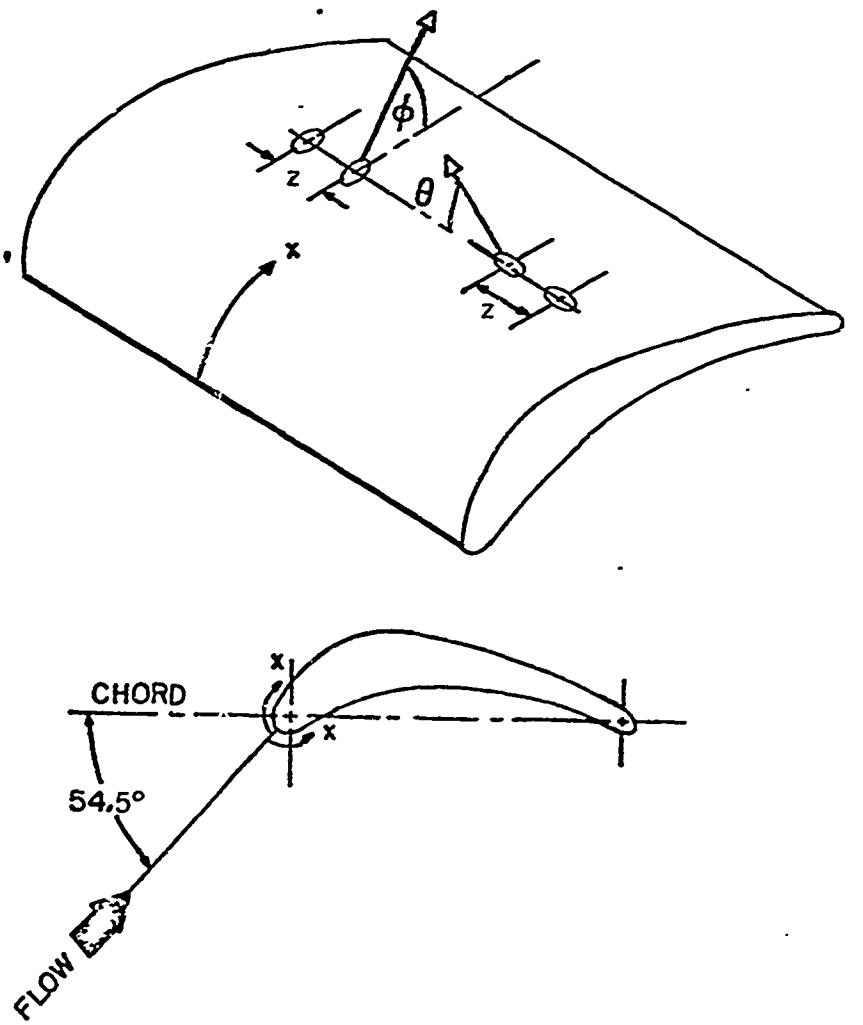

Fig. 7 - Coordinate system for blowing orifices and instrumentation on film-cooling models

Table II - Blowing Geometries of the Film-Cooling Models

Model	Surface	Holes Per Row	θ,°	φ,°	z, in.
I	Suction	7	12	90	.222
	Pressure	7	12	90	.222
II	Suction	34	90	90	.055
	Pressure	34	90	90	.055
III	Suction	17	30	90	.105
	Pressure	17	30	90	.105
IV	Suction	17	90	30	.105
	Pressure	11	20	90	.154

	Surface	Row 1	Row 2	Row 3	Row 4	Row 5
x for blowing rows, in. (all models)	Suction	.93	1.14	1.35	1.62	1.91
	Pressure	.69	.90	1.16	1.44	1.72

controlled by the free-stream conditions and since the no-blowing Stanton number is only weakly dependent on free stream conditions ($R_e^{-0.2}$ for turbulent flow), $(\rho u)_{c_y}$ is the primary independent variable for transpiration cooling effectiveness.

Applying Eq. (3) to the present film-cooling case, we obtain, from simple summation over all holes,

$$\dot{m}_c = N\dot{m}_H = N(\rho u)_c A_H \quad , \tag{4}$$

and from Fig. 8 we see that

$$(\rho u)_{cy} = (\rho u)_c \sin\theta \quad . \tag{5}$$

Using Eqs. (3), (4), and (5), the constant K is found to be

$$K = \frac{N A_H}{\sin\theta}$$

which is more conveniently written

$$K \propto \frac{Nd^2}{\sin\theta} \quad . \tag{6}$$

From Fig. 9

$$N = \frac{W}{z} = \frac{W \cos\left(\frac{\pi}{2} - \theta\right)}{(d+\tau)} \quad , \tag{7}$$

where W is the width of the blade wetted by the coolant. For $0 < \theta \leq \frac{\pi}{2}$, as is the case here, $\cos(\pi/2-\theta) = \sin\theta$. Thus Eq. (6) becomes

$$K \propto \frac{Wd^2}{(d+\tau)} \quad . \tag{8}$$

τ obviously should be as small as possible to maximize the number of holes per row in order to gain the best possible coolant distribution. Furthermore, for a given τ, the matching constant K, as given by Eq. (8), is primarily dependent on the hole diameter d. Thus all blades tested have been designed with the same orifice diameter, d = 0.028 inch. Referring back to Eq. (6), the choice of a constant diameter reduces the matching constant to

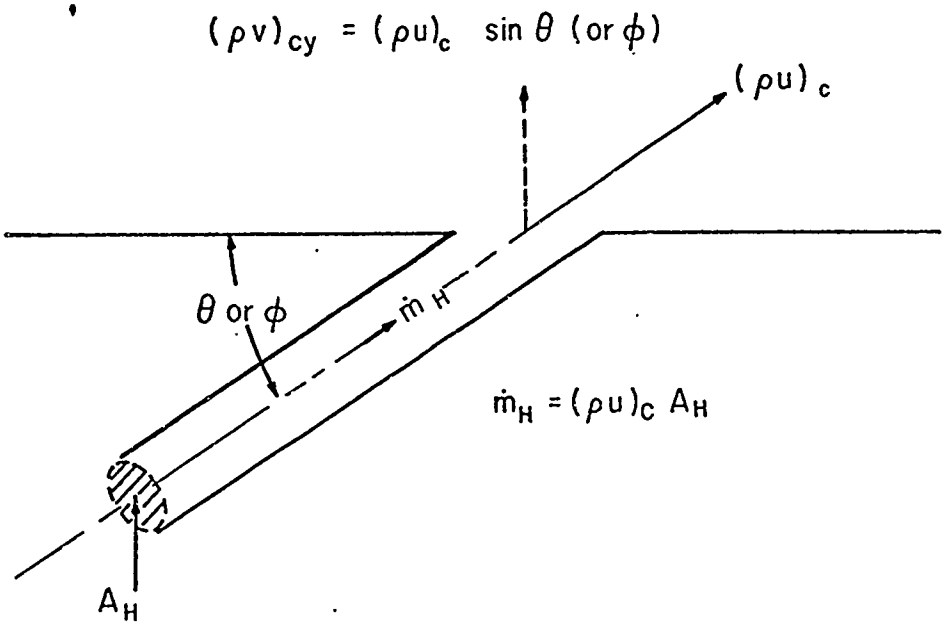

Fig. 8 - Definition of the normal component of coolant mass flux

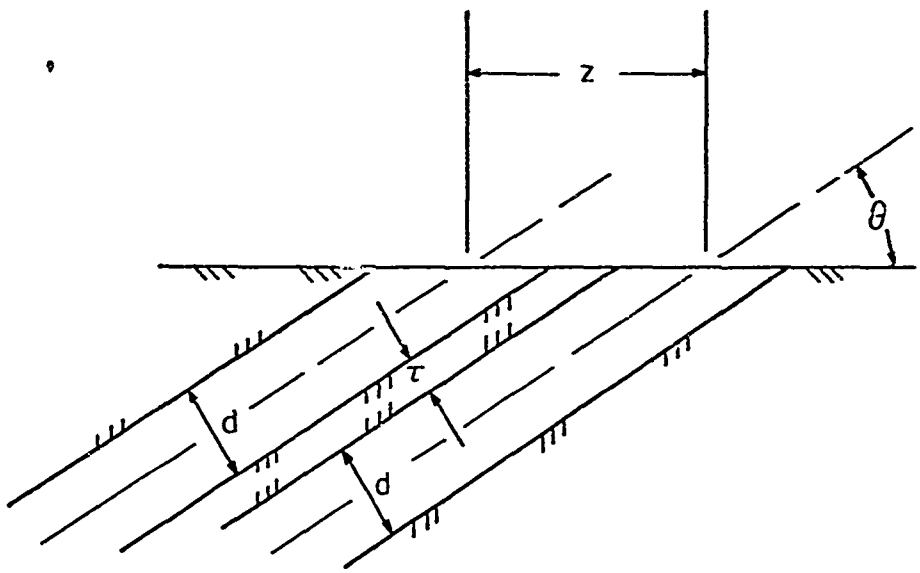

Fig. 9 - Discrete hole geometry within a single row of spanwise-angled blowing holes

$$K \propto \frac{\Pi}{\sin \theta}$$

for all blades in order to keep the same normal component of the coolant mass flux, $(\rho u)_{c_y}$, for a given coolant flow rate for all blades. Because of the use of one extremely shallow-angle geometry (12° from the spanwise surface tangent) and fabrication complexities, this rule could not be applied exactly, but all models tested were designed and built in such a manner that equal coolant flow rates gave nearly equal vertical components of the coolant mass flux.

2. Heat Transfer Models

The basic technique of measurement chosen for the determination of no-blowing heat transfer rates over the turbine airfoil employed the transient thin-skin thermometry method. This method of measurement placed two primary design requirements on the heat transfer models; namely, that a model had to be impulsively immersed in the pre-existing steady state flow field and that a large portion of the model surface had to be composed of a thin metallic skin.

The first requirement, that of impulsive insertion into the pre-existing flow field, was accomplished by the use of a slave blade having the same profile as the heat transfer model. A two-dimensional flow, such as that over the single turbine airfoil in a contoured channel, is ideally suited for this technique since, by use of a spanwise elongated model, the test cabin blockage can be kept constant during insertion. The technique adopted was to link the slave blade to the heat transfer model and allow the insertion of the heat transfer model to simultaneously expel the slave blade. Two heat transfer blades were used in this study, one for measurements on each of the pressure and suction surfaces. Figure 10 shows a heat transfer model and slave blade combination.

Each of the two heat transfer models was fabricated from solid stainless steel stock. Two techniques of obtaining a thin skin surface were used. For the pressure surface model, a rectangular region 1/2 x 1-5/32 inches was machined out of the suction surface, leaving a 0.010-inch thickness of base metal on the pressure surface. For the suction surface measuring model, a similar rectangular cutout was machined completely through the blade and a 0.010-inch-thick sheet of stainless steel was welded flush to the surface. After thermocouple installation on the underside of each thin-skin surface on both models, the cutout portion was refilled with high temperature-resistant insulating cement and smoothed flush with the surface. Figure 11 shows the dimensions of each heat transfer model and the location of the thermocouples.

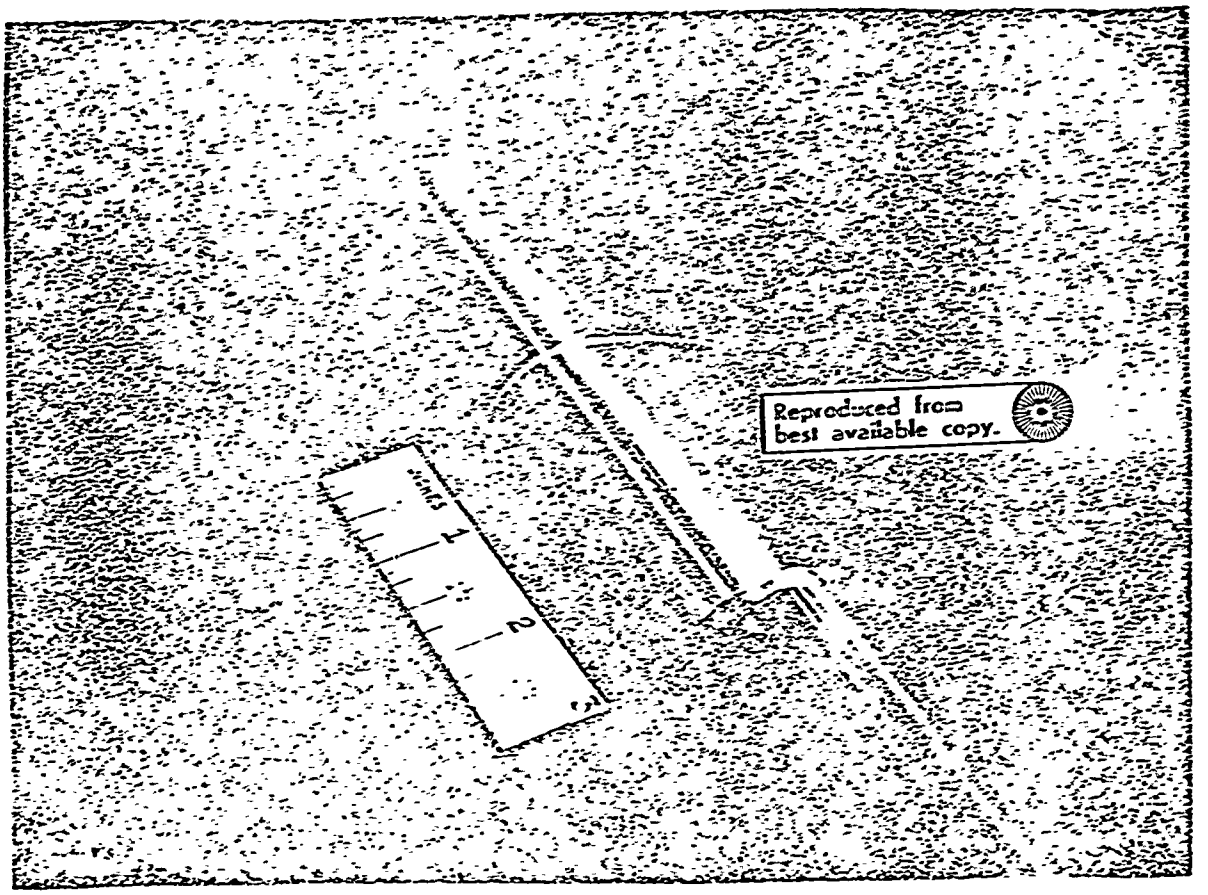

Fig. 10 - Suction surface no-blowing heat transfer model (foreground) joined with slave blade

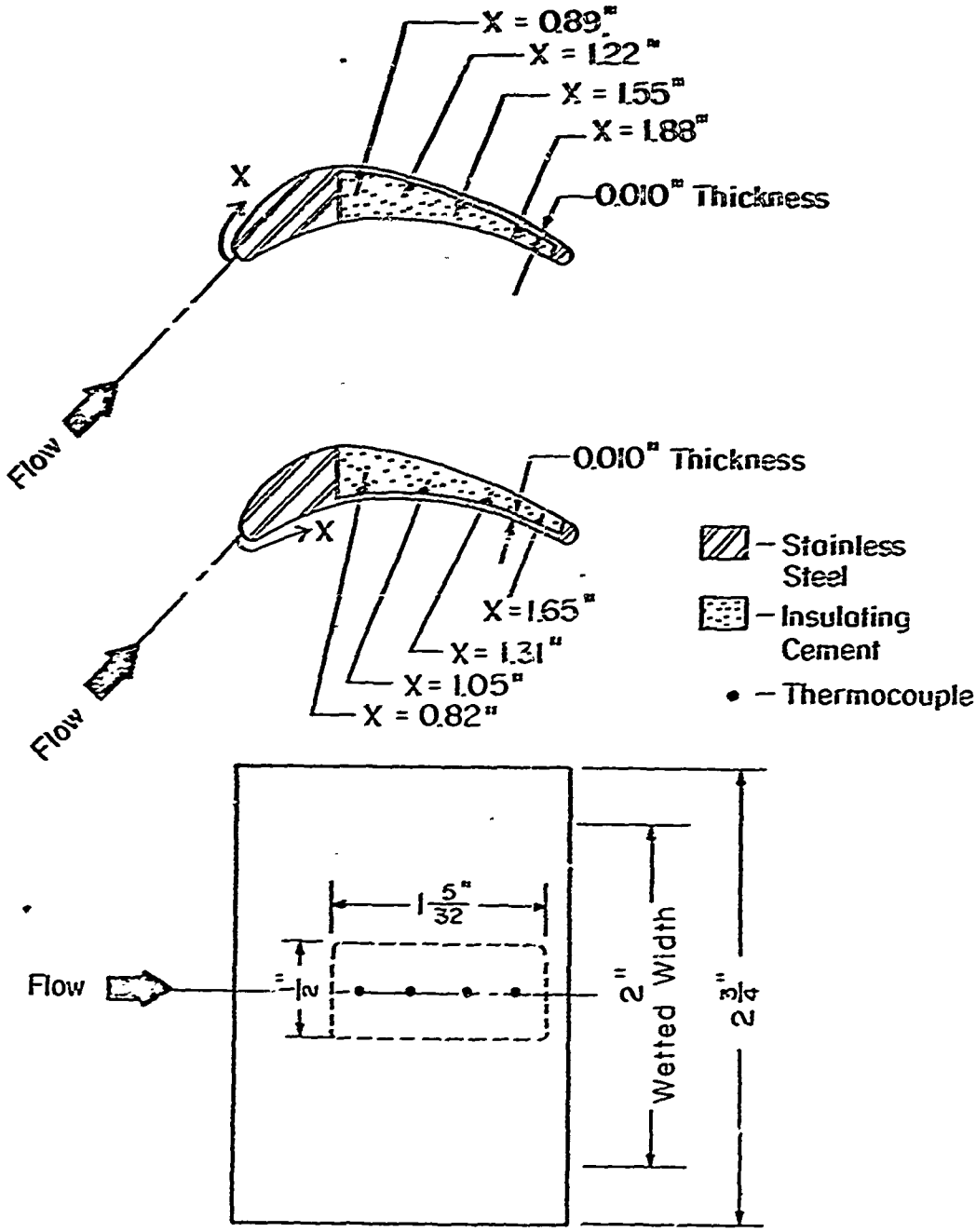

Fig. 11 - Pressure and suction surface heat transfer models

The two methods of obtaining the 0.010-inch-thick metal skin were tried in an effort to reduce the measurement error resulting from variations in skin thickness. Since the transient measuring technique yields heat transfer values only through accurate knowledge of the skin properties (including thickness), unknown variations in skin thickness will introduce error. The skin must also be sufficiently thin to minimize lateral conduction, particularly from the main body of the model. Thermocouples in these models were located a minimum of 30 skin thicknesses from the main model body, reducing any lateral conduction. Skin thicknesses were checked and found to vary by no more than ±0.0005 inch from the nominal 0.010 inch thickness.

C. INSTRUMENTATION

The instrumentation used for control of the HYFAT facility was essentially the same as that used on the OSUAARL 12-inch hypersonic wind tunnel and as such it has been well proven over several years of use. The stagnation pressure was monitored by a Helicoid laboratory gauge having an accuracy of ±0.1 psig. Stagnation temperature was measured just upstream of the facility by a platinum-platinum rhodium thermocouple with a maximum error of ±10°F. This temperature was displayed continuously on a Brown strip recorder and, along with the stagnation pressure, was used to maintain constant flow conditions through the use of an automatic control system.

Pressure measurements for the film-cooling model tests were made by both transducers and mercury manometer tubes. Static pressures on the model surface and test cabin walls were measured using a 25-tube mercury manometer bank. Total pressures at both the inlet and in the wake survey location 0.63 inch downstream of the blade were recorded continuously using strain gauge and variable reluctance transducers. Their output was fed to an analog computer for printout and visual display on "x-y" plotters. The computer was used to non-dimensionalize the decrease in wake total pressure ($P_{t_1} - P_{t_2}$) by continuously dividing the measured decrease by the inlet total pressure, P_{t_1}. This technique was employed to minimize the effect of any variation of the inlet total pressure during a wake survey. The wake total pressure survey probe was mechanically linked to the core of a cylindrical linear differential transformer (LTD). The LTD, using a power supply, provided the analog computer with a linear voltage output which was porportional to the position coordinate y of the wake survey probe. Micrometer calibration of the system showed a maximum deviation from complete linearity of only ±1% over the 1-inch total travel of the proble. To achieve a steady and smooth rate of probe travel, a fine threaded, manually operated screw advance was installed on the survey probe. Figure 12 shows this total pressure measurement system schematically.

Coolant air was supplied independently to each surface of the film-cooling blades and test cabin walls. Each film-cooling surface received

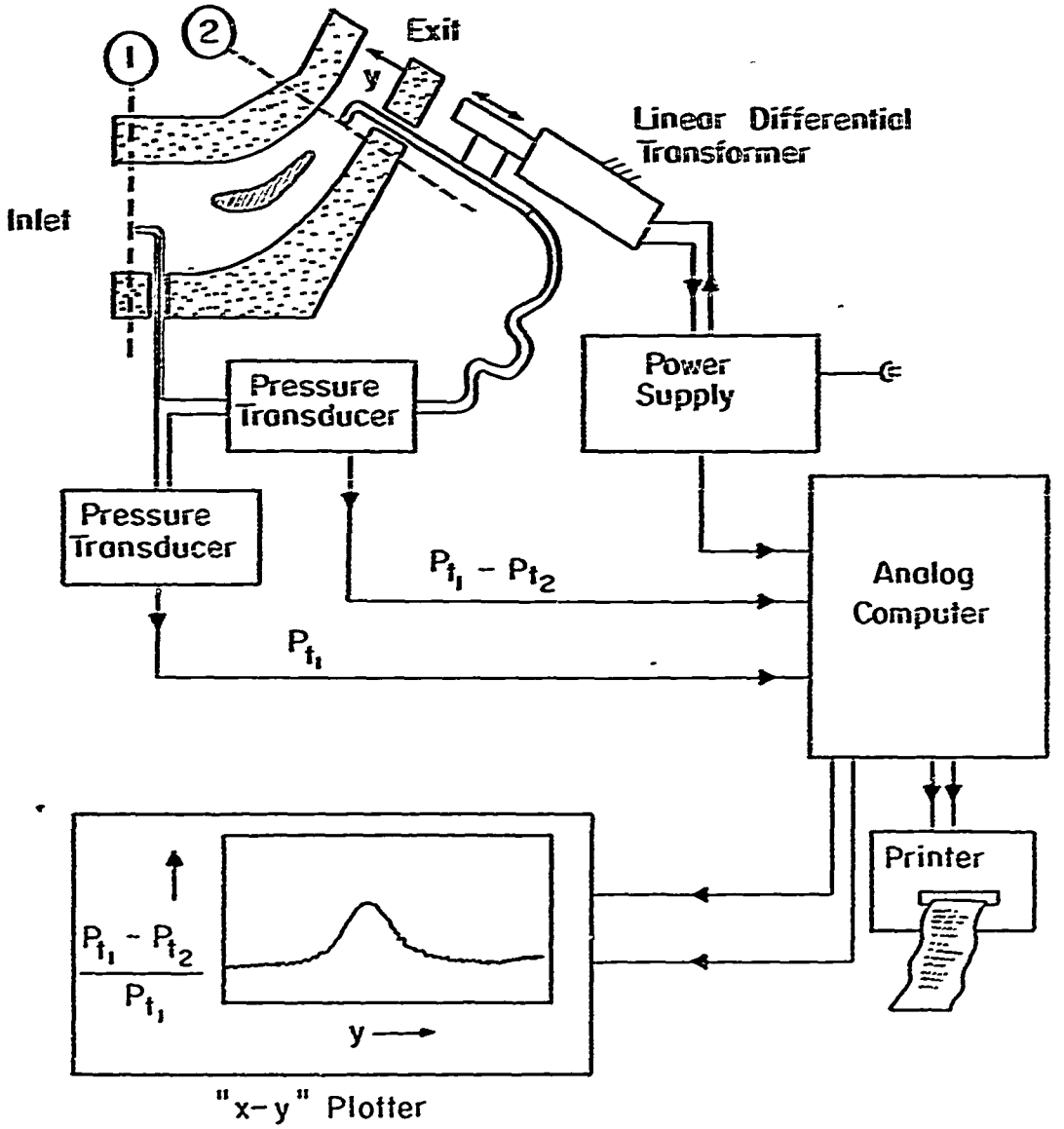

Fig. 12 - Schematic of the wake total pressure sensing system

coolant from both ends of the blade and all air lines feeding a given surface were fed from a common manifold. The coolant air flow into each manifold was independently controlled by a valve and metered by use of a a conical De Laval nozzle with Bourdon pressure gages upstream and downstream of the constriction.

Steady-state temperatures in the film-cooling airfoils were sensed by chromel-alumel thermocouples ceramically insulated in a stainless steel sheath of 0.040 inch diameter. The thermocouples were found to be accurate to ±5°F.

A somewhat different instrumentation problem was posed by the temperature measurement requirements of the heat transfer models. The measurement of heat transfer rates over a body surface has been performed previously at OSUAARL in wind tunnels, using thin-skin thermometry and rapid model insertion into the flow.[19] This technique determines the aerodynamic heating of the skin by measuring the transient temperature rise of the skin and relating this to the heat absorbed through a heat balance equation. The requirement that the insertion time of the model be extremely short has, for wind tunnel testing, been satisfied by using a pneumatic ram piston to rapidly move the model away from the test cabin wall region and insert it into the flow core. For the present case, where the flow area blockage by the airfoil is large, a slave blade was positioned in the flow to establish the proper flow field. The slave blade and model were joined physically by an insulator which was contoured to the airfoil profile. Openings in the test cabin sidewall, which were also contoured to the blade profile, allowed the simultaneous insertion of the model and withdrawal of the slave blade. Pressurized canisters on each side of the test cabin minimized leakage through the clearance between the blades and the contoured cutout. A pneumatic piston provided the ram force to insert the models with an insertion time of approximately 0.1 second. Figure 13 shows the heat transfer measurement apparatus installed on the HTTAT facility.

The heat transfer models employed copper-constantan thermocouples attached to the underside of the thin-skin portion of the model. The thermocouple junctions were first made and then attached to the metallic skin using epoxy resin cement. All junctions survived a minimum of 30 impulsive insertions and 5 of these survived over 50 runs. Thermocouple leads were carried outside the cabin through the hollow shaft used to drive the model into the flow. Figure 14 shows schematically the method used to obtain temperature vs. time plots each time a model was inserted into the flow. The millivolt-strength signal from a thermocouple was amplified by a Doelcam preamplifier and then fed to the analog computer. Here the signal was further amplified and the output was displayed on an "x-y" plotter. Although four separate thermocouples were handled simultaneously, each thermocouple circuit was separately calibrated. Plotted voltage output was easily converted to temperature using standard tables. The rate of plotter pen travel, equally important as thermocouple output to the accuracy of the final result, was controlled by a time integration circuit in the analog computer.

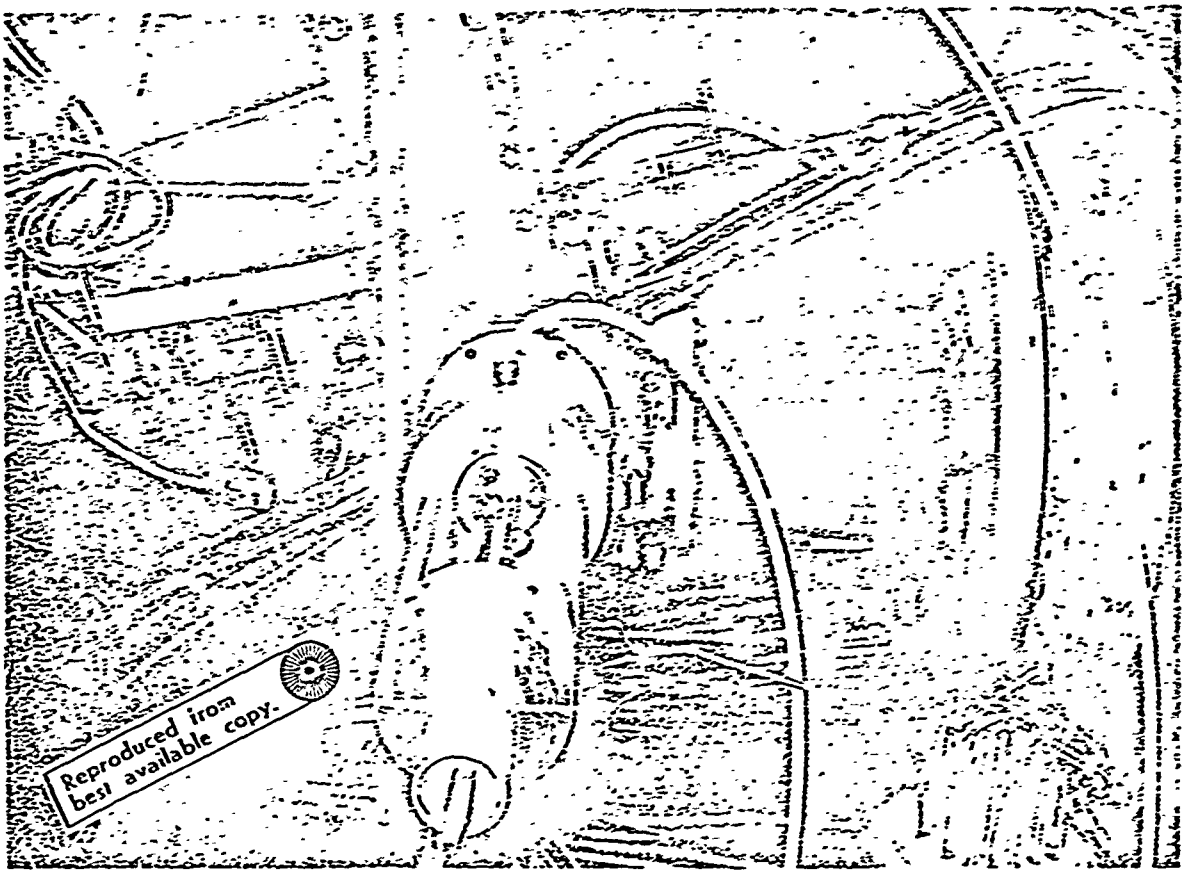

Fig. 13 - View of heat transfer measuring apparatus installed on HTTAT facility test cabin showing pressurized canister and pneumatic ram piston (foreground) used to insert heat transfer model into test cabin flow

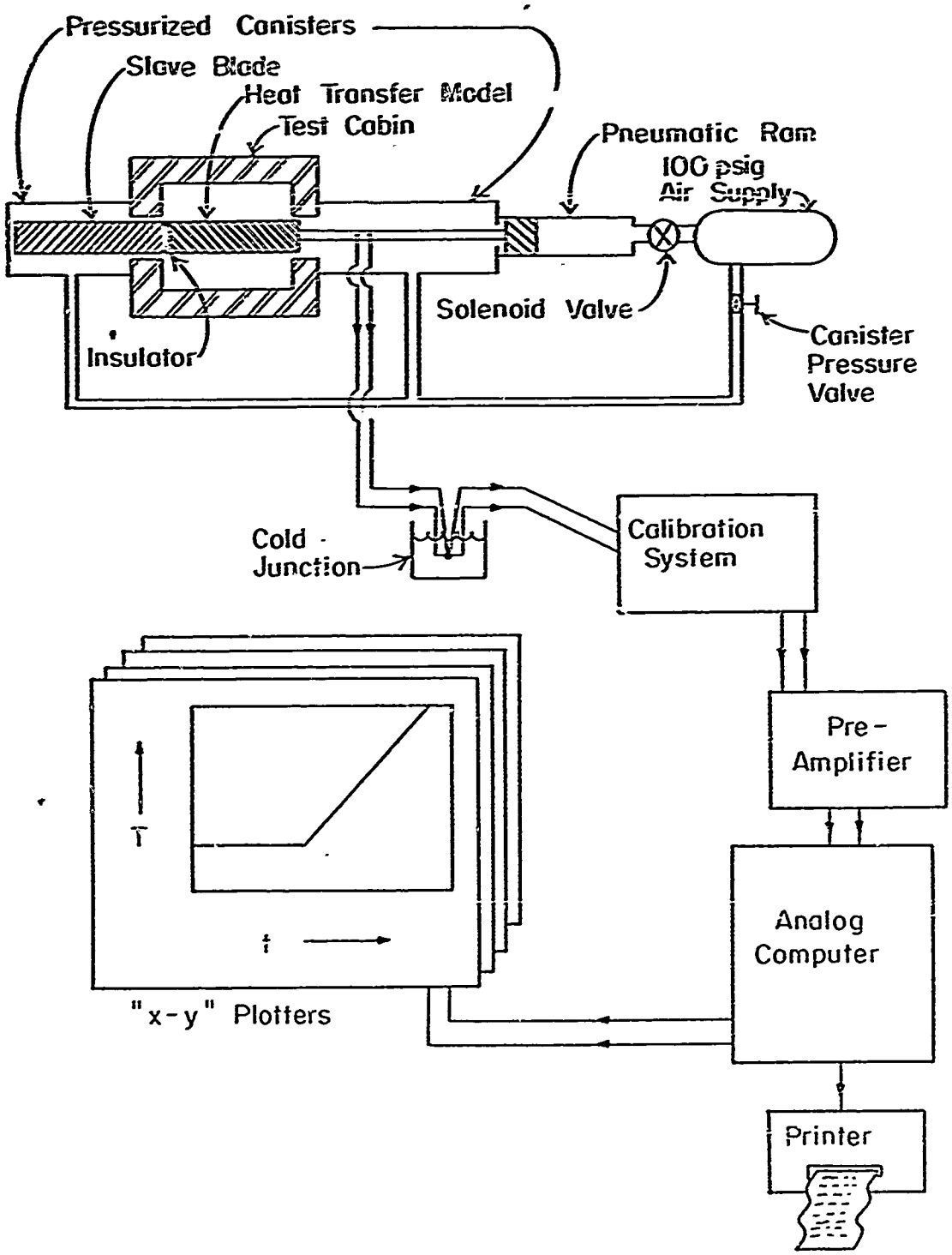

Fig. 14 - Schematic of heat transfer measurement system

Pressure measurements for the heat transfer tests were required only at the test cabin inlet for the determination of flow condition.

III. EXPERIMENTAL PROGRAM

A. DEFINITION OF THE BLOWING PARAMETER B

The present experimental technique of film cooling either or both of the turbine airfoil surfaces complicates the problem of determining an appropriate independent blowing parameter by which the film-cooling effectiveness η and the loss coefficient ω may both be indexed. The problem stems from the basic point of view by which each of the coefficients η and ω is considered. The film-cooling thermal effectiveness is classically treated as a stream-surface interaction problem and has generally been studied both analytically and experimentally as a function of stream-to-surface conditions. Thus the basic parameter in film-cooling correlations is Ms/x, where $M = (\rho u)_c/(\rho u)_e$ is the total coolant-to-freestream mass flux ratio, s is the slot height, and x is the surface distance from the coolant injection slot to the point of interest. This parameter gives no indication of the ratio of coolant-to-freestream mass flow rates, denoted here as $\xi = \dot{m}_c/\dot{m}_1$, which is the basic parameter by which turbine cooling flow losses are usually correlated in standard jet engine cycle analyses. Furthermore, if the number of surfaces cooled is a variable, as in the present study, then a common value of Ms/x for each surface corresponds to various values of ξ, depending on the number of surfaces cooled. The basic film cooling parameter Ms/x appears unsuited for the correlation of film-cooling effectiveness in the present study for one other reason also. This is the fact that, when multiple-row cooling geometries are employed, the choice of an x value to be used in the parameter is not readily apparent. Also, an x value is difficult to define when considering the use of the parameter to correlate flow losses measured aft of the airfoil. The value of M to be used in such a correlation is also not readily defined since $M = (\rho u)_c/(\rho u)_e$ is a variable over the airfoil surface due to the variation of $(\rho u)_e$.

In order to circumvent the problems outlined outlined above, a dimensionless blowing parameter has been defined for this investigation which serves as a useful parameter for examining both η and ω. Denoted as B, this blowing parameter is defined as

$$B \equiv 10^3 \frac{Fb}{c/2} \quad , \tag{9}$$

where $F = (\rho u)_c/(\rho u)_1$ the ratio of the coolant-to-inlet mass fluxes; $b = A_H/z$, the equivalent slot height for a single row of holes; and c = nominal model chord, equal to 2 inches for the present airfoil. The equivalent slot height is defined in a manner similar to that used by Papell,[9] as shown in Fig. 15. The equivalent slot height b thus defines the slot height which would pass the same coolant per unit span as does one row of the discrete holes being employed.

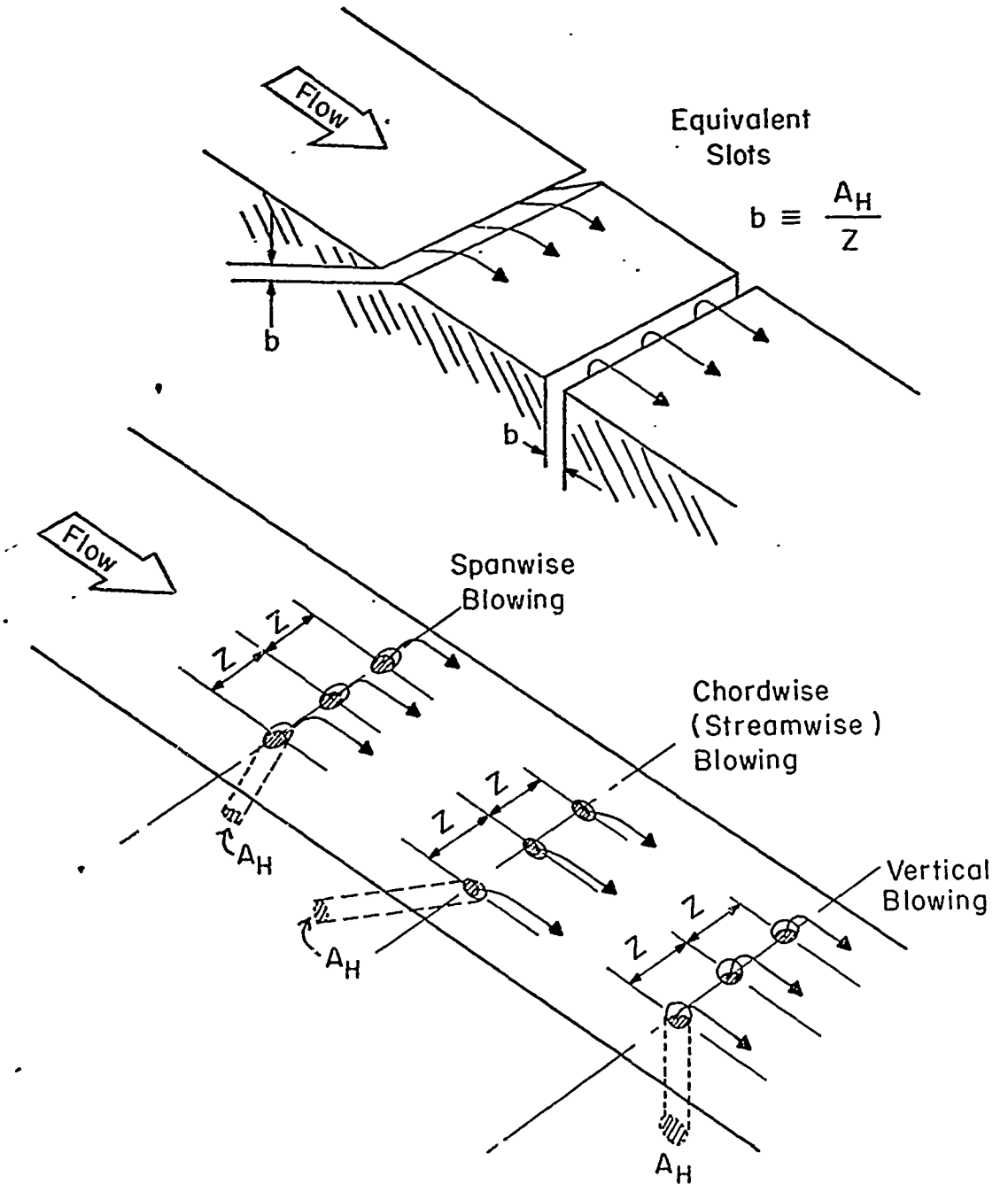

Fig. 15 - Definition of equivalent slot height (b) used in correlation of film-cooling data

A physical interpretation of B can easily be stated. Noting that $c/2$ = 1 inch, B may then be written as

$$B = 10^3 \frac{(\rho u)_c}{(\rho u)_1} \cdot \frac{(b \cdot 1)}{(1 \cdot 1)} .$$

Thus B is equal to 10^3 times the coolant mass flow rate per unit span of of the blade emanating from one row of discrete holes, divided by the inlet mass flow rate per unit inlet area. Since five rows of discrete holes are employed on both surfaces of each film cooling model, B is thus proportional at all conditions to the coolant-to-inlet mass flow rate ratio per surface per unit span. It should be noted that B is also proportional by a constant to the mass flow rate ratio ξ but the constant of proportionality is slightly different for each film-cooling model. This slight variation of the constant of proportionality arises from the fact that model fabrication problems precluded the exact satisfaction of the stipulation discussed in Section II B; namely, that equal coolant mass flow rates should correspond to equal vertical components of the coolant mass flux ratio. Figure 16 shows the proportionality between ξ and B for each of the film-cooling models for the condition of simultaneous blowing from the suction and pressure surfaces. The slope of each line in Fig. 16 is reduced by a factor of 1/2 if only one of the surfaces is film cooled.

For simplicity in later discussion, the blowing modes have been designated using upper case letters: S (suction surface cooling only), P (pressure surface cooling only), and S + P (both surfaces cooled using equal coolant mass flow rates).

B. TEST CONDITIONS

The conditions for the present investigation were chosen to simulate the environment that might be found in a high-temperature, film-cooled turbine aboard an advanced supersonic aircraft. The nominal conditions chosen for the film cooling tests were

$$P_{t_1} = 3 \text{ atmospheres}$$

$$T_{t_1} = 500°F, 1000°F$$

$$T_c = 75°F$$

with an inlet Mach number between 0.3 and 0.4. Two test cabin exit nozzles were used, resulting in inlet total-to-downstream static pressure ratios across the airfoil of P_{t_1}/P_2 = 1.5 and 1.7. These values were chosen since they gave wholly subsonic and transonic flow, respectively, over the film-cooled region of the suction surface.

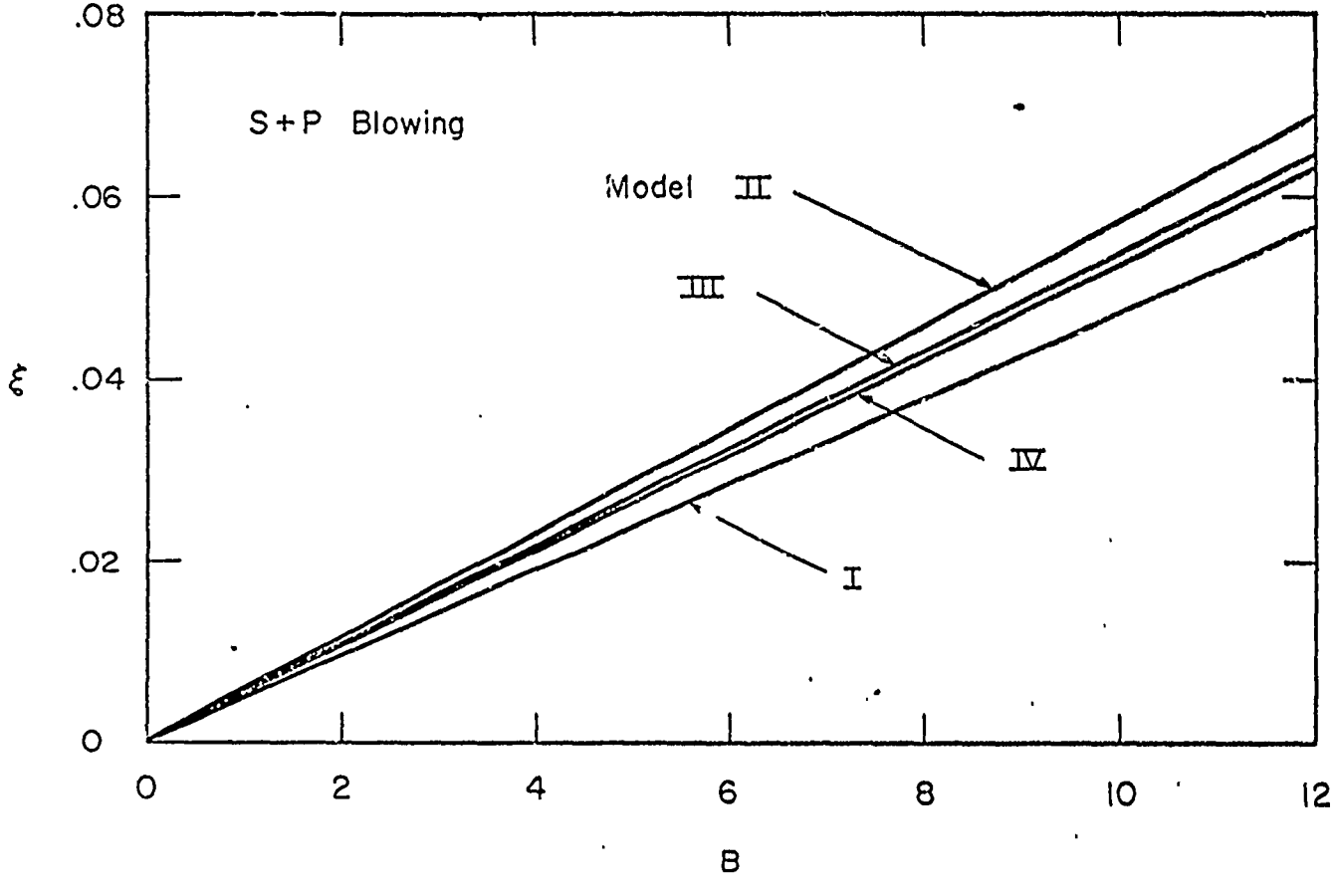

Fig. 16 - Relationship of blowing parameter B to coolant-to-inlet mass flow rate ratio ξ for S + P blowing

The inlet Reynolds number-per-foot range for the film cooling tests was

$$2 \times 10^6 < R'_{e_1} < 4 \times 10^6$$

and coolant-to-inlet flow ratios tested were in the range

$$0 \leq \xi < 0.11 \quad .$$

The design of the facility and models made it possible to film-cool each surface of the model independently, either singly or simultaneously. It was decided to test all film-cooling models with blowing from each surface alone and with blowing from both surfaces simultaneously in order to evaluate the separate effects. However, whenever both surfaces were cooled, equal coolant mass flow rates were emitted from each surface. In addition, a limited number of runs were made with Model I in which coolant was injected from the test cabin walls to simulate blowing on adjacent airfoils.

Figure 17 shows the nominal coolant velocities for the various models and their respective surfaces. These values of u_c are based on the assumption that the pressure of the coolant as it crosses the surface plane is equal to the average static pressure of the region of injection for that particular surface.

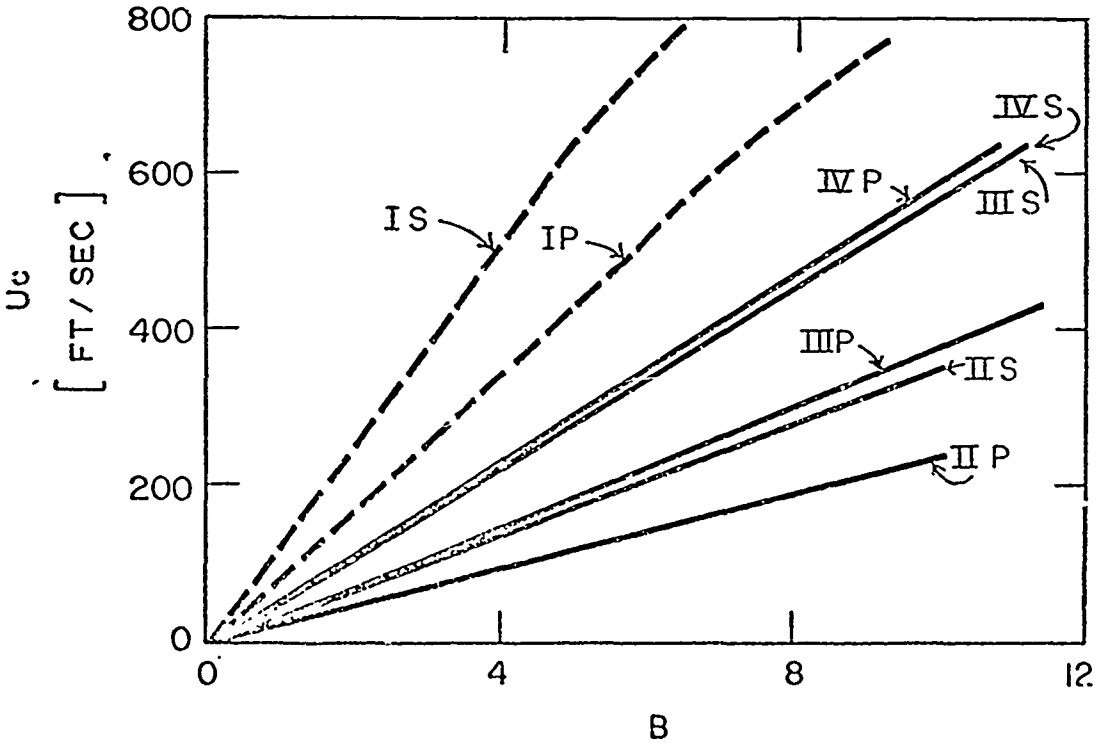

Fig. 17 - Nominal coolant velocities for film-cooling model surfaces

The no-blowing heat transfer testing was conducted at lower inlet temperatures but over a greater range of inlet pressures in order to cover the same range of R_{e_1}' as was included in the film-cooling tests. The testing range for the heat transfer experiments was

$$200°F \leq T_{t_1} \leq 400°F$$

$$23 \text{ psia} < P_{t_1} < 45 \text{ psia}$$

$$2 \times 10^6 < R_{e_1}' < 5.5 \times 10^6$$

The wall-to-total temperature ratio (T_w/T_{t_1}) was maintained in the vicinity of 0.75 to 0.80, which is commensurate with values that were measured in the film cooling tests.

C. TEST PROCEDURES

Two basically different types of tests were performed in this study; i.e., the film-cooling measurements and the no-blowing heat transfer measurements.

Film-cooling models were installed in the HTTAT Facility through the contour cutouts in the sidewall mounting plates. All model instrumentation leads (pressure, coolant, and thermocouple) were brought through the blade ends and the remainder of the cutout was then filled with high-temperature insulating cement to both hold the blade in position and provide a sealant against leaks. The facility test cabin was virtually assembled around each film-cooling model and then attached to the heater via the transition section. This precluded visual inspection of the model or total pressure probes between assembly and disassembly. The models and probes were carefully checked visually for any structural damage both before and after testing. Only the characteristic discoloring of stainless steel resulting from exposure to elevated temperatures was observed. Total pressure probes of 1/16-inch diameter stainless steel were employed and no evidence of probe bending or vibration was found either during or after the testing.

A typical test of a film-cooling model was always preceded by a calibration of the pressure-sensing system used to survey the wake total pressure. Once the system had been calibrated, primary air flow was begun, the flow was brought to the correct stagnation pressure and temperature, and the automatic control system then assumed control to maintain constant flow conditions. A series of blowing conditions were then tested, usually beginning and ending with a no-blowing condition. At each condition, after waiting a period of 10 to 15 seconds for complete thermal and pressure equilibrium to be achieved, the wake survey was made. About one minute was the usual time to traverse the

1-inch height of the channel downstream of the airfoil trailing edge. Once the probe had been withdrawn from the flow, the static pressure manometer bank was sealed and the 16-point Brown recorder tripped to record the airfoil temperatures. The static pressures could then be read from the sealed manometer bank as the coolant flow rate was changed for the next blowing condition.

Test procedures for the no-blowing heat transfer measurements were identical to those for the film-cooling tests with regard to facility start-up and control of primary flow conditions. The mercury manometer bank was used only to check static pressures in the test cabin since inlet stagnation and static pressures were measured by pressure transducers using the same pressure measurement system as was used for the film-cooling tests. Each of the four thermocouples was calibrated independently prior to and after a test run. No wake total pressure surveys were conducted during the heat transfer phase of the investigation.

The slave blade was positioned in the flow and the heat transfer model located in the sealed canister while the inlet flow was brought to the desired conditions. As the flow pressure was increased during start-up, the pressure supply to the sealed canisters on the facility sidewall was correspondingly raised to prevent hot test cabin air from entering the canister containing the heat transfer model since it was necessary to keep the model as cool as possible prior to insertion. The model was somewhat heated by conduction from the slave blade, but the insulator connecting the two reduced this considerably. When model temperature did rise above tolerable levels during extended operating times, the air supply to the canisters was temporarily increased to cool the model. The contour cutout in the sidewall through which the model entered and the slave blade exited the test cabin was only 0.002 inch larger in overall clearance than the model profile, resulting in negligible air flow between canisters and test cabin as long as pressure differentials were held within 5 psi.

The "x-y" plotter pen travel was begun one to three seconds before model insertion, depending on the time base being employed. Pen speeds of 1 to 3 inches per second were used to traverse the 15-inch-wide chart paper. Following the recording of the initial temperature rise, the model was allowed to remain in the flow until the rate of skin temperature increase, as shown on the analog computer's digital voltmeter, had fallen to approximately 1°F per minute. These terminal values were then recorded as adiabatic wall temperatures (T_{aw}) for subsequent heat transfer calculations.

D. DATA REDUCTION

Standard laboratory procedures were used to reduce all manometer tube pressure data, and calibration information for all pressure transducers was entered into the analog computer to enable direct computer

output in psia and/or ratio form. Two data reduction procedures deserve mention at this point. These are the methods of integrating the wake total pressure loss and the manner in which no-blowing heat transfer was inferred from the transient temperature time histories.

The previous discussion of the wake total pressure measuring system (Section II C) pointed out that the data output of the analog computer was in the form $(P_{t_1} - P_{t_2})/P_{t_1}$ vs. y, a plot of the nondimensional total pressure defect across the wake as a function of the position coordinate normal to the flow. The total pressure loss coefficient is defined for this investigation as

$$\omega \equiv \int_{-0.3}^{+0.3} \frac{P_{t_1} - P_{t_2}}{P_{t_1} - P_2} \, d\left(\frac{y}{y_2}\right) \tag{10}$$

where y_2 is the height of the channel, equal to one inch. The integration distance was chosen to be ± 0.3 inch from the channel centerline in order to include that portion of the wake affected by the airfoil but avoid the regions containing the boundary layers of the test cabin walls. Thus ω may be written as

$$\omega = \int_{-0.3}^{+0.3} \frac{(P_{t_1} - P_{t_2})/P_{t_1}}{(P_{t_1} - P_2)/P_{t_1}} \, d\left(\frac{y}{y_2}\right) \quad , \tag{11}$$

and under the assumption of constant static pressure across the wake, Eq. (11) becomes

$$\omega = \left\{ \int_{-0.3}^{+0.3} \frac{(P_{t_1} - P_{t_2})}{P_{t_1}} \, d\left(\frac{y}{y_2}\right) \right\} \Big/ 1 - \frac{P_2}{P_{t_1}} \quad . \tag{12}$$

Equation (12) shows that the "x-y" plotter output could be integrated directly and used to calculate ω, which was done using a planimeter.

The transient thin-skin thermometry method of measuring heat transfer allows the calculation of the surface heat transfer to the thin skin by knowledge of the skin properties and the initial slope of the temperature vs. time plot. The heat balance equation which applies is

$$\dot{q} = C_M \rho_M L \frac{dT}{dt} \quad , \tag{13}$$

where

$\dot{q}$ = heat transfer rate per unit surface area,

C_M = specific heat of the metal skin,

ρ_M = metal density,

L = metal thickness,

T = metal temperature, and

t = time.

The values used for the stainless steel skin employed on the heat transfer models were

$$C_M = 0.120 \text{ Btu/lb}_m{}^\circ\text{F} \quad ,$$

$$\rho_M = 0.290 \text{ lb}_m/\text{in.}^3 \quad , \text{ and}$$

$$L = 0.010 \text{ inch} \quad .$$

Values of dT/dt were obtained by measuring the initial slope of the plotter output and using standard copper-constantan thermocouple tables. Differentiation of the transient temperature output was not performed by the analog computer since any filtering would have decreased the time response.

IV. EXPERIMENTAL RESULTS

A. STATIC PRESSURE DISTRIBUTIONS

Static pressures were measured at a minimum of 10 surface locations on all film-cooling models for inlet stagnation temperatures of 500°F and 1000°F and a variety of blowing conditions. The complete static pressure data are presented in Tables III - XIII (Appendix C) and only the data obtained at T_{t_1} = 1000°F are shown in Figs. 18 - 29. Distributions obtained at the lower stagnation temperature of 500°F are essentially the same as those shown in these figures. Curves have been faired through the data points except where the resultant crowding would be confusing. In such cases only the no-blowing distribution is represented by a curve.

Figures 18 - 21 show a marked departure of the pressure distribution on the suction surface of Model I (12° spanwise blowing) from those measured on the other models. This irregularity was at first thought to be a fault of the measurement system, but extensive checking of the manometer bank and pressure lines, plus additional test runs, revealed that such a variation does indeed occur. Possible reasons for this irregularity are discussed in Section IV. Figures 18 - 21 present data for Model I obtained with four different blowing modes. The normal modes of S, P, and S + P blowing were tested on all models, however, Fig. 21 presents data obtained during blowing from both the model and the contoured test cabin walls to simulate the effect adjacent film cooled blades. Figures 22-29 show static pressure distributions on Models II (90° blowing), III (30° spanwise blowing), and IV (20° spanwise P blowing and 30° chordwise S blowing). Since Model IV was the only model tested possessing dissimilar S and P blowing geometries, plots are presented showing both S and S + P blowing for this model. Throughout the testing program it was observed that P blowing has a negligible effect on the static pressure distribution, hence only S blowing data are presented graphically for Models II and III, in Figs. 22 - 25. Data are presented for Models II, III, and IV for the two blade pressure ratios, P_{t_1}/P_2 = 1.5 and 1.7. Bearing in mind that for γ = 1.4 the sonic P/P_t is 0.53, the no-blowing data show that for P_{t_1}/P_2 = 1.5 the suction surface is wholly subsonic. Suction surface flow is transonic for P_{t_1}/P_2 = 1.7 although in the region of the rows of coolant holes ($0.93 \leq x \leq 1.91$ inches) the flow is wholly supersonic for the no-blowing condition.

Since all static pressure data were obtained using standard manometer techniques at pressures which gave relatively large mercury column deflections of between 10 and 50 inches, the accuracy of the data can be placed at approximately ± 1%, limited primarily by the ability of the observer.

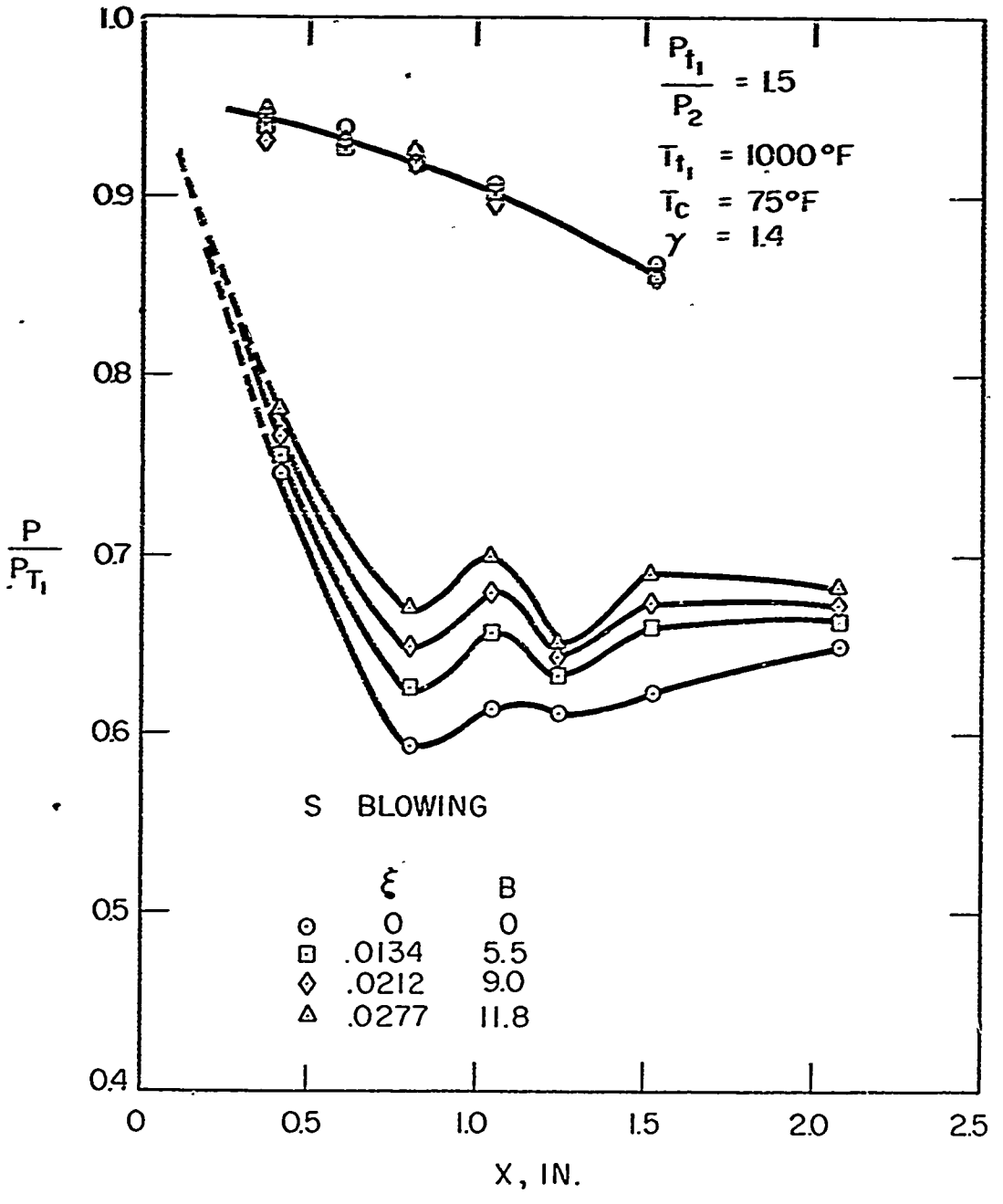

Fig. 18 - Static pressure profiles for S blowing on Model I (12° spanwise blowing)

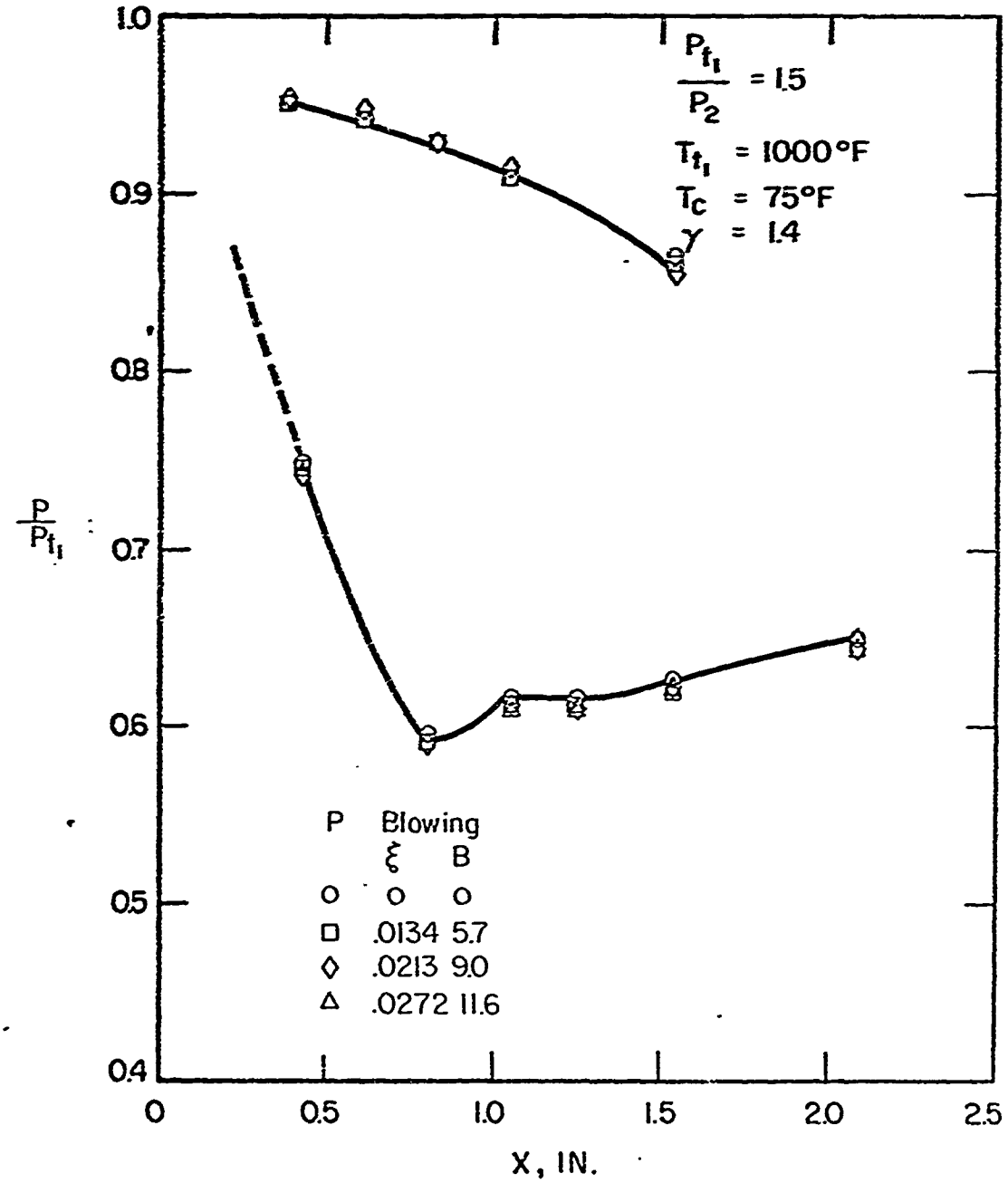

Fig. 19 - Static pressure profiles for P blowing on Model I (12° spanwise blowing)

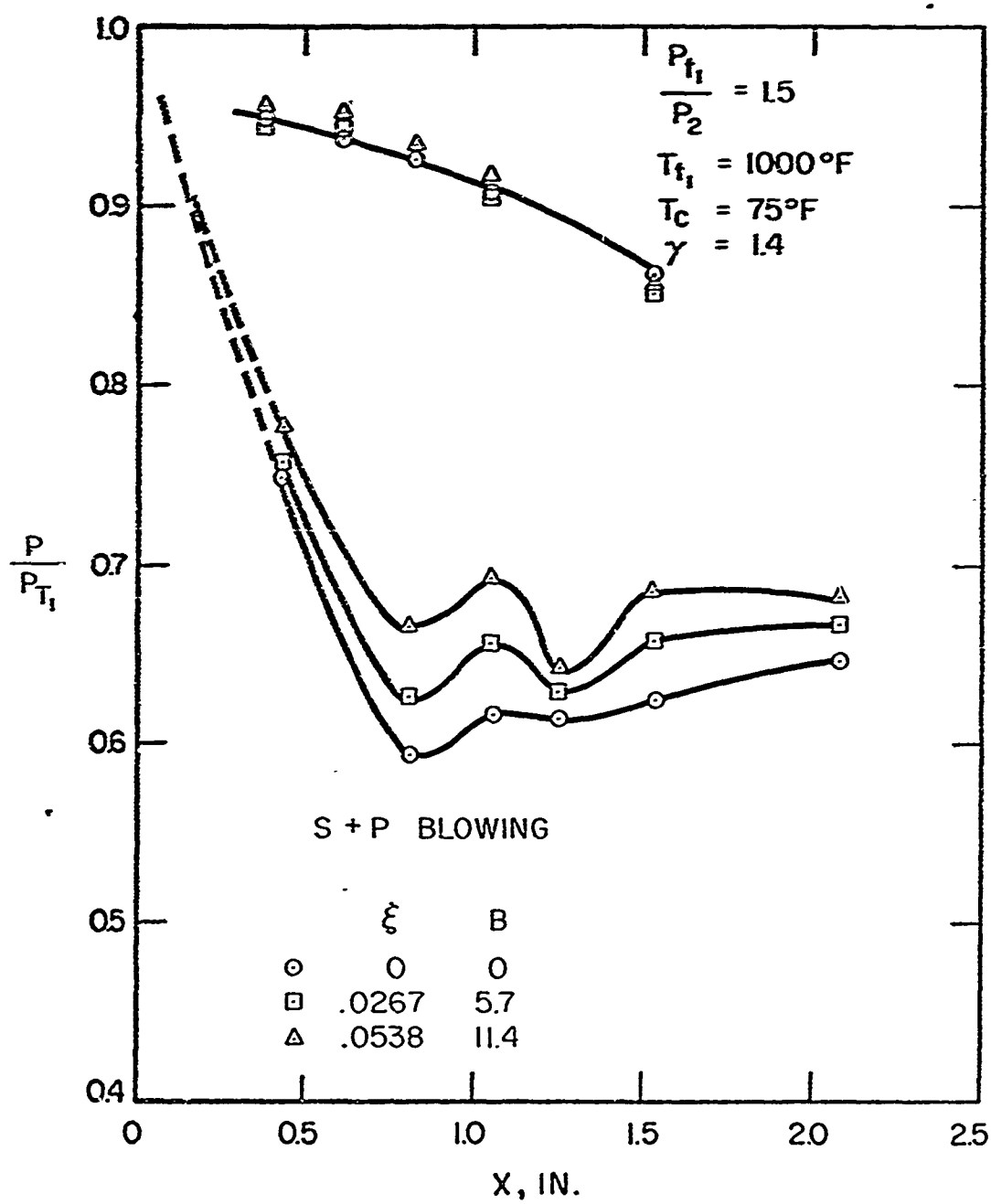

Fig. 20 - Static pressure profiles for S + P blowing on Model I (12° spanwise blowing)

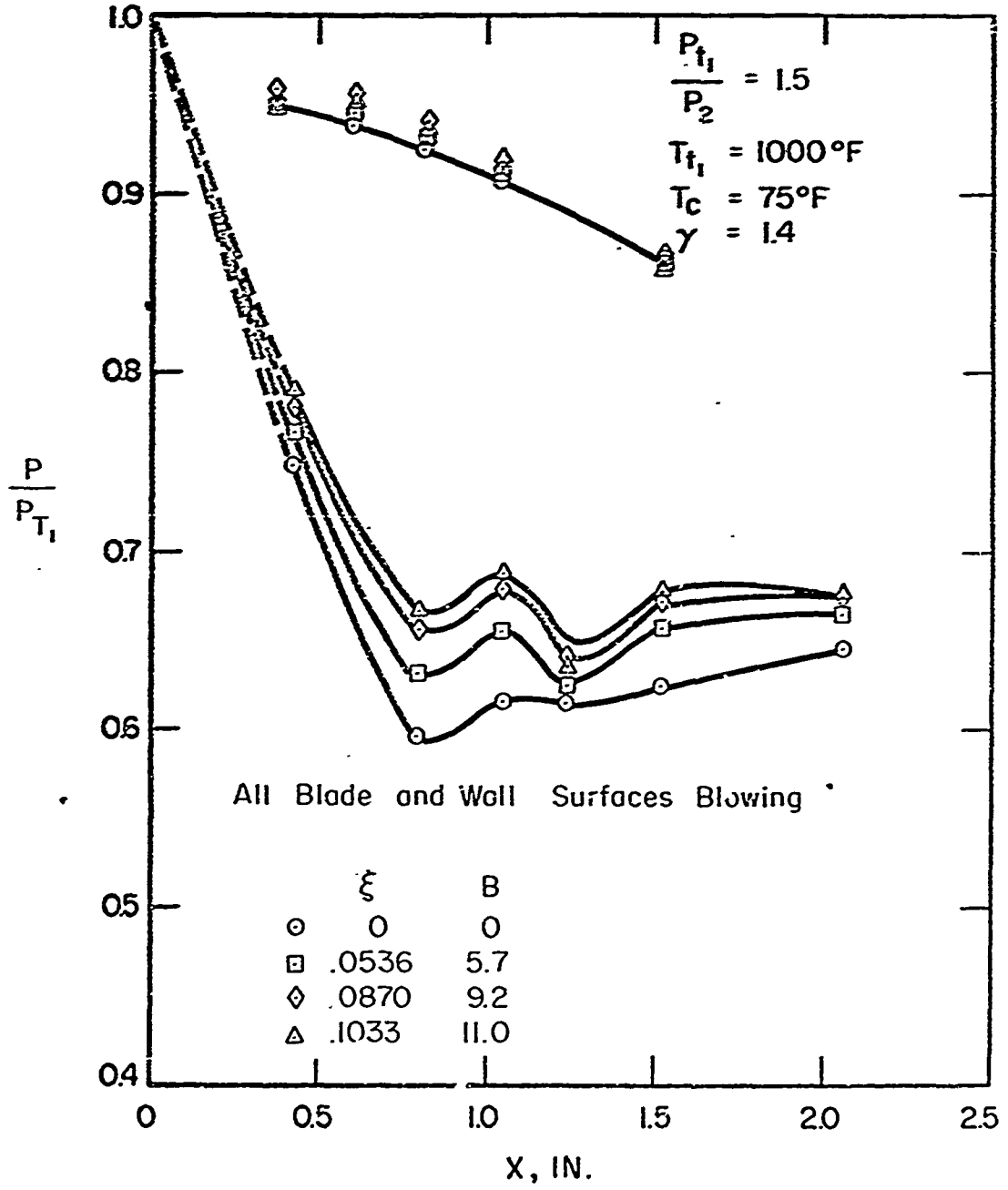

Fig. 21 - Static pressure profiles for S + P and test cabin wall blowing on Model I (12° spanwise blowing)

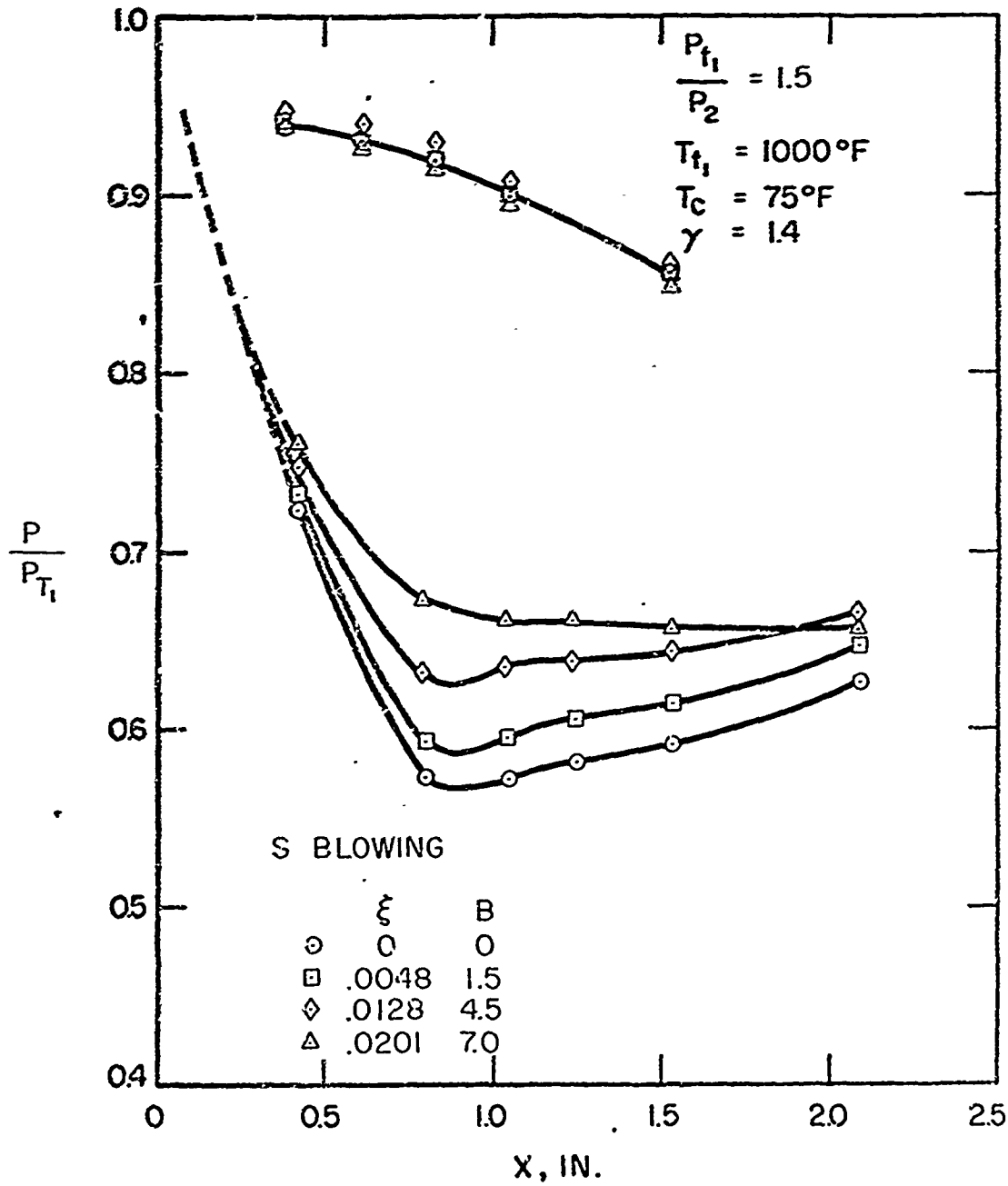

Fig. 22 - Static pressure profiles at $P_{t_1}/P_2 = 1.5$ for S blowing on Model II (90° blowing)

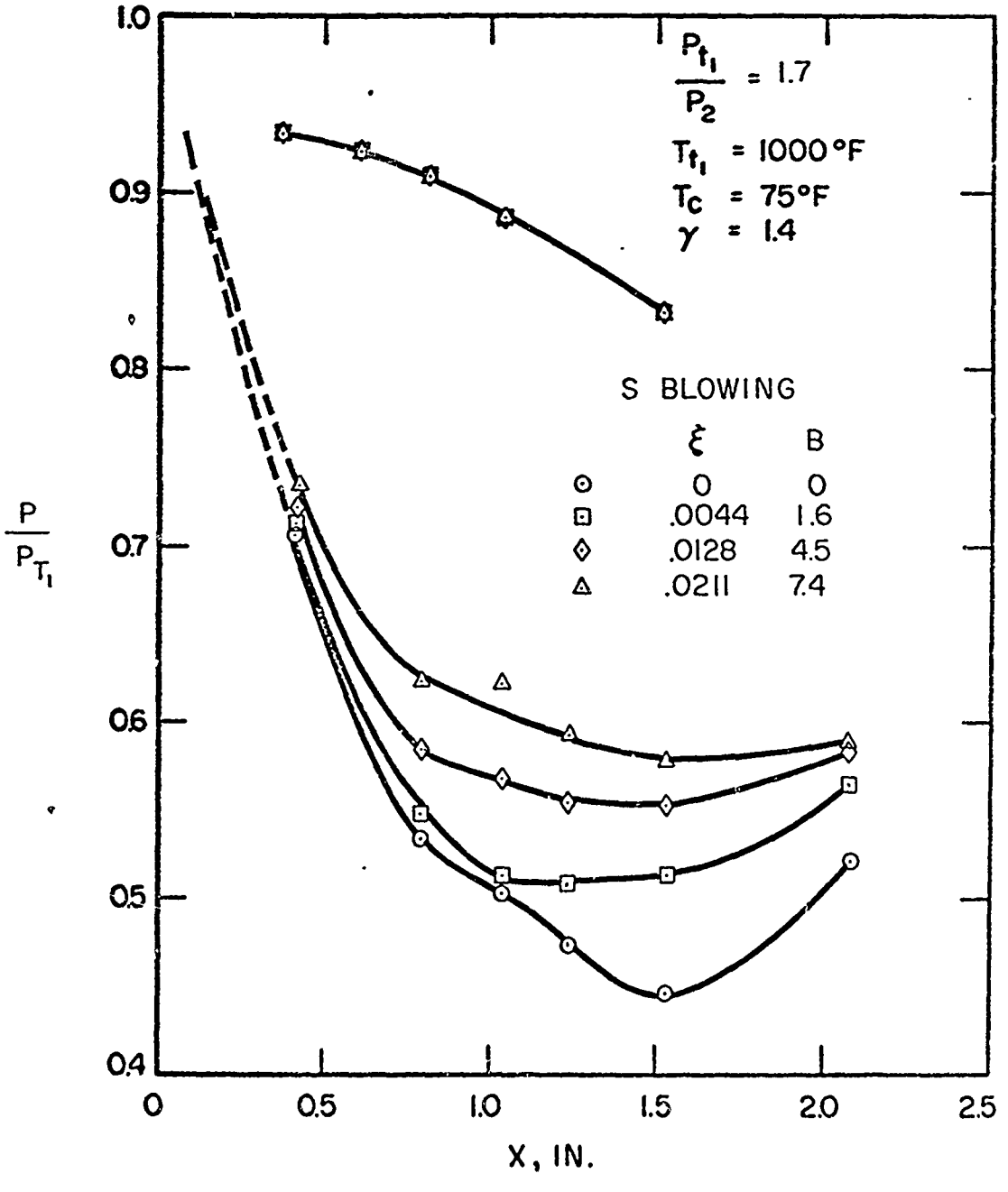

Fig. 23 - Static pressure profiles at $P_{t_1}/P_2 = 1.7$ for S blowing on Model II (90° blowing)

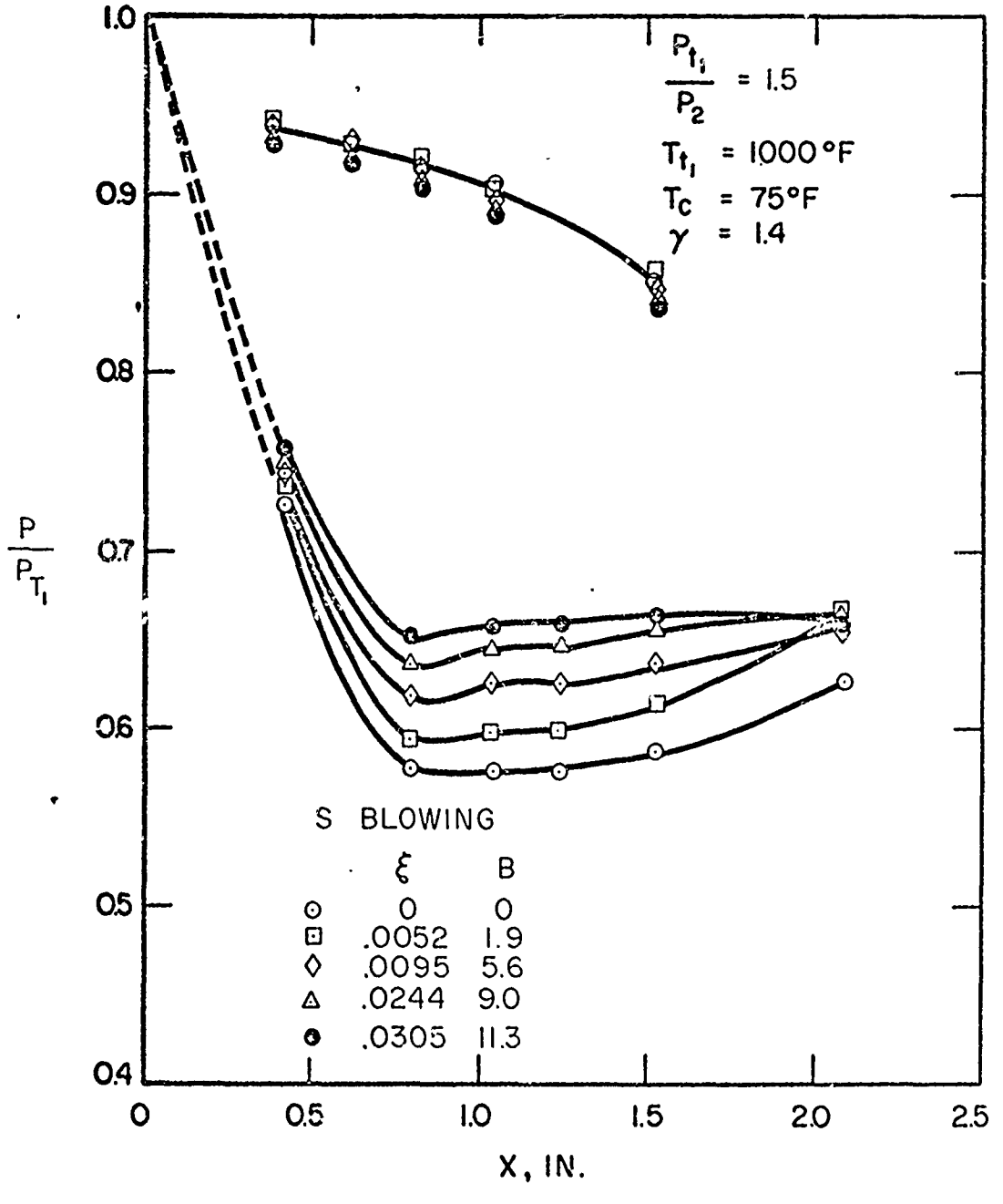

Fig. 24 - Static pressure profiles at $P_{t_1}/P_2 = 1.5$ for S blowing on Model III (30° spanwise blowing)

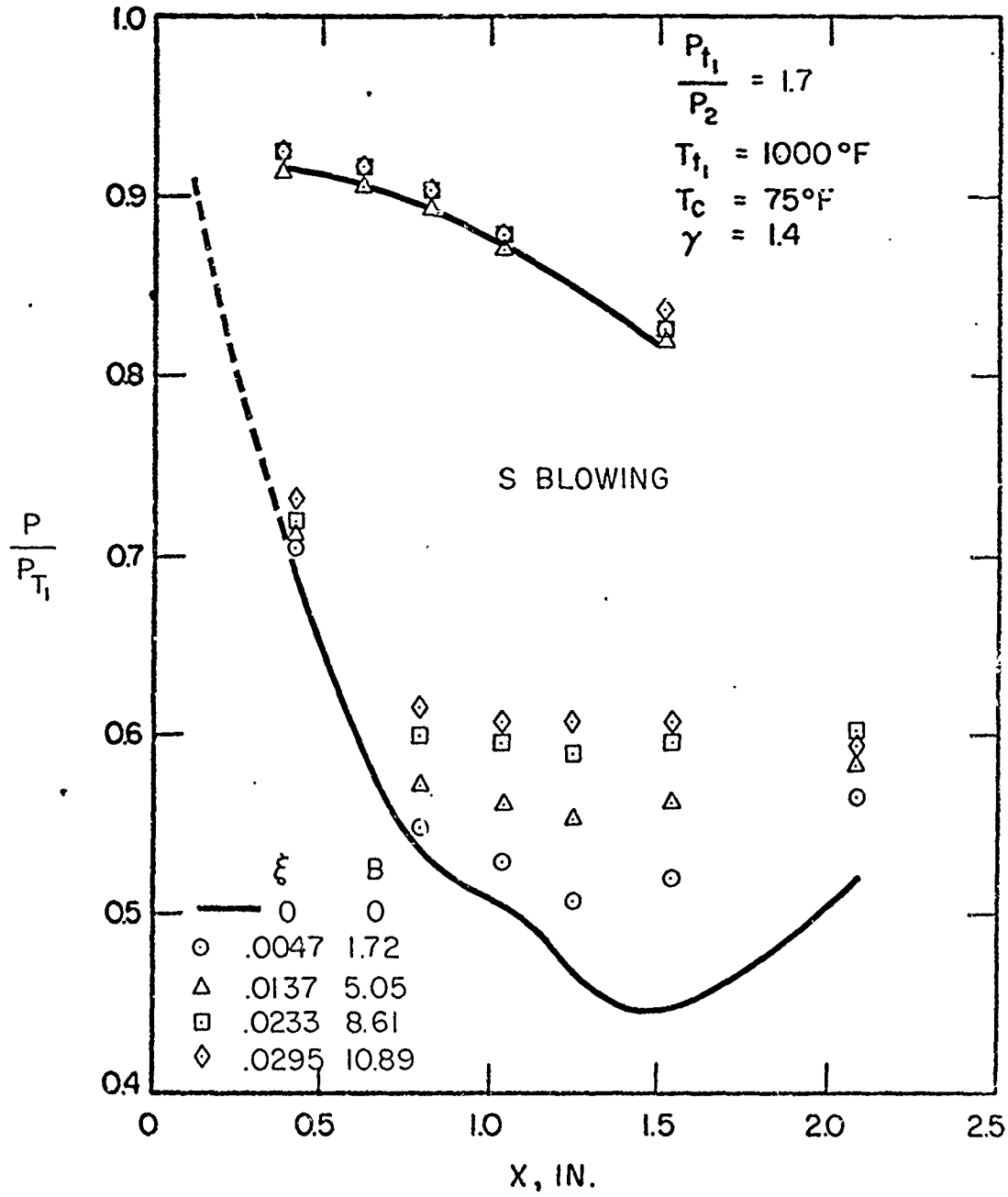

Fig. 25 - Static pressure profiles at P_{t_1}/P_2 = 1.7 for S blowing on Model III (30° spanwise blowing)

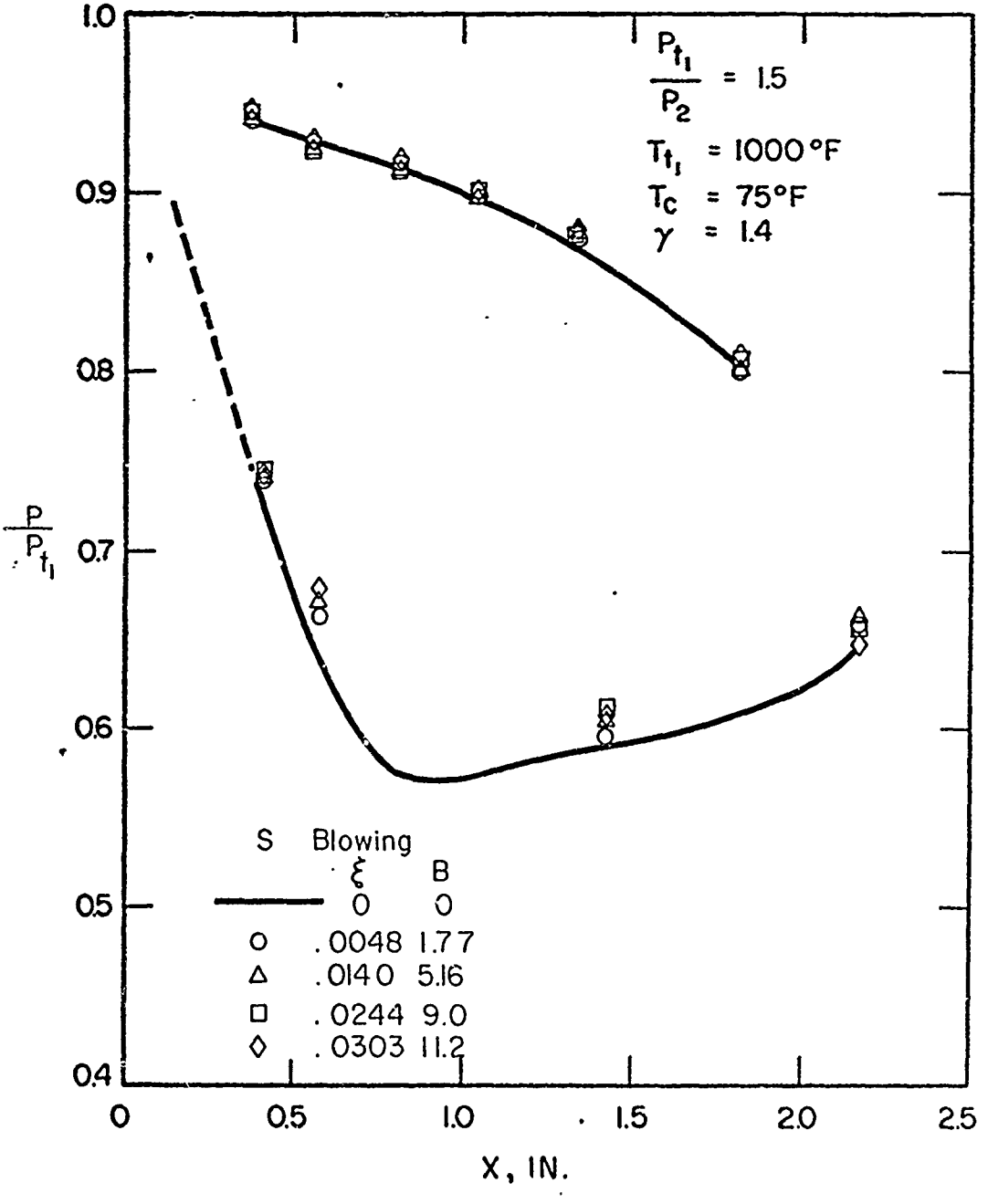

Fig. 26 - Static pressure profiles at $P_{t_1}/P_2 = 1.5$ for S blowing on Model IV (30° chordwise blowing)

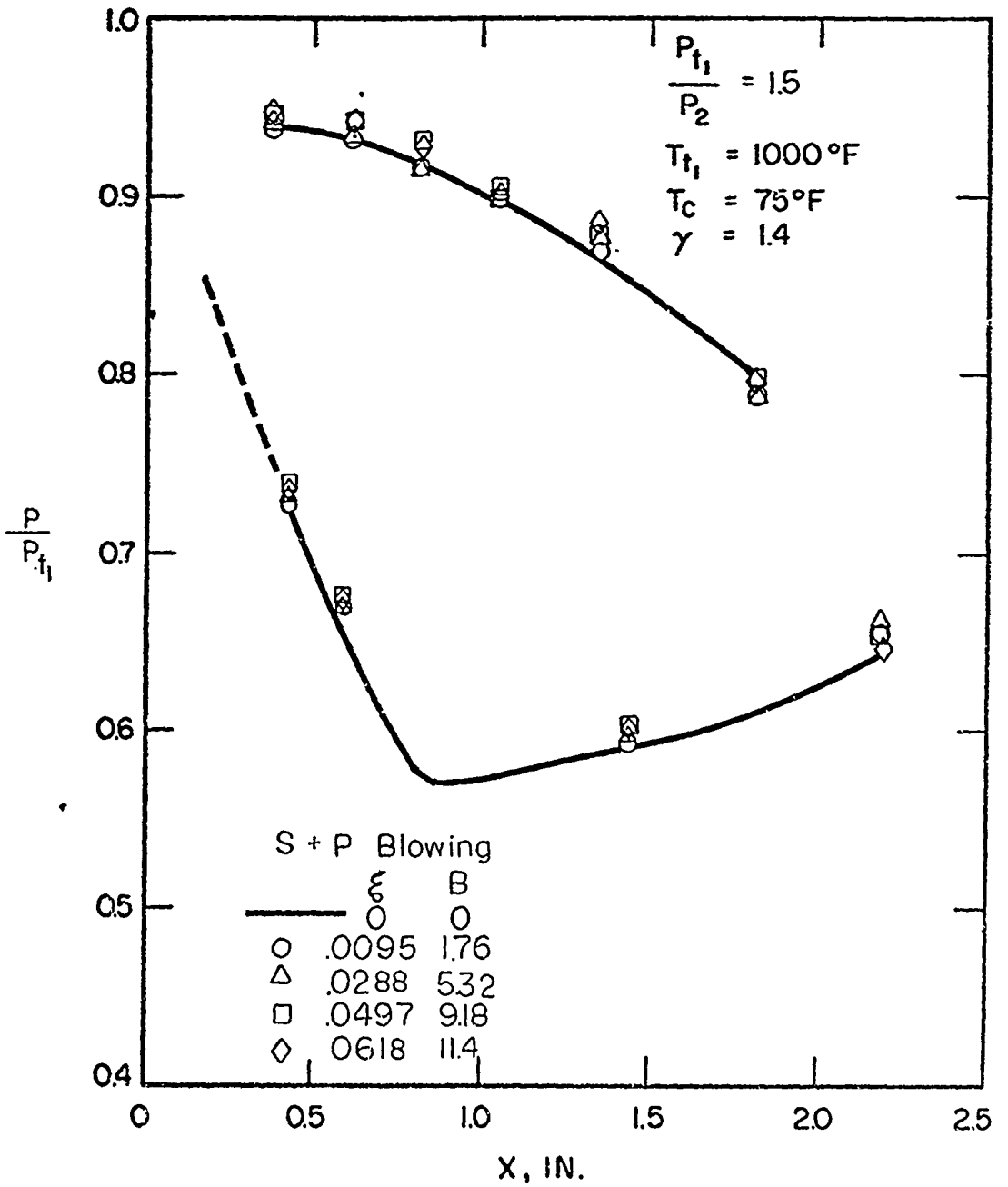

Fig. 27 - Static pressure profiles at $P_{t_1}/P_2 = 1.5$ for S + P blowing on Model IV (30° chordwise S blowing and 20° spanwise P blowing)

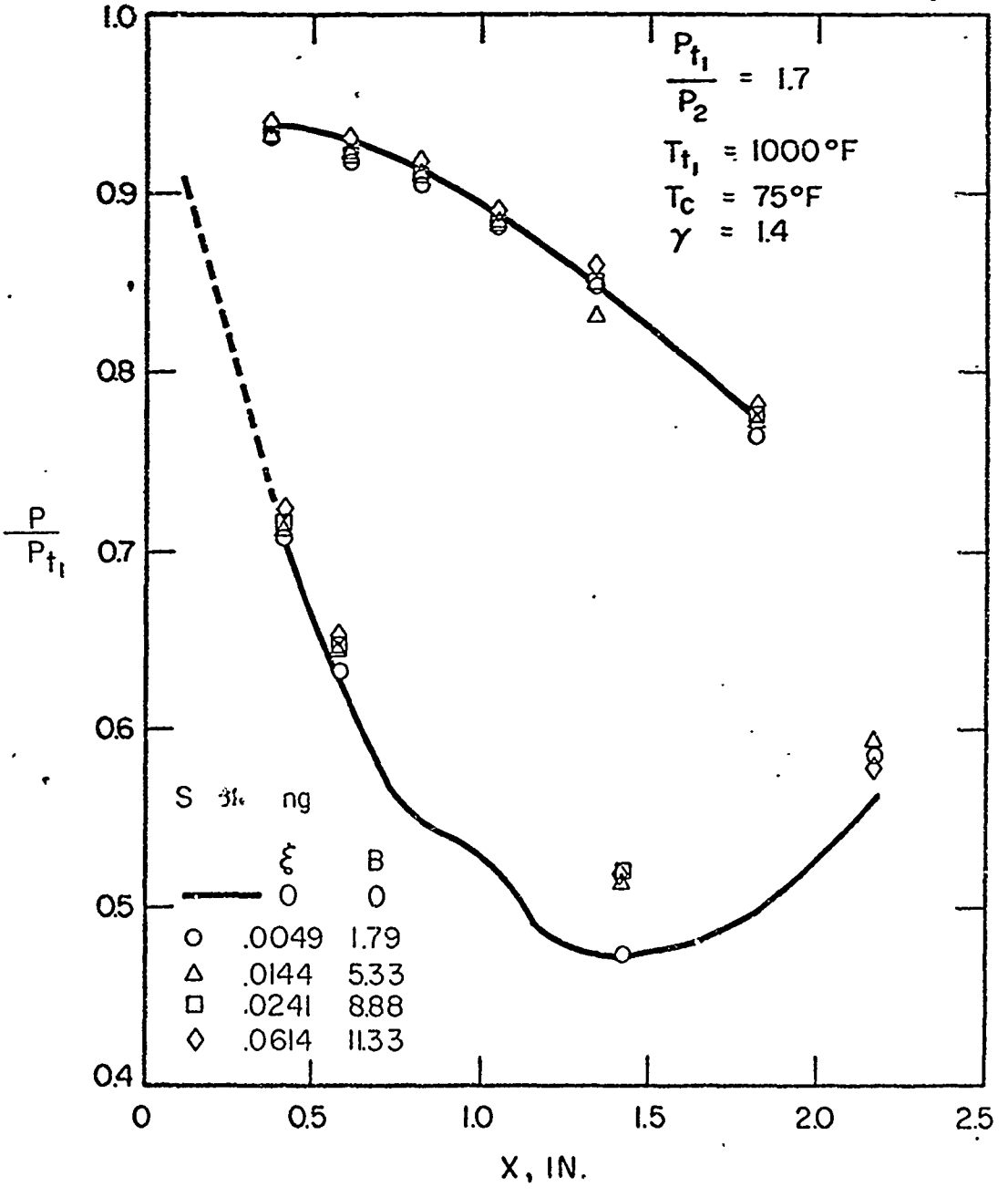

Fig. 28 - Static pressure profiles at $P_{t_1}/P_2 = 1.7$ for S blowing on Model IV (30° chordwise blowing)

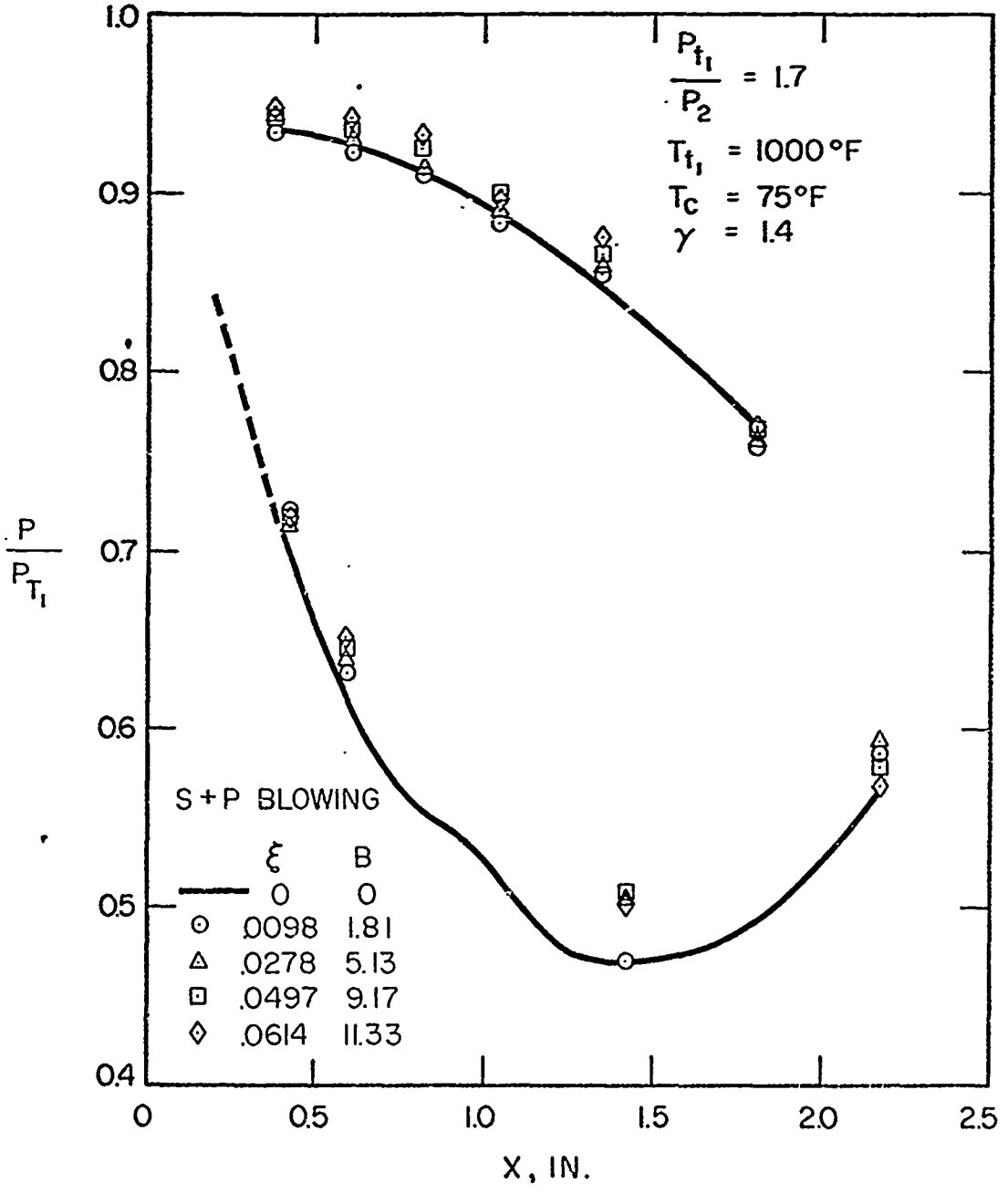

Fig. 29 - Static pressure profiles at $P_{t_1}/P_2 = 1.7$ for S + P blowing on Model IV (30° chordwise S blowing and 20° spanwise P blowing)

B. WAKE TOTAL PRESSURE DATA

Surveys of the wake total pressure were obtained at a distance 0.63 inch downstream of the trailing edge for all film-cooling models. Surveys were made for both of the tested blade pressure ratios and at inlet total temperatures of both 500°F and 1000°F. These data were received in the nondimensional form shown in Figs. 30 and 31, which show actual surveys obtained at large mass addition rates. Integrals of the measured wake total pressure surveys are shown in Figs. 32 for the T_{t_1} = 1000°F and P_{t_1}/P_2 = 1.5 conditions. These values are indicative of the loss coefficient ω since they differ from the coefficient by the factor $(1 - P_2/P_{t_1})$, which is essentially a constant determined by the size of the exhaust nozzle of the test cabin. Values of the measured integrals and the corresponding loss coefficients are presented for all tested conditions in Tables XIV - XXV. The accuracy of the results was limited primarily by the flow fluctuations which were evident in many of the runs. These variations could not be removed by filtering since rapid time response of the pressure measurement system had to be maintained if survey times were to be kept reasonably short (1 minute). However, survey profiles were found to be repeatable within ±5% of the peak value.

C. FILM-COOLING TEMPERATURE MEASUREMENTS

Thermocouples located within each film-cooling model were monitored to evaluate the steady state cooling of each model. Temperatures at various stations along the model camber line were recorded for the testing of Model I. Both camber line and surface temperatures were monitored for the remaining models in order to determine the significance of both the internal cooling and the conduction of heat from the uncooled surface when only one airfoil surface was film cooled. Figure 33 presents typical chordwise temperature distributions along the camber line of Model I. Such data are useful primarily in examining the overall cooling of the airfoil and, as seen in Fig. 33, show that as coolant flow rates are increased, the gains in cooling become smaller in terms of actual temperature reduction.

Temperature data obtained from the thermocouples located within 0.010 to 0.025 inch of the suction surfaces of Models II, III, and IV gave a more valid indication of the film-cooling effectiveness and are the data used in the film-cooling analysis of this investigation. Figure 34 shows typical suction surface temperature profiles for both S and S + P blowing on Model II. The data show that suction surface temperatures are considerably reduced when S blowing is modified to S + P blowing. This reduction results in large part from the reduction of heat conduction through the blade from the uncooled pressure surface, but is also partly a result of additional internal cooling. Thus the data obtained from the suction surface thermocouples should not be interpreted as true film-cooling adiabatic wall temperatures. This point,

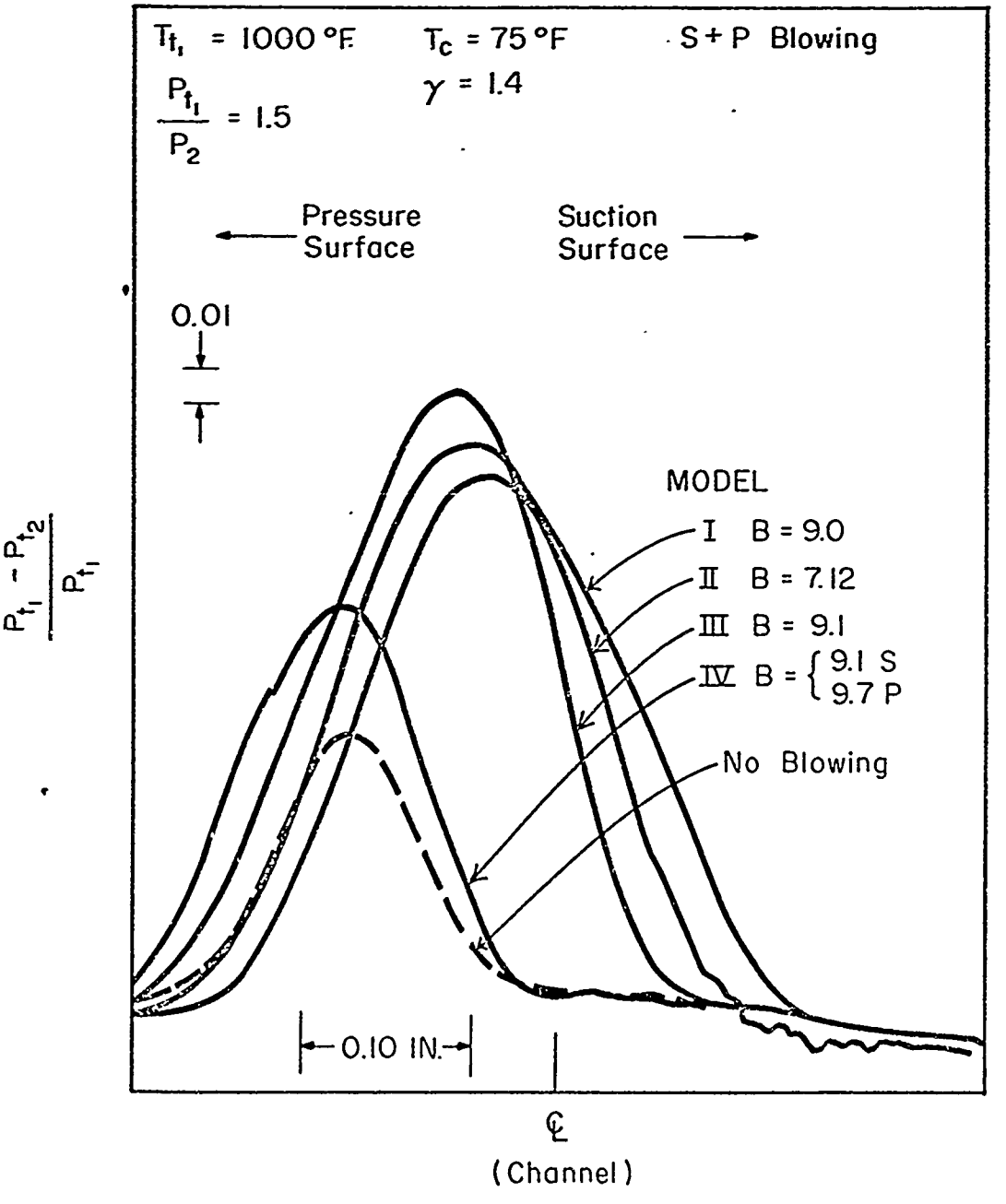

Fig. 30 - Typical wake total pressure surveys for massive blowing at $P_{t_1}/P_2 = 1.5$

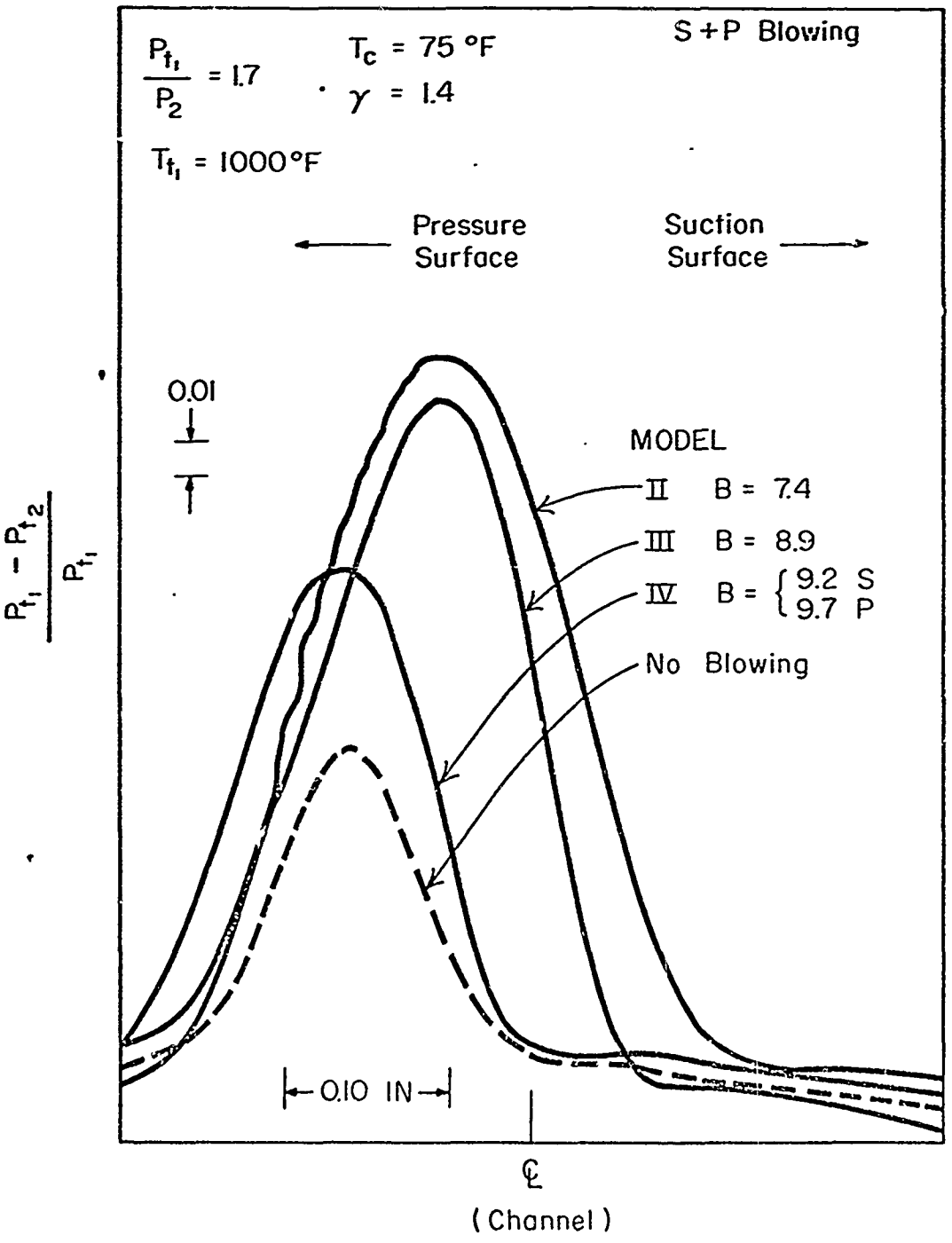

Fig. 31 - Typical wake total pressure surveys for massive blowing at $P_{t_1}/P_2 = 1.7$

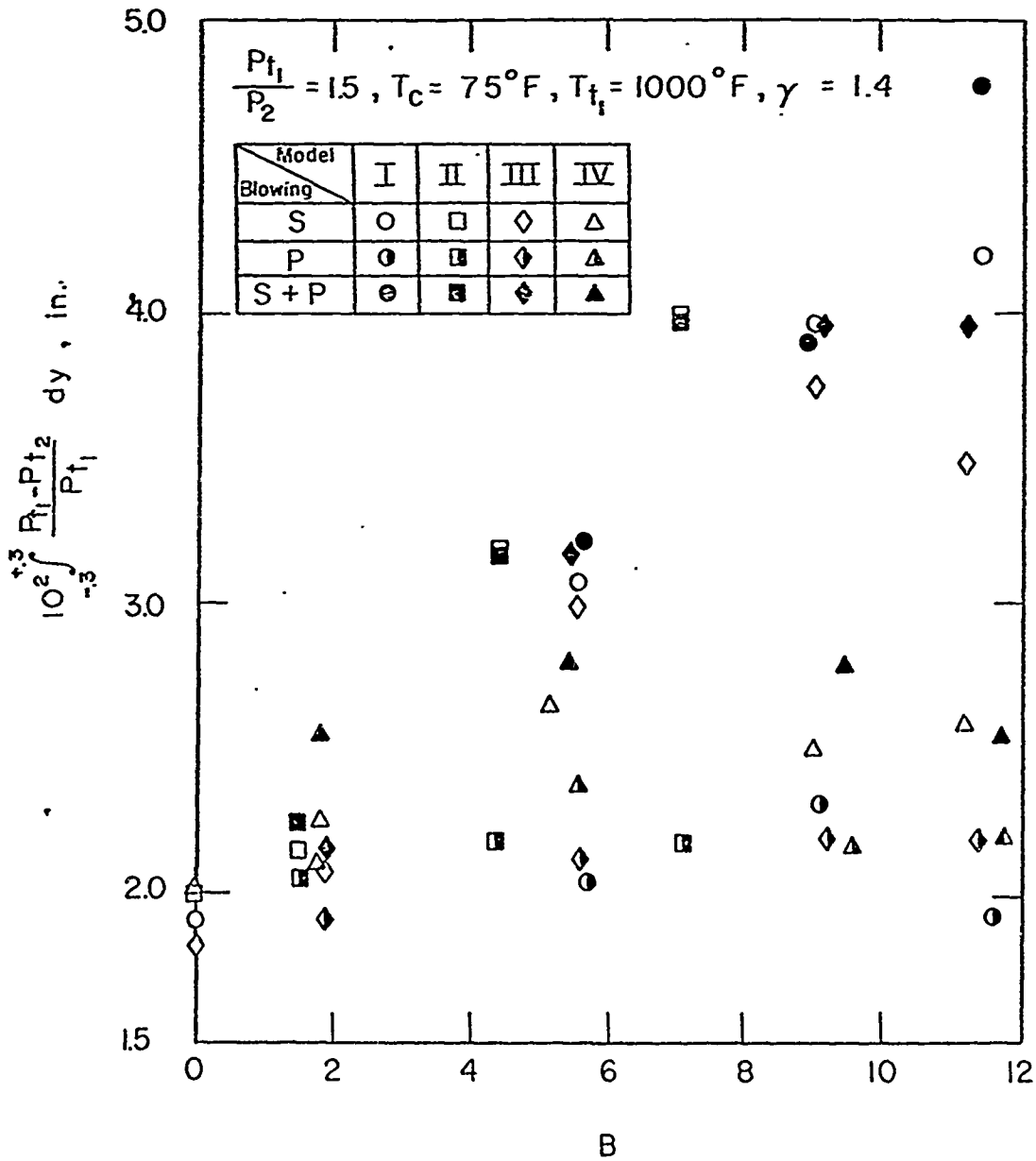

Fig. 32 - Measured wake total pressure defects for P_{t_1}/P_2 = 1.5

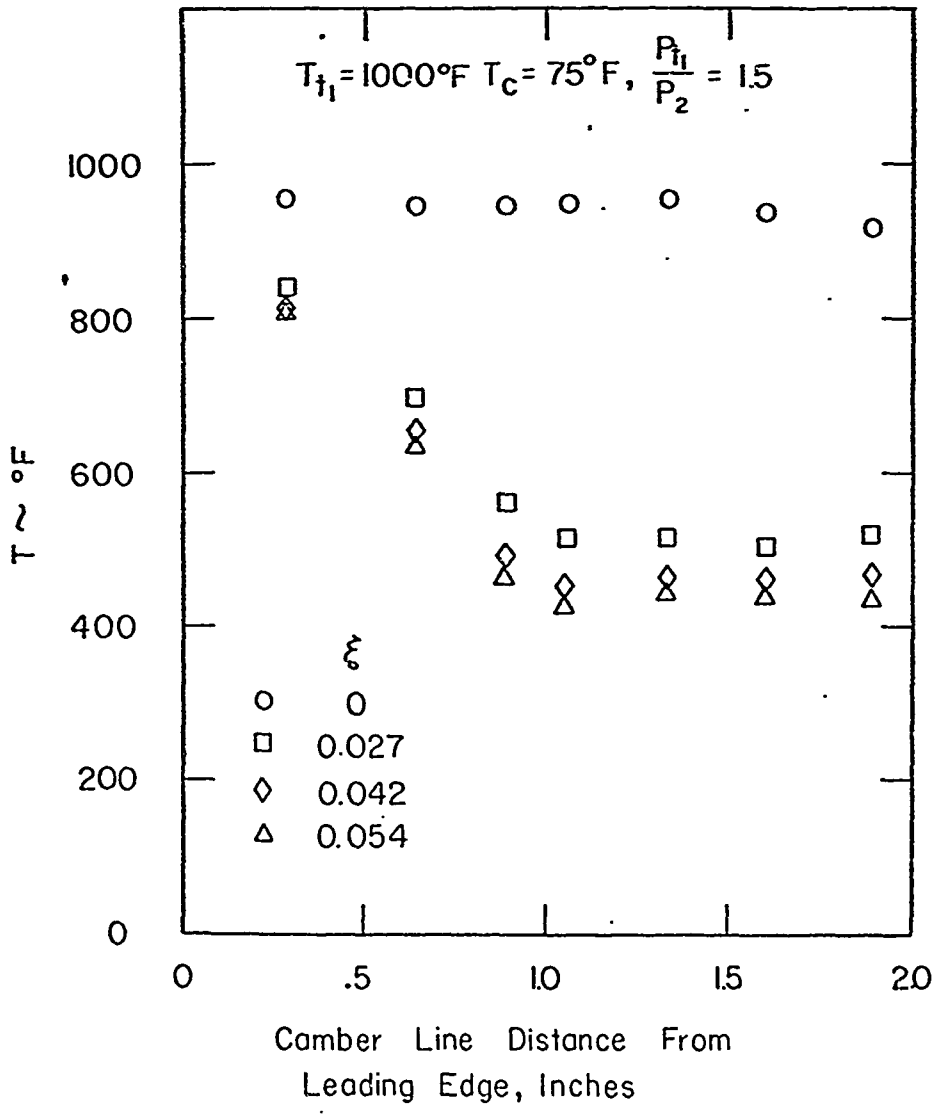

Fig. 33 - Effect of massive S + P blowing on temperature along camber line of Model I (12° spanwise blowing)

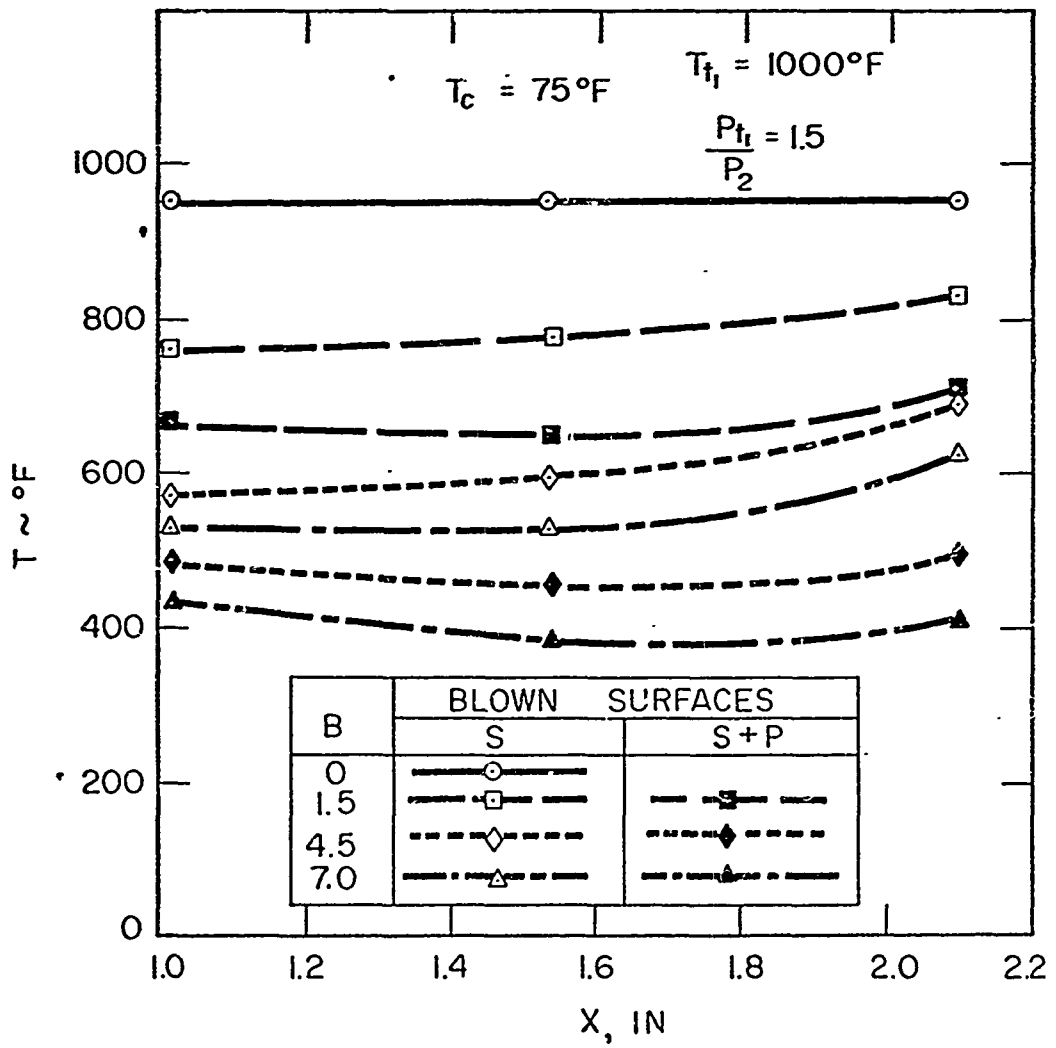

Fig. 34 - Suction surface temperature profile for S and S + P blowing on Model II (90° blowing)

along with the interpretation of the temperature data is further amplified in Section V. An accuracy of ± 5°F may be ascribed to the temperature data, which are presented in Tables XXVI - XXXVII.

D. NO-BLOWING HEAT TRANSFER DATA

Heat transfer rates measured in the absence of film cooling by the previously described transient technique are presented in Tables XXXVIII-XL. Typical surface distributions of the heat transfer in coefficient form are shown in Figs. 35 - 37. The data are shown in the more useful form of the Stanton number in Figs. 38 - 41, where it is seen that a turbulent boundary layer existed over much of the airfoil surface. The data exhibit the customary scatter which is characteristic of transient heat transfer measurements. Considerably more scatter is found in the $P_{t_1}/P_2 = 1.5$ suction surface measurements, which were the final measurements taken, than in the data obtained at $P_{t_1}/P_2 = 1.7$. This increase in scatter is probably attributable to a weakening of the thermocouple-to-model bond, which eventually caused several thermocouples to separate from the thin metallic skin, terminating the measurements. Because of the above problem, and the fact that some chordwise conduction must occur in the thin skin of a model, an accuracy of no more than ±10% can be stated for these data.

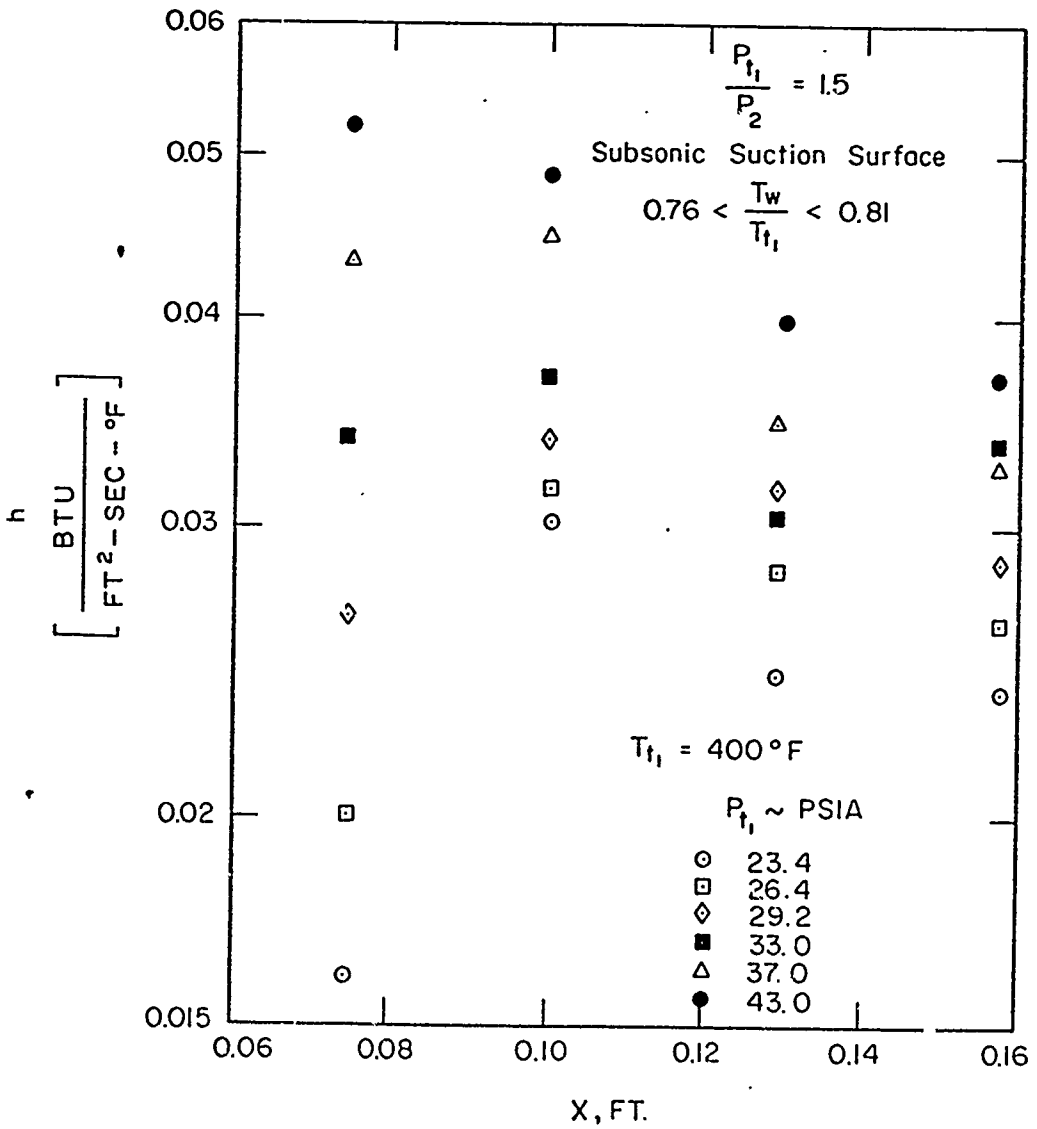

Fig. 35 - Typical suction surface no-blowing heat transfer distributions for $P_{t_1}/P_2 = 1.5$

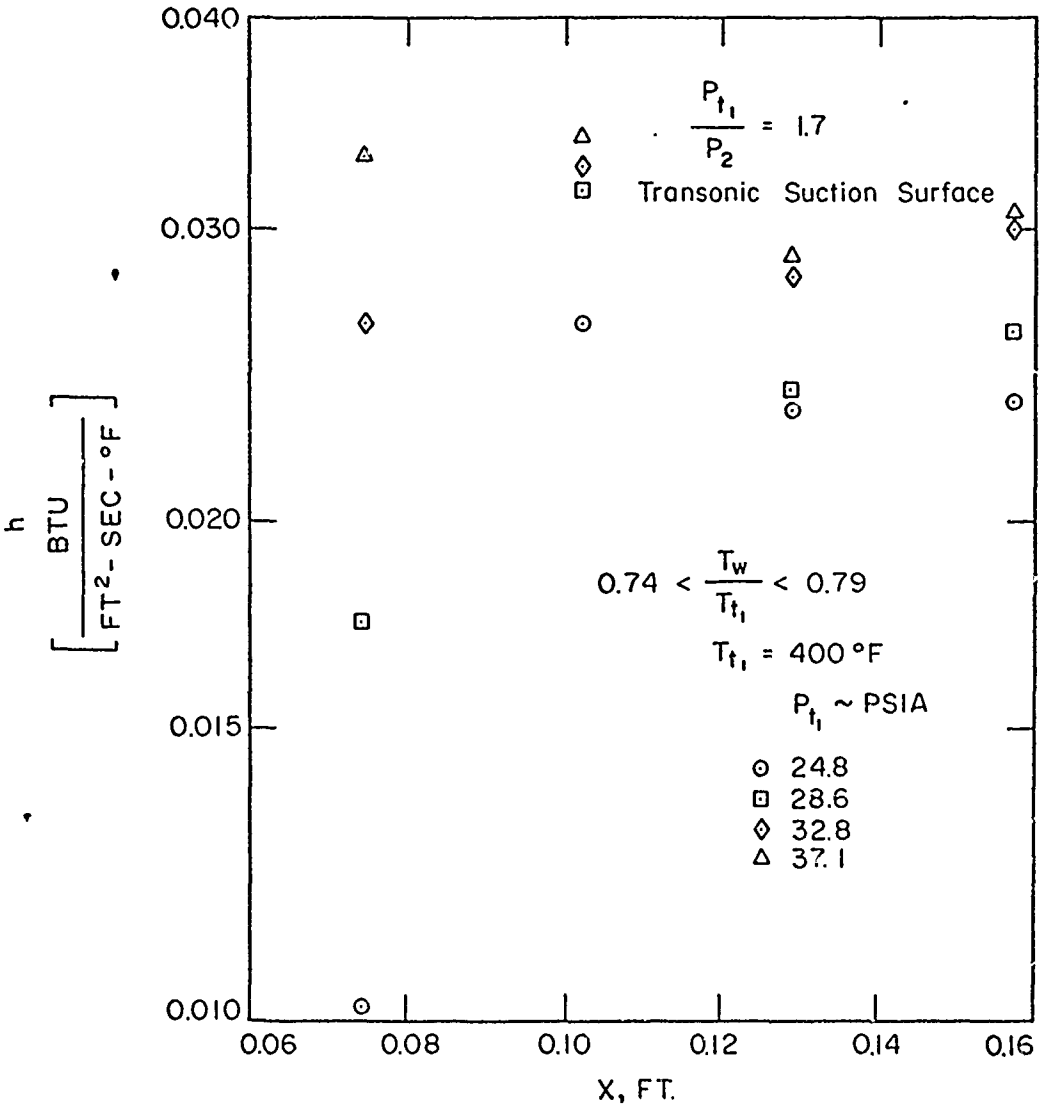

Fig. 36 - Typical suction surface no-blowing heat transfer distributions for $P_{t_1}/P_2 = 1.7$

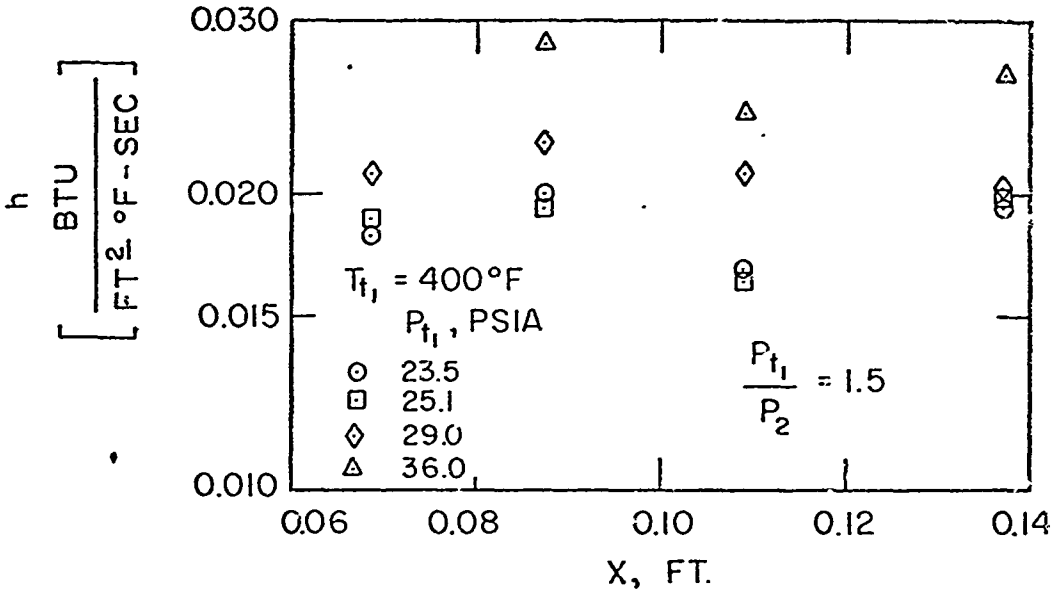

(a) $P_{t_1}/P_2 = 1.5$

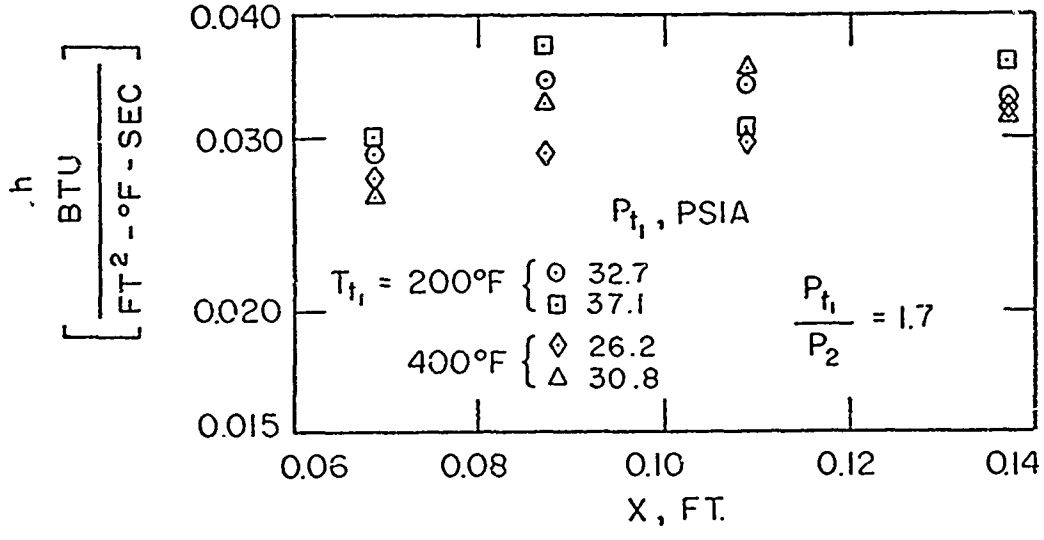

(b) $P_{t_1}/P_2 = 1.7$

Fig. 37 - Typical pressure surface no-blowing heat transfer distribution for (a) $P_{t_1}/P_2 = 1.5$ and (b) $P_{t_1}/P_2 = 1.7$

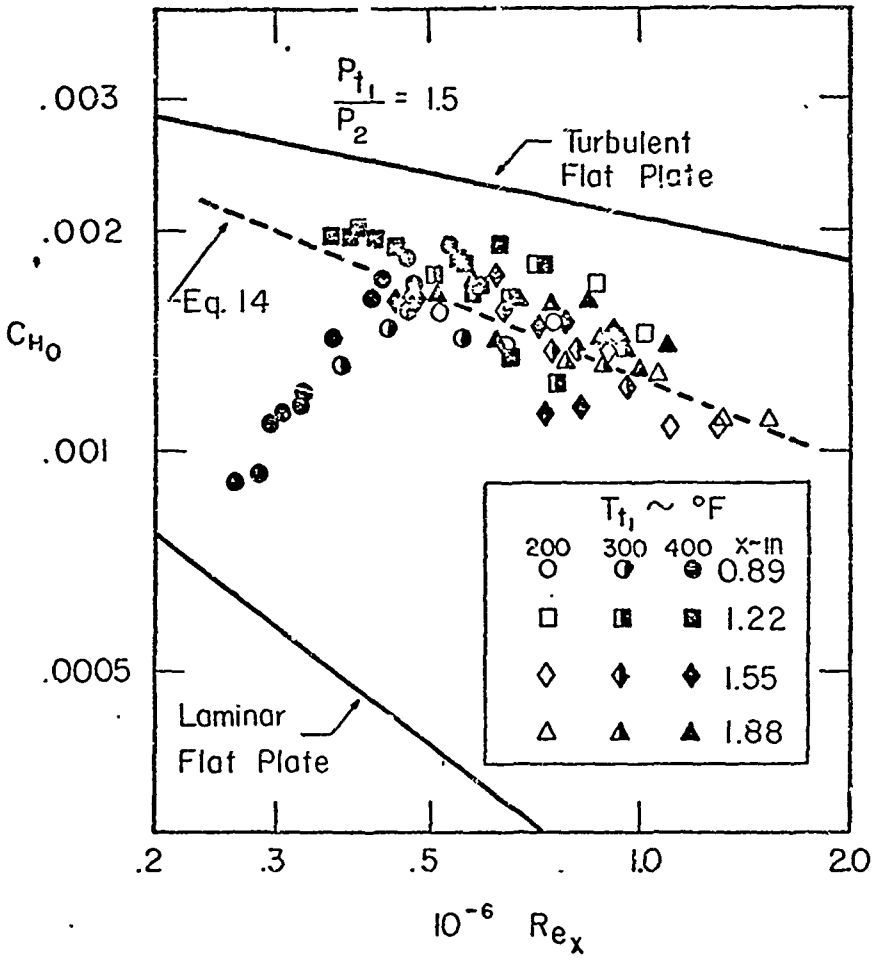

Fig. 38 - No-blowing Stanton number data for subsonic suction surface

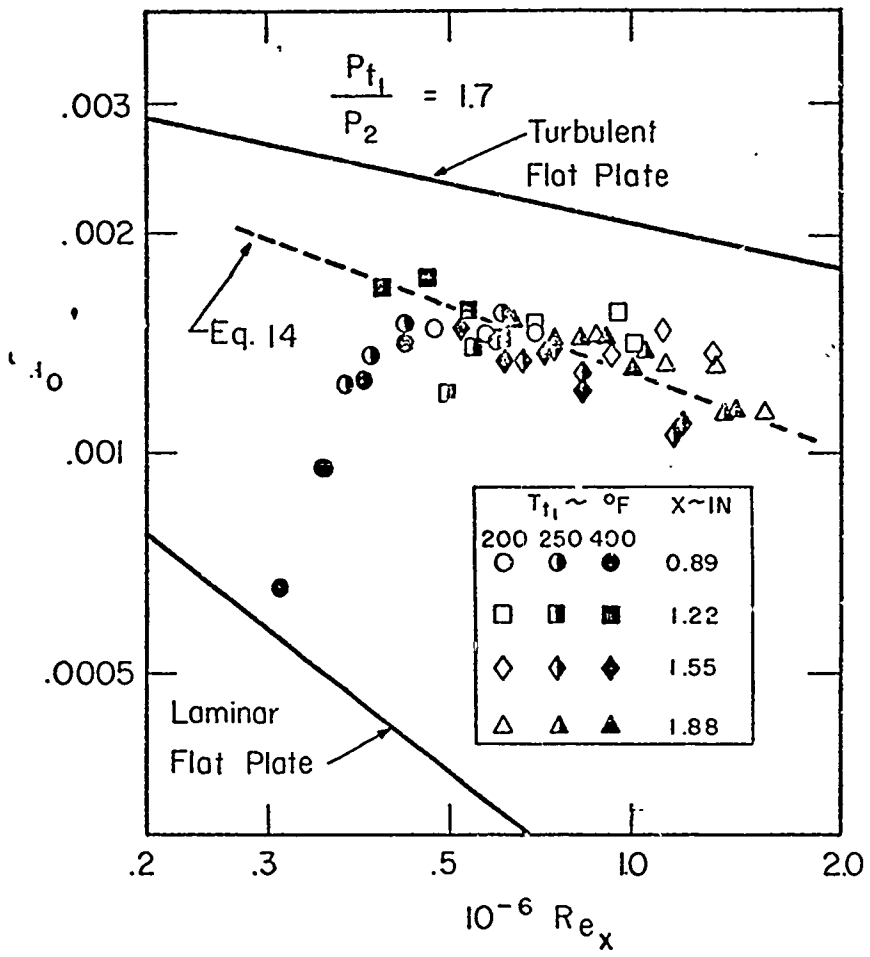

Fig. 39 - No-blowing Stanton number data for transonic suction surface

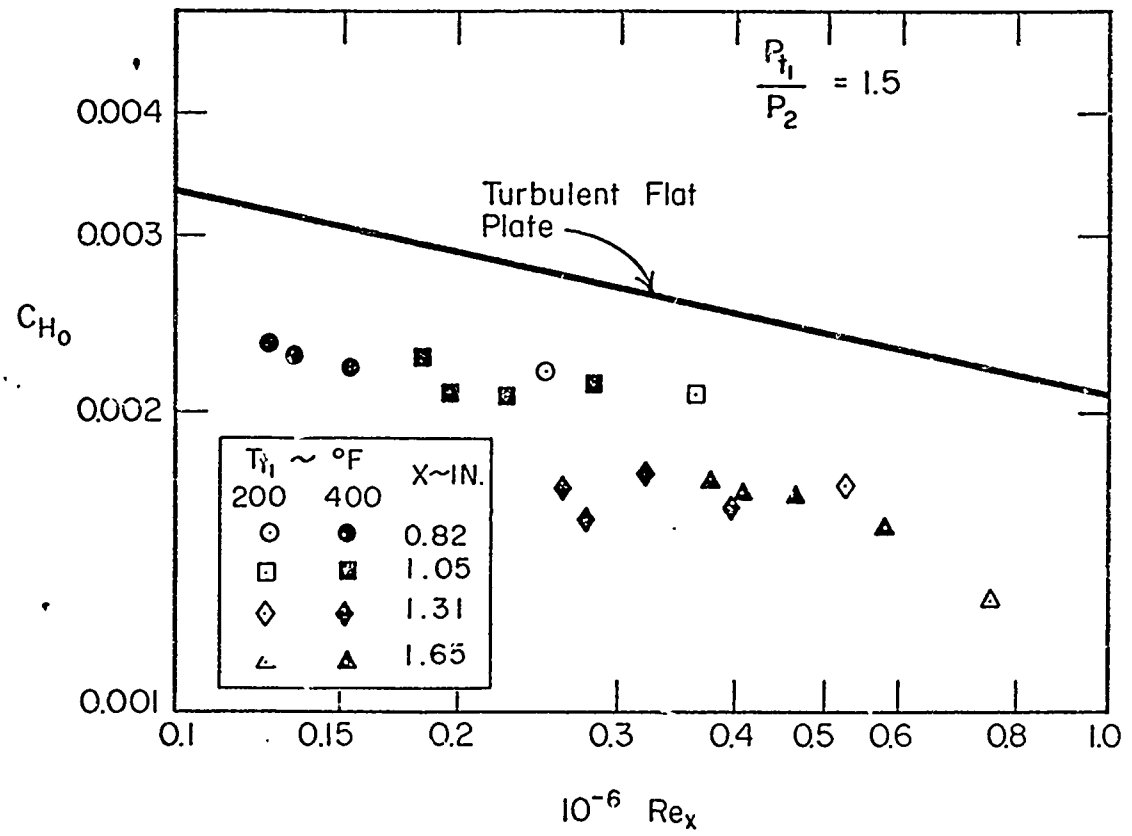

Fig. 40 - No-blowing Stanton number data for pressure surface at $P_{t_1}/P_2 = 1.5$

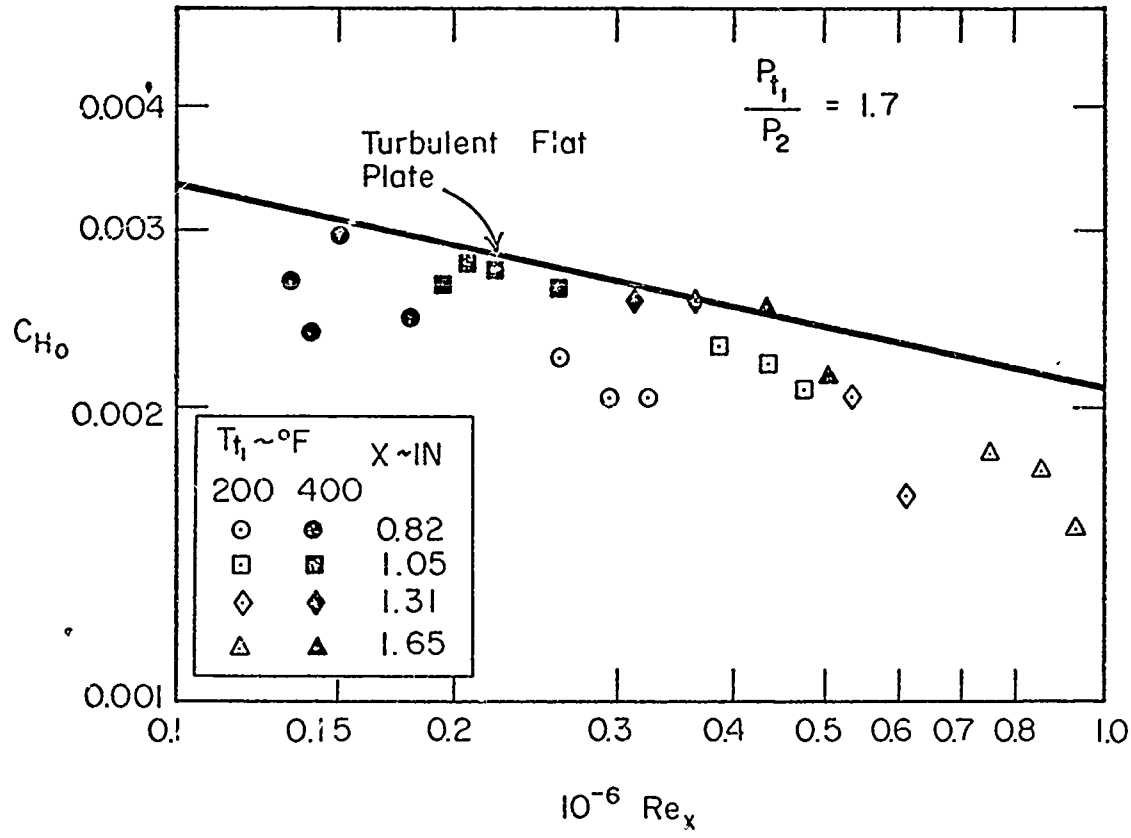

Fig. 41 - No-blowing Stanton number data for pressure surface at $P_{t_1}/P_2 = 1.7$

V. DISCUSSION OF RESULTS

A. NO-BLOWING RESULTS

Any analysis of the effects of film cooling on the flow over a surface must begin with a basic understanding of the flow existing in the absence of blowing. The static pressure distributions measured for B = 0 show that either a negative or very mild positive pressure gradient existed over most of the injection region of the suction surfaces of Models II, III, and IV. These three models gave almost identical no-blowing pressure distributions, as seen in Figs. 23 - 30. The no-blowing static pressure distributions over the suction surface of Model I, however, displayed an inflection and were also slightly higher in value than those measured on the other models. This deviation was investigated and additional tests run, as previously mentioned, but no local surface contour irregularity of sufficient size to cause such behavior could be found. A possible explanation of the phenomenon is the fact that the 12° spanwise blowing geometry used on this model results in large elliptical cavities (0.028 x 0.135 inch) on the surface where the coolant hole and model surface intersect.

The no-blowing heat transfer results of Figs. 38 and 39 show that transition from a laminar to a turbulent boundary layer begins at a local surface Reynolds number of from 250,000 to 300,000 on the suction surface. The location of the beginning of a completely turbulent layer is not apparent from these figures, since only the leading thermocouple, located at x = 0.89 inch, gave heat transfer rates typical of heating in the transition regime. This fact is most clearly shown in Fig. 38 and, to a lesser extent, in Fig. 39, by the two differing trends in the low Reynolds data for the thermocouples located at x = 0.89 inch (circle symbols) and x = 1.22 inch (square symbols). Completion of transition to a wholly turbulent boundary layer thus took place somewhere between the first and second thermocouples; i.e., in the region $0.89 \leq x \leq 1.22$ inches. For the film-cooled models, this is the region containing the first two rows of coolant holes, and therefore additional impetus for transition was provided in this region for the film-cooling models by blowing and/or the equivalent surface roughness of the holes. The Schlieren investigation of Shaw[20] confirms that transition occurred in this region, both with and without blowing, for Models I and II.

Also shown in Figs. 38 and 39 is the empirical correlating equation

$$C_H = 0.162\ Re_x^{-0.35} \tag{14}$$

which was faired through the suction surface Stanton number data and from which C_{H_o} values were obtained for use in the film cooling effectiveness correlations.

The pressure surface heat transfer measurements indicate that a fully developed turbulent boundary layer existed over the entire heat transfer measurement region (0.82 inch $\leq x \leq$ 1.65 inch) of the surface for local Reynolds number as low as 130,000. The boundary layer stabilizing effect of the severe negative pressure gradient over the fore part of the suction surface is apparent when Stanton number data for the two surfaces are compared at equal surface Reynolds numbers. The transition surface Reynolds number for the suction surface is at least twice that of the pressure surface, but no closer determination can be made since all heating measured on the pressure surface indicates a turbulent boundary layer and no evidence of transition was found.

The heat transfer measurements show that the simple approximation of flat plate flow is valid for conservative engineering design estimates of the surface heat transfer to a typical turbine airfoil in the absence of cooling since measured heating rates fell at least 20% to 40% below the flat plate turbulent heating prediction over most of the airfoil surface measured.

B. EFFECT OF BLOWING ON THE STATIC PRESSURE DISTRIBUTION

The effect of blowing on the static pressure distribution, as shown in Figs. 18 - 29, was found to be highly dependent on which surface (S or P) was film cooled. No significant changes in either the magnitude or shape of the lift distribution from the no-blowing case can be seen in the P blowing results for Model I, shown in Fig. 19. Although not shown graphically, this same lack of any P blowing effect on pressure distribution was found to be true for all film cooled models, geometries, and blowing rates. Any alterations that were observed were generally within the ± 1% accuracy of the static pressure measurements and cannot be considered significant. This lack of any effect of P blowing on lift may be attributed to the monotonically negative pressure gradient over the blown region of the pressure surface, a gradient which became increasingly favorable as the trailing edge was approached.

The effect of suction surface (S) blowing, however, was found to be quite significant, as shown in these same figures, causing a loss of lift on the suction surface but, as might be expected, again no noticeable effect on the pressure surface. The distributions obtained for S + P blowing were virtually identical to those of S blowing for all film-cooled models. This is seen for Model I by comparing Figs. 18 and 20. For purposes of analysis, only the effects of S blowing on the suction surface pressure distribution need be examined to determine any effects due to the various blowing geometries.

A comparison of the S blowing suction surface distributions shows that the 90° blowing on Model II caused the most severe loss of lift of all geometries tested. This can be seen by comparing Figs. 18, 22,

24, and 26 for the subsonic suction surface ($Pt_1/P_2 = 1.5$) and Figs. 23, 25, and 28 for the transonic suction surface ($Pt_1/P_2 = 1.7$). Severe loss of lift was also found for the spanwise blowing geometries of Models I (12° spanwise) and III (30° spanwise). The effects appear to have been quite similar for both the subsonic and transonic cases, although Model I was not tested for the transonic condition. A general similarity can be noted between the surface pressure alterations for Models I, II, and III, all of which injected coolant having no chordwise velocity component. The loss of suction surface lift began well ahead of the first blowing row (x = 0.93 inch) for all geometries tested, as shown most clearly by the data points at x = 0.75 inch in Fig 22. This effect was most pronounced for the 90° injection geometry and least noticeable on Model IV, which emitted coolant in the chordwise direction 30° from the surface tangent.

The effect of blowing rate intensity on the lift alterations was found to be similar for the non-chordwise injection geometries of Models I, II and III at small values of B. Comparison of the pressure distributions of Figs. 22 and 24 for the lowest non-zero value of B shows that for these low blowing rates there was a negligible difference between the lift alterations caused by 90° or 30° spanwise injection. The same result is observed for the transonic surface when Figs. 23 and 25 are compared. However, as B was increased, the vertical blowing effect on loss of lift became increasingly more severe than that of the spanwise blowing. This is in spite of the fact that the vertical blowing component was the same for the two cases. Figure 22 shows that at a value of B = 7, the alteration of the static pressure distribution for vertical blowing resulted in a negative pressure gradient over the entire suction surface.

Examination of the data from the last pressure tap on the suction surface for all models tested shows that as the blowing rate was increased, the pressure at this location (x = 2.09 inches) approached a common value for all models, the value being very close to the downstream static pressure, i.e., P_2/P_{t_1}. This suggests that the flow may have separated near the trailing edge, with the terminal or base pressure being felt further upstream as the separation region crept forward with increasing blowing. Such a hypothesis cannot be proven by the present pressure data since the region in question possessed a small pressure gradient such that numerous pressure taps would have been required to see this effect. However, it should be mentioned that the Schlieren investigation of Shaw[20] for Models I and II shows some evidence that separation did occur in the immediate vicinity of the trailing edge for both models at low coolant flow rates. The same investigation also suggests that the separation appeared to move forward for Model II (90° injection) as blowing was increased, but the boundary layer appeared to be attached over the coolant injection region ($0.92 \leq x \leq 1.91$ inches) for values of B as high as 7.

Although film-cooled turbine airfoil pressure data for comparison with the present results are not available in the open literature, the recent experimental results of Provenzale and Thirumalaisamy[15] show that for the transpiration cooled stator blades of their study the static pressure distribution was completely unaffected by mass addition from both surfaces at coolant flow rates equivalent to those of the present study. This is in marked contrast to the present surface pressure measurements which show the generally disruptive nature of film cooling by discrete hole blowing.

C. EFFECT OF BLOWING ON THE TOTAL PRESSURE LOSS COEFFICIENT

The measurement of the total pressure loss coefficient presents a conclusive contrast between the blowing geometries which injected coolant with no chordwise velocity component and the streamwise-oriented injection of the suction surface of Model IV. This is shown in Figs. 30 and 31 in which the shift of the peak wake momentum defect toward the suction surface is evident for Models I, II, and III. The total pressure loss coefficients calculated from the wake pressure surveys are shown in Figs. 42, 43, and 44 in the form of $\omega - \omega_o$, where ω_o is the coefficient calculated using the integrated total pressure defect for the airfoil without blowing. Several similarities between these three figures are significant.

First, it is noted that all blowing geometries gave approximately the same losses at low values of the blowing parameter $B < 3$. As blowing was increased, three differing trends were observed. The losses for the vertical blowing of Model II continued to rise in an almost linear fashion, as did those of the 12° spanwise geometry of Model I. The losses for the 30° spanwise geometry of Model III also rose as B was increased, but at a decreasing rate, so that at the massive blowing rates of $B > 9$, the 30° spanwise geometry began to show a significant reduction in losses from those shown by Models I and II. This appeared surprising, since Model III is of intermediate geometry, having a spanwise injection angle $\theta = 30°$ and a number of holes per row of 17, both values which fall between those of Models I and II.

This similarity of the observed losses for the spanwise injection geometries of Models I and II and the lower losses measured for Model III prompted an examination of the actual exit angles for the coolant air. Using smoke tests, it was observed that the 12° injection geometry, unlike the others, emits the coolant at the hole angle only for very low coolant velocities. As coolant velocity was increased, the low length-to-diameter ratio allows the coolant to increase its exit angle until, at the extreme case of the choked condition, the average angle is greater than 45°. The ideal coolant velocities for this geometry are also higher, as was seen in Fig. 17, but these would be reduced as the flow occupied more of the surface ellipse with increasing mass flow rate.

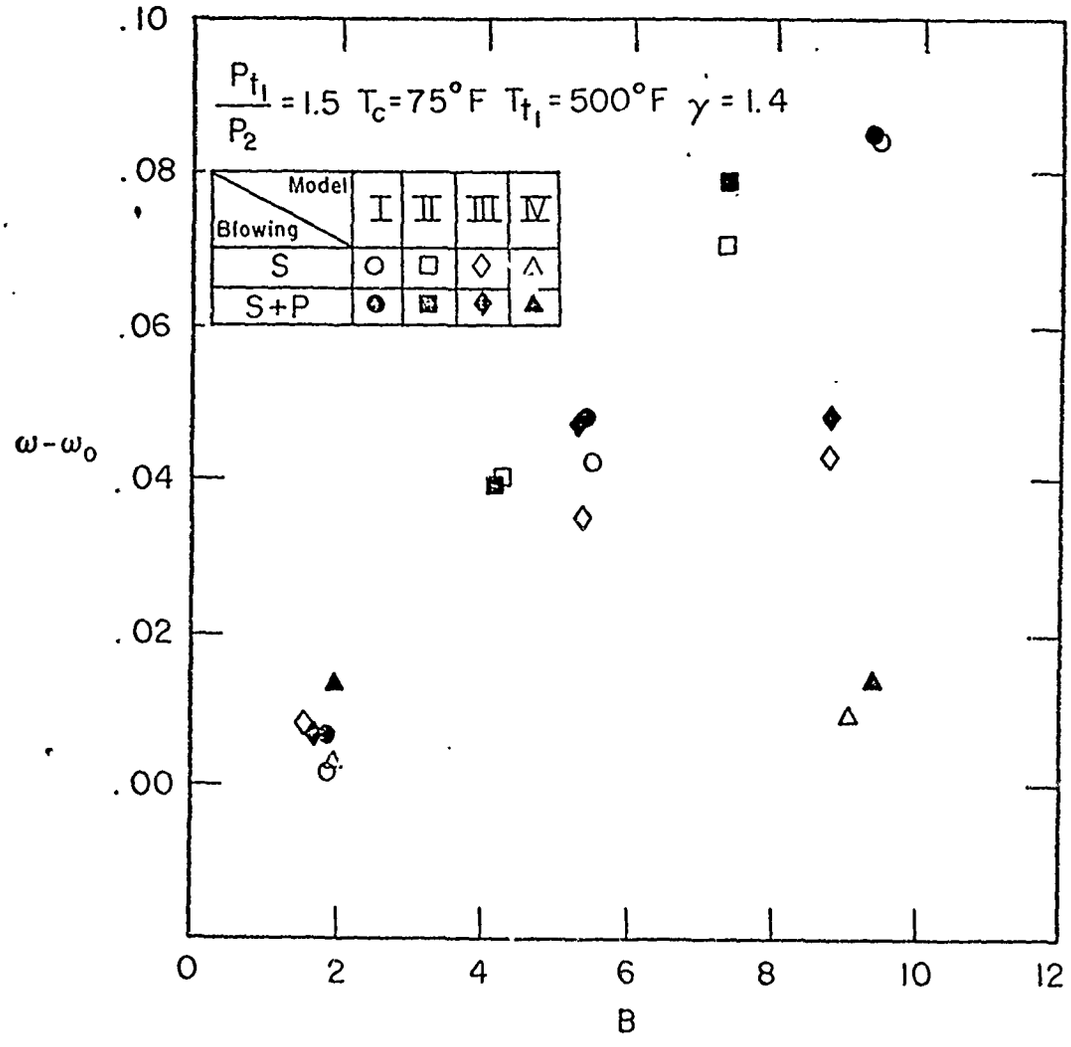

Fig. 42 - Increase in total pressure loss coefficient ω for Models I-IV at T_{t_1} = 500°F and P_{t_1}/P_2 = 1.5

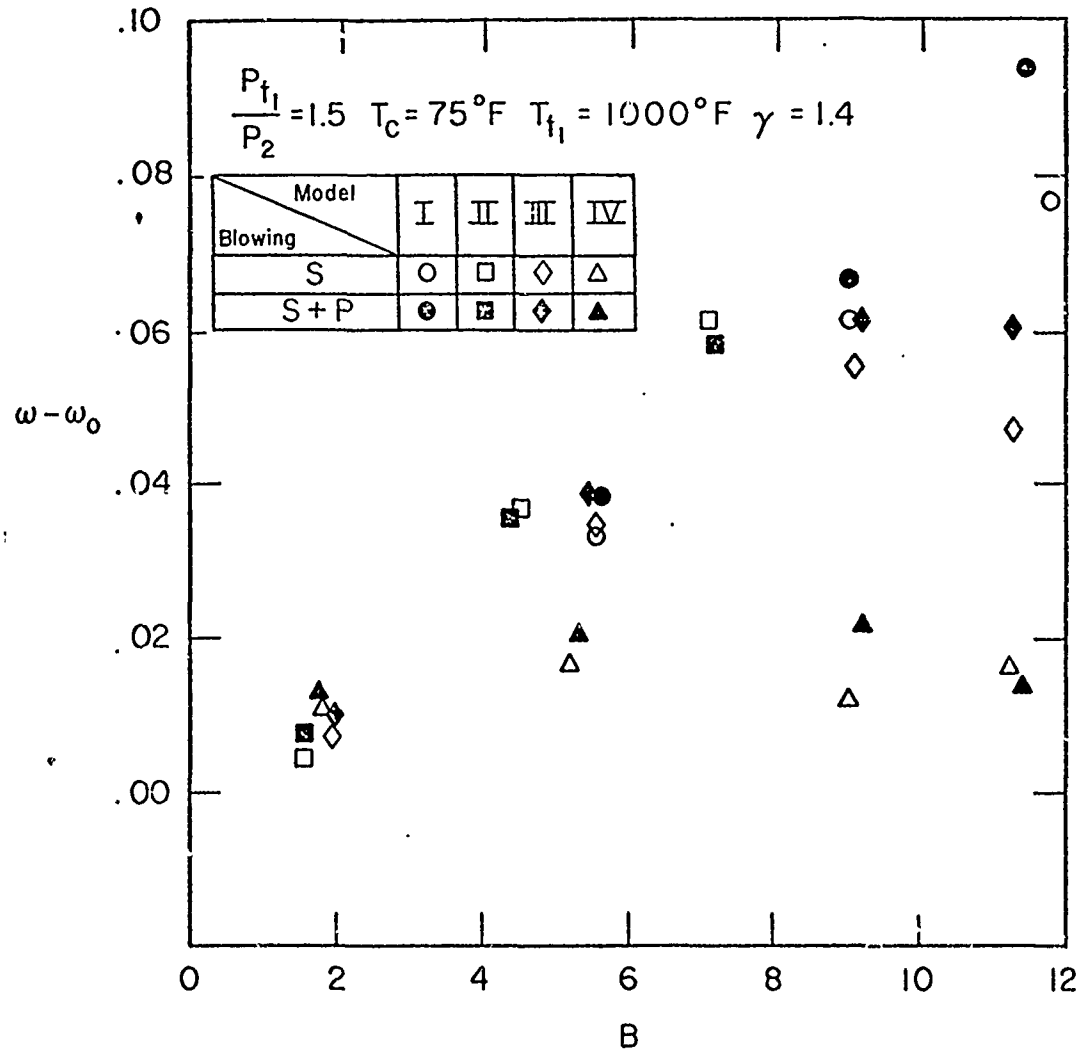

Fig. 43 - Increase in total pressure loss coefficient ω for Models I-IV at T_{t_1} = 1000°F and P_{t_1}/P_2 = 1.5

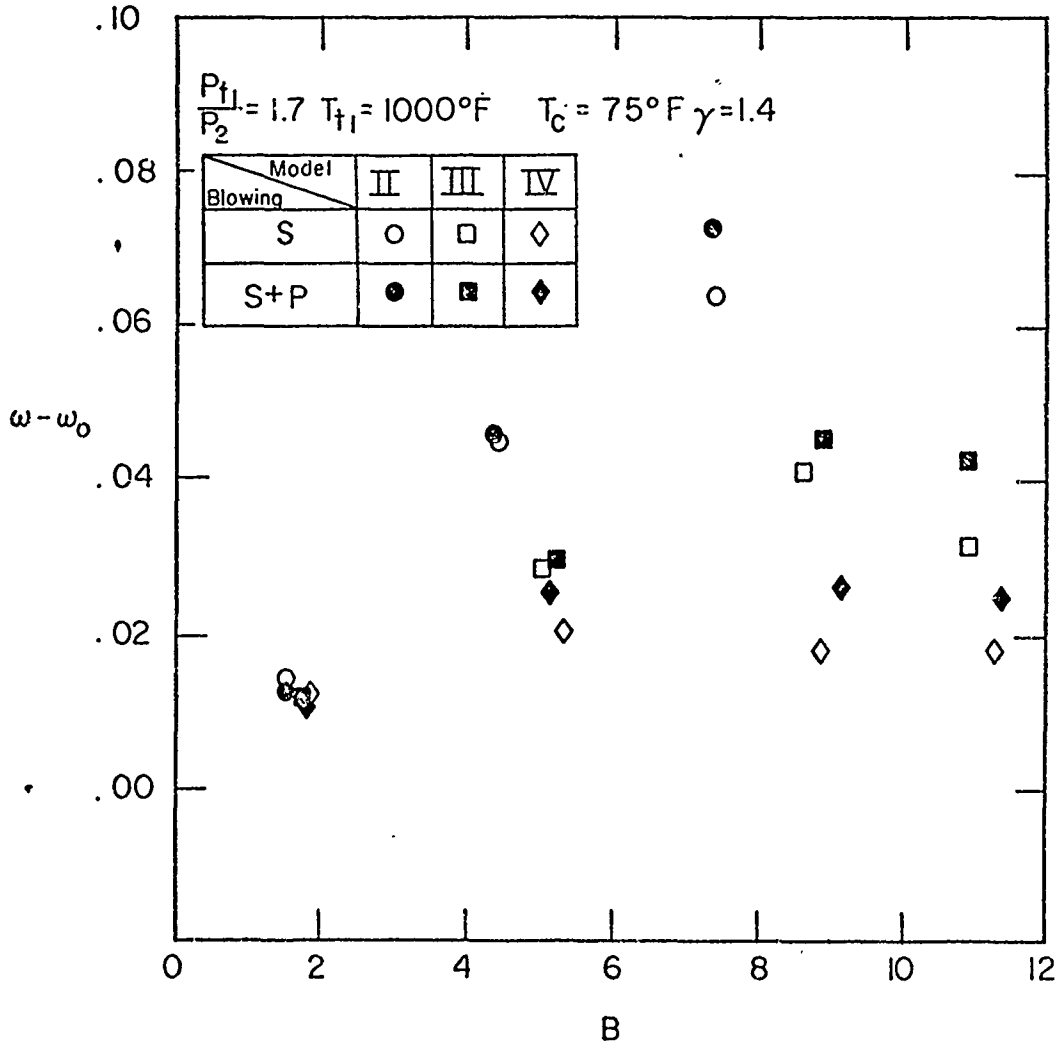

Fig. 44 - Increase in total pressure loss coefficient ω for Models II, III, and IV at P_{t_1}/P_2 = 1.7

This problem does not arise with the other geometries since the coolant holes have sufficient guiding length to keep the coolant flow vector coaxial with the hole until the surface is reached, where bending and mixing with the boundary layer and external flow begins.

The results for ω, however, do indicate a marked decrease in the total pressure losses for the 30° spanwise blowing geometry when compared with the 12° and 90° injection. This fact, when considered in the light of the above discussion concerning the 12° geometry, indicates that spanwise inclinations may be helpful in reducing losses, although not nearly to the degree that chordwise angling, such as the surface geometry of Model IV, accomplishes.

The reduction of losses for Model IV was evident at each of the test conditions except for the lowest blowing rates tested. At the higher values of B, this model gave losses which were less than 1/4 those of the vertical and 12° spanwise geometries.

A second result of a comparison of Figs. 42 - 44 is the consistent agreement of S and S + P losses. This indicates, as do the static pressure distributions, that the suction surface was the primary source of all losses measured. The fact that the losses appear to be, for each geometry, a function of B (which is a surface-to-stream parameter) also confirms this.

The superiority of the chordwise coolant injection in reducing losses at higher blowing rates is predictable, since considerable coolant momentum is wasted by non-streamwise blowing. This momentum waste, which for non-chordwise injection is $\rho_c u_c^2$, must be absorbed as a deficit by the external flow (including the boundary layer), while chordwise coolant injection contributes to the flow momentum the component $\rho_c u_c^2 \cos \varphi$ ($\varphi = 30°$ for Model IV, S blowing). This latter quantity increases with increasing B, thus a reduction of losses for chordwise injection is not surprising.

It is instructive to examine the effect of the angular orientation of injection by assuming a simple physical model for the flow about the airfoil and determining whether the basic conservation equations of fluid dynamics predict loss coefficient variations such as those mentioned. Such an analysis has been performed (see Appendix A) in which the flow past the injection surface of the confined airfoil in this study has been approximated by a constant area channel. Isentropic compression from the inlet (Station 1) to the channel entrance was assumed, as was isentropic expansion from the channel exit to the downstream wake survey location (Station 2). All mixing of coolant and primary flow was assumed to occur in the constant area channel with the primary flow at an average Mach number, found by using the average of S and P surface pressures over the blowing region. The results of this calculation are shown in Fig. 45, where ξ is used as the blowing parameter. The trends shown agree with the experimental results previously

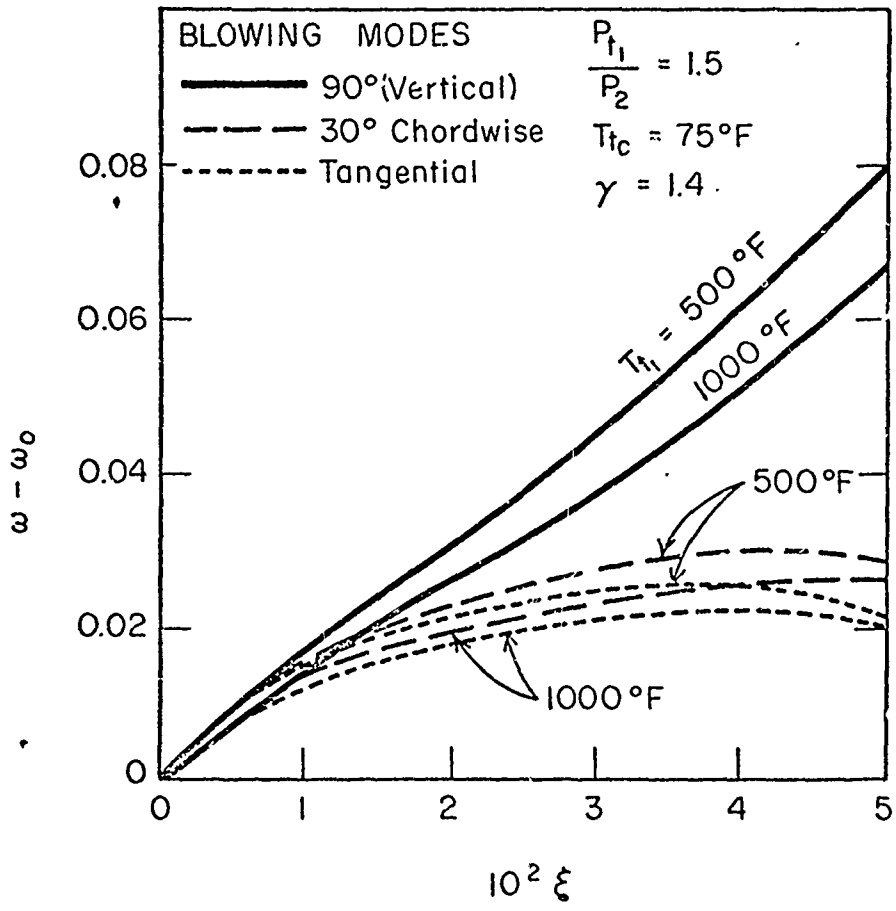

Fig. 45 - Increase in total pressure loss coefficient ω predicted by ideal mixing analysis (Appendix A)

shown, and the advantage of chordwise angled blowing is obvious. Tangential injection curves ($\varphi = 0°$) show only a slight superiority to the 30° result. The spanwise $\theta = 30°$ geometry is considered a vertical ($\varphi = 90°$) geometry as far as the ideal mixing analysis is concerned.

The present experimental results for $P_{t_1}/P_2 = 1.5$ are compared with the ideal mixing calculations in Figs. 46 and 47. Agreement is clear for S + P blowing, the condition which more nearly satisfies the assumption of the calculations that the Mach number is averaged over the blowing region of both surfaces. The fact that the present experimental results show a general agreement with the ideal mixing analysis indicates that the experimentally observed losses are explainable, in large part, by momentum loss caused by coolant and primary flow mixing and that castastrophic effects, such as boundary layer separation, are not the dominant mechanism.

The simplified analysis of ideal mixing, which predicts that nonchordwise injection results in a nearly linear ω vs. ξ relationship, is equally applicable (as far as the assumptions are concerned) to transpiration cooling. This is confirmed by Reference 15, in which transpiration-cooled stator blades were tested in an annular cascade. The data of Reference 15 show a simple linear relationship between ω and ξ for ξ values as high as 0.08, thus the simple mixing analysis appears to be quite useful for engineering calculations and estimates. An interesting facet of the above transpiration-cooled blade results is the fact that the airfoil tested emitted coolant over the entire surface. Thus the concept of an average Mach number in the region of injection was a considerable approximation.

D. FILM COOLING EFFECTIVENESS RESULTS

The data obtained from the thermocouples located below the suction surface are shown in Figs. 48 - 51 in the form of the effectiveness η and a correlating parameter C_{H_o}/Ms, which is the standard film-cooling parameter with the x-dependence removed. The S blowing results were influenced considerably by heat conduction through the blade from the uncooled pressure surface, and thus they undoubtedly underestimate the actual film-cooling effectiveness on the suction surface. The S + P blowing results were not affected by this problem since no large temperature gradient existed across the blade thickness, but these data were affected somewhat by internal cooling due to coolant passage within the airfoil. Thus, the S + P results are judged to be the upper limit on film-cooling effectiveness since they are at least as high as the adiabatic η normally used to examine film cooling. The S + P data are also of more engineering significance since actual turbine airfoils are constructed in a basically solid manner such as the present models and therefore the adiabatic wall condition is rarely met in practice because of the internal convective cooling caused by coolant passage through the blade interior.

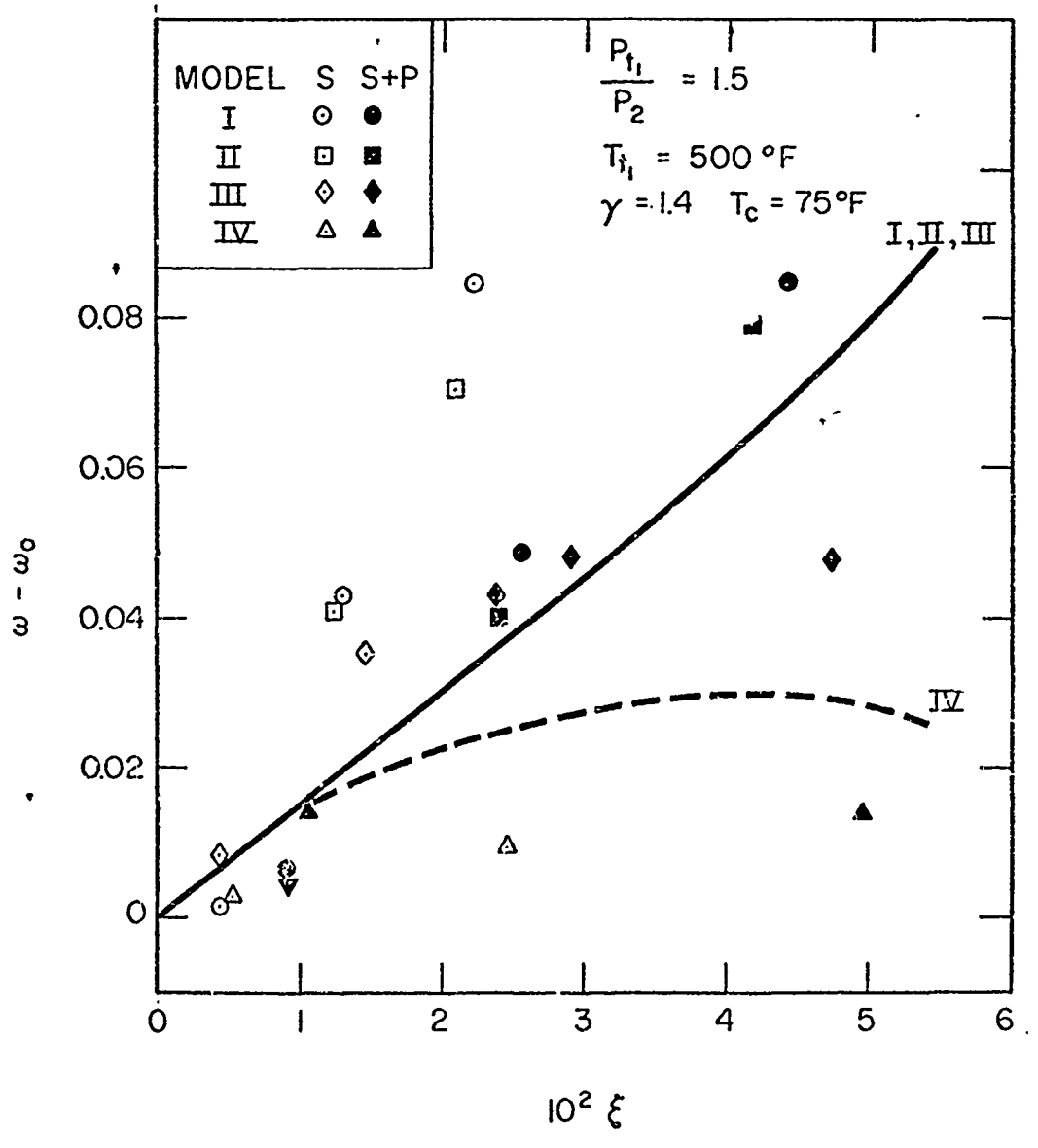

Fig. 46 - Comparison of measured ω values with prediction of ideal mixing analysis for T_{t_1} = 500°F

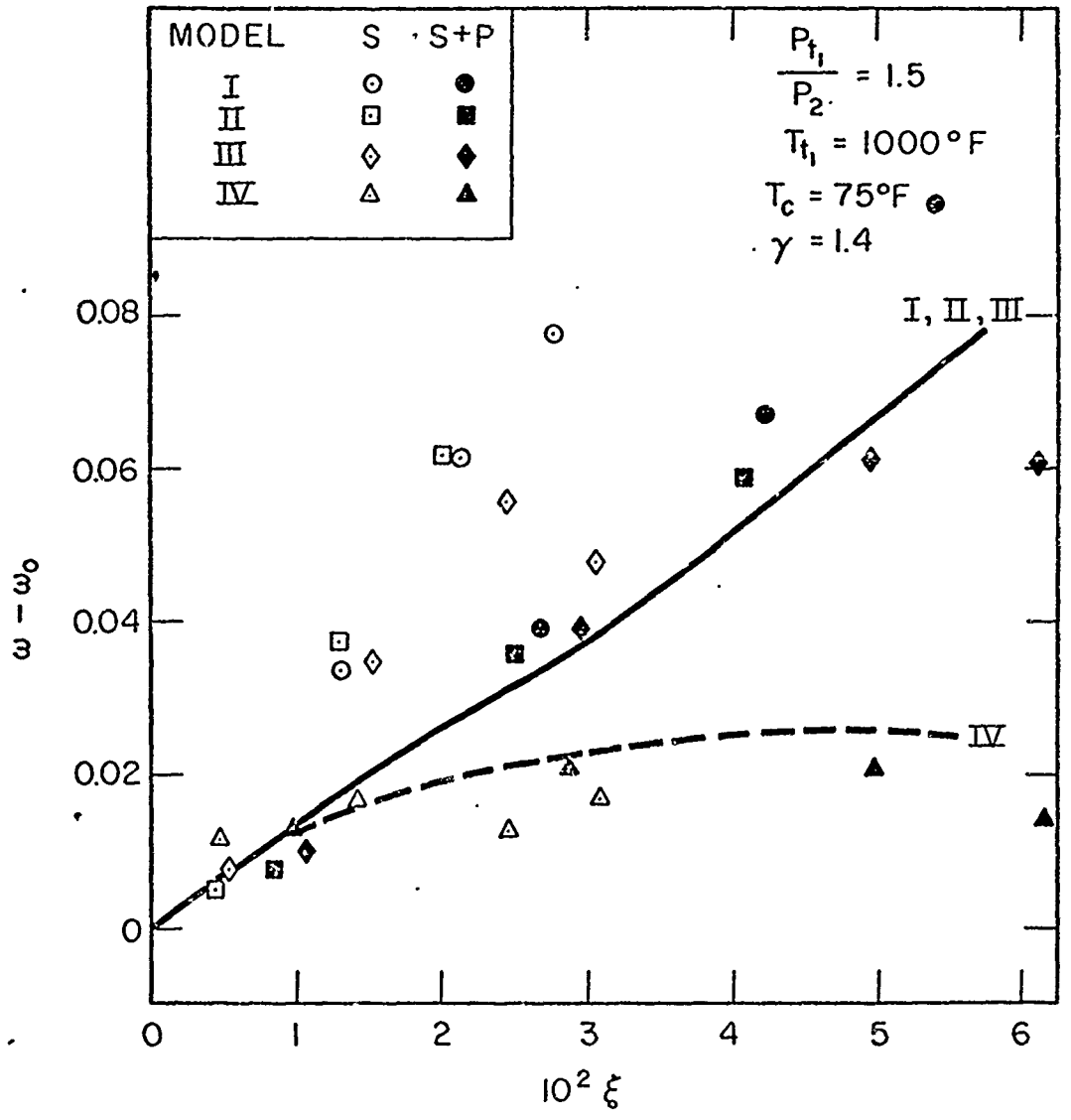

Fig. 47 - Comparison of measured ω values with prediction of ideal mixing analysis for T_{t_1} = 1000°F

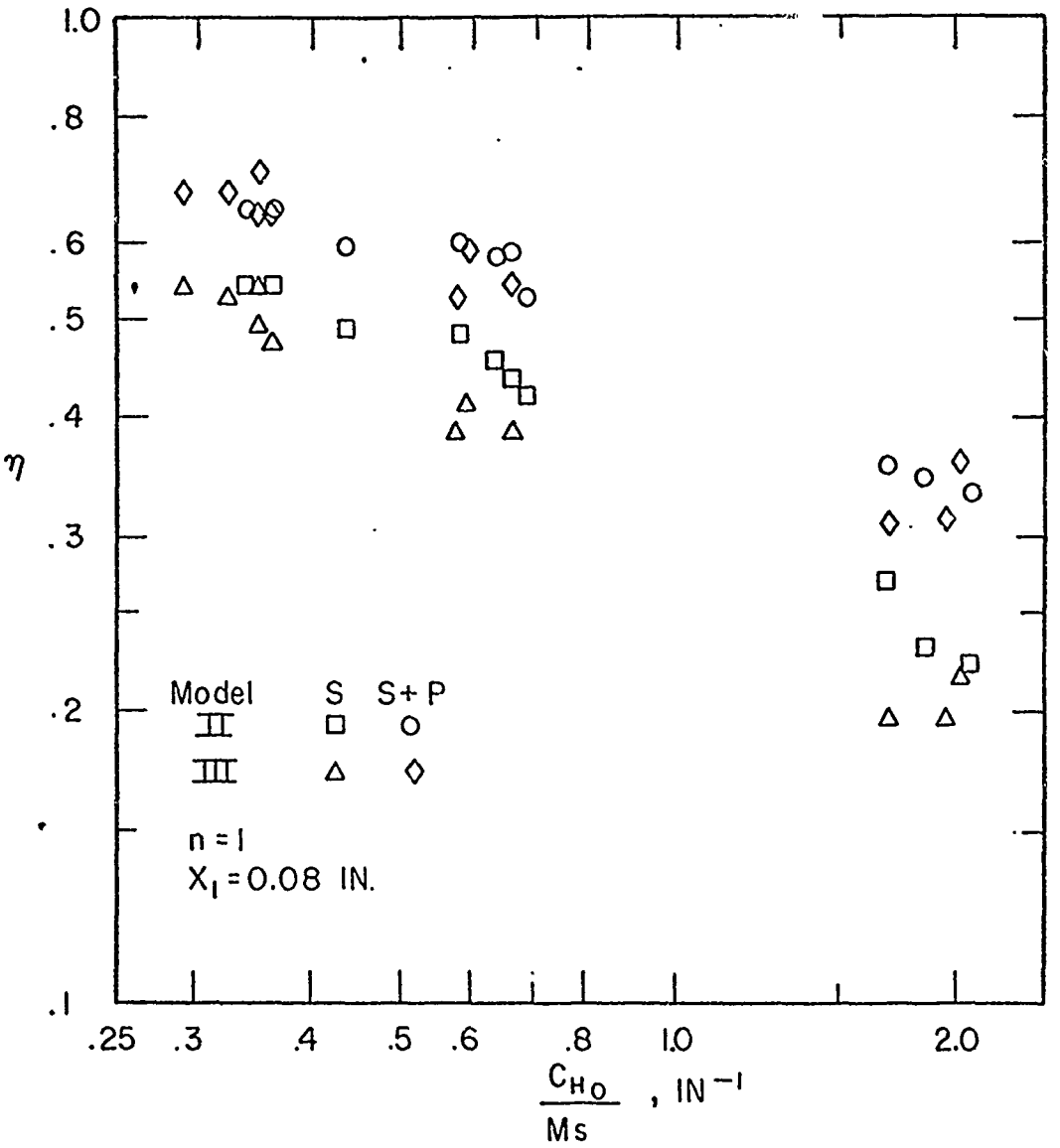

Fig. 48 - Suction surface cooling effectiveness 0.08 inch aft of first blowing row for Model II (90° blowing) and III (30° spanwise blowing)

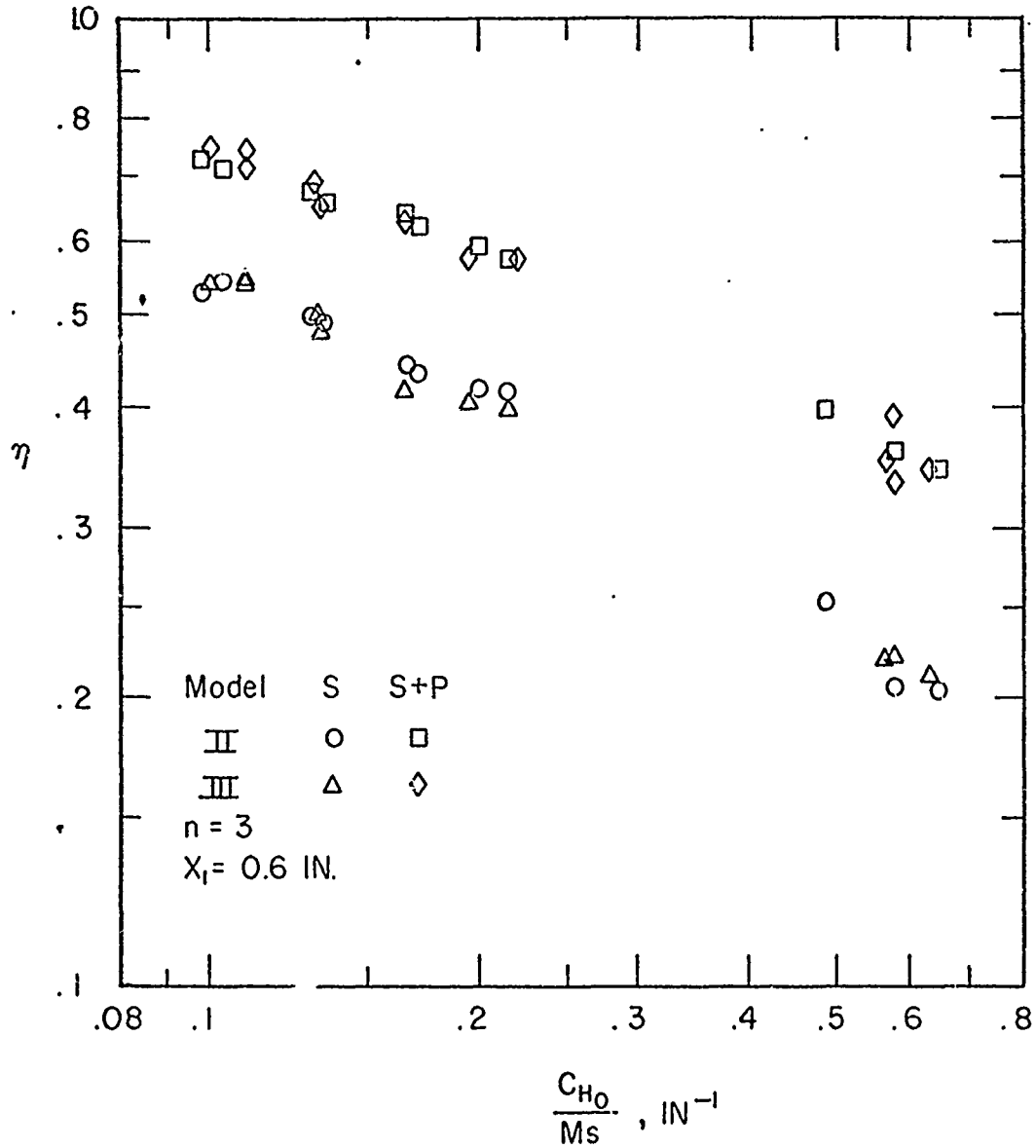

Fig. 49 - Suction surface cooling effectiveness 0.6 inch aft of first blowing row for Models II (90° blowing) and III (30° spanwise blowing)

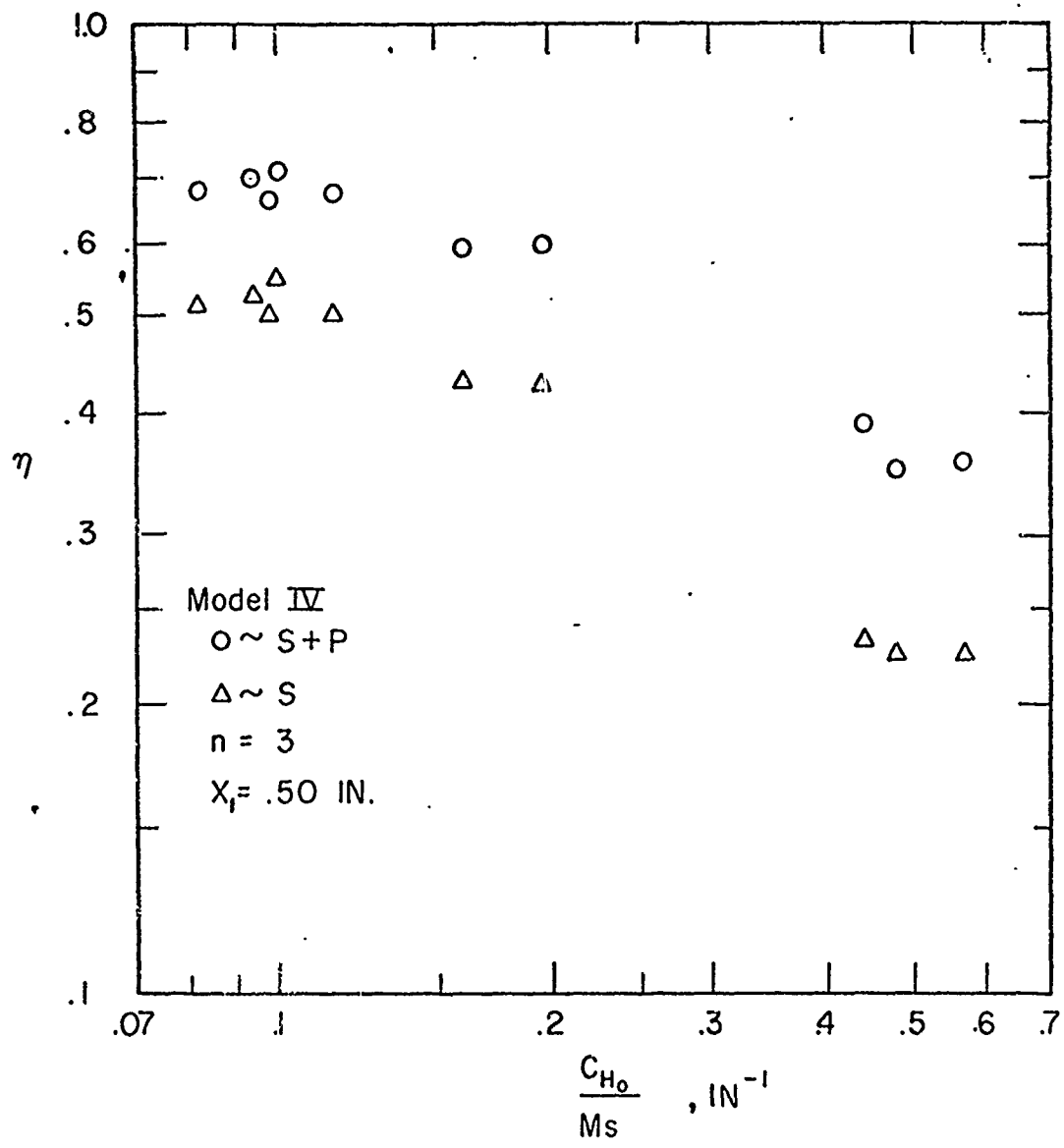

Fig. 50 - Suction surface cooling effectiveness 0.5 inch aft of first blowing row for Model IV (30° chordwise S blowing, 20° spanwise P blowing)

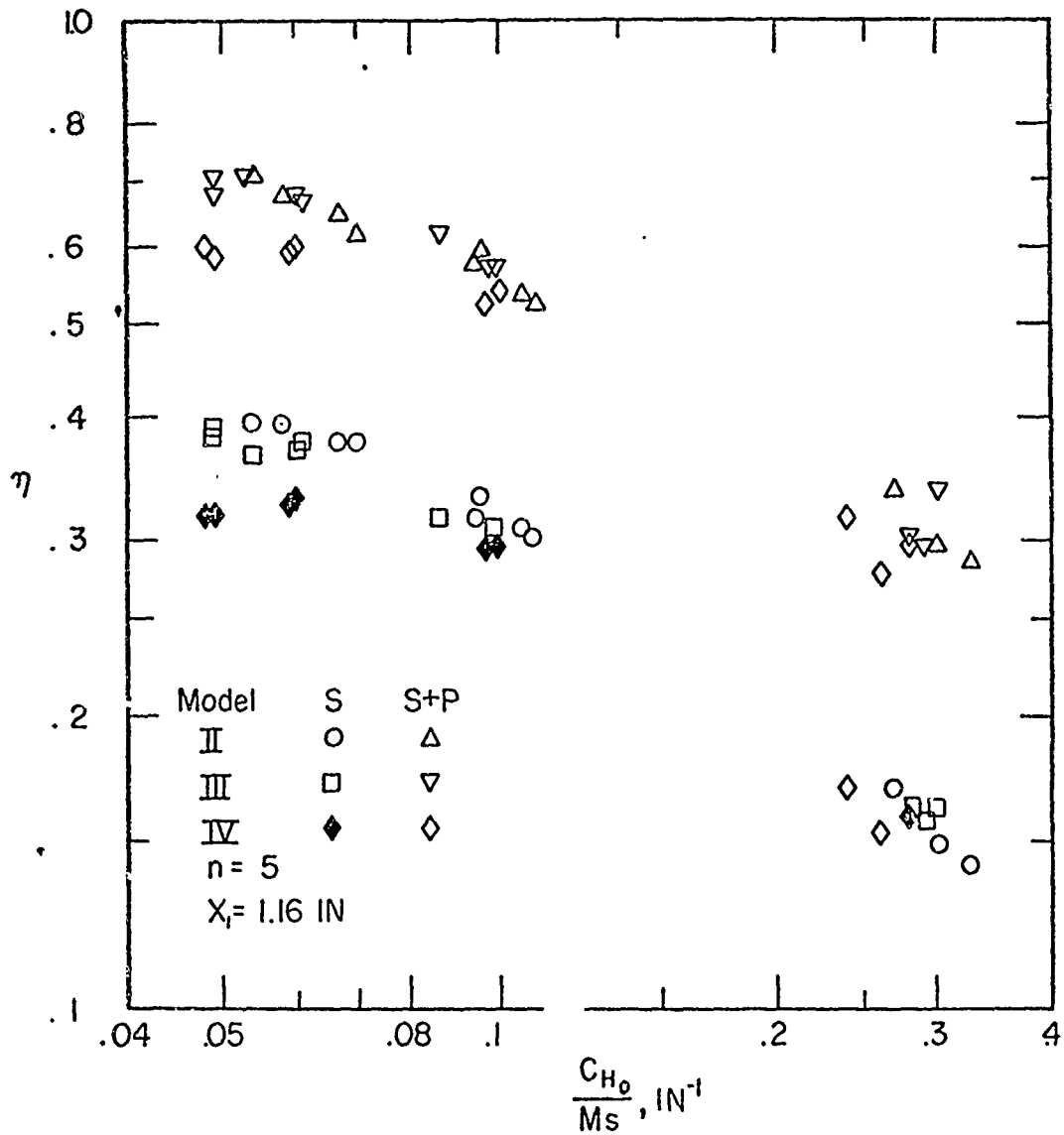

Fig. 51 - Suction surface cooling effectiveness 1.16 inch aft of first blowing row for Models II (90° blowing), III (30° spanwise blowing) and IV (30° chordwise S blowing and 20° spanwise P blowing)

This raises the question of error in η due to the assumption that $T_c = 75°F$, which was used to calculate all η values reported. An analysis of the possible error introduced by this assumption is presented in Appendix B, the results of which show that the maximum error in η due to the assumption of constant coolant temperature is generally less than 0.03 for the present conditions.

Figure 48 compares the measured effectiveness for a point cooled by only one row of coolant holes (n = 1); i.e., based on a thermocouple measurement immediately downstream of the first row of holes. Since the C_{H_o} values used are average values obtained from the no-blowing heat transfer measurements, scatter must be expected in the results in both the η and C_{H_o}/Ms directions. The results show, however, that neither of the blowing geometries enjoyed a clear superiority in cooling effectiveness. The same result is shown by Figs. 49 - 51, which show measured cooling effectivenesses at suction surface locations cooled by 3 and 5 rows of holes (n = 3,5). Figure 51 indicates an apparent decrease in cooling effectiveness for the trailing edge region thermocouple of Model IV, but this cannot be definitely attributed to film effects since the chordwise blowing geometry of Model IV necessitated changes in the location of internal coolant passages which could have caused this effect. Slight internal geometry changes in Model IV from those used in Models I, II, and III also caused the n = 3 thermocouple (Fig. 50) to be located 0.10 inch further forward than the same thermocouple on Models II and III.

Since the effectiveness data were obtained using multiple rows of holes which were approximately equally spaced, the choice of an x value to be used in the standard film cooling correlating parameter C_{H_o} x/Ms is not readily apparent. Several possibilities were investigated, among these the cases where

(1) $x = x_1$, the distance from the point of measurement to the first row of holes;

(2) $x = x_n$, the distance from the point of measurement to the closest upstream hole row; and

(3) $x = \bar{x}$, the arithmetic average of the distances to each of the distances to each of the upstream rows; i.e., $\bar{x} = \frac{1}{n} \sum_{i=1}^{i=n} x_i$. (Each of these choices of x reduces to the correct single row x when only one row is present.)

Curves were faired through the averages of the S + P data shown in Figs. 48 - 51 and plotted as functions of C_{H_o} x/Ms for each of the choices of x mentioned above. This is shown in Fig. 52, where it is clear that the choice of $\bar{x}$ is preferable. The concept of $\bar{x}$ merely

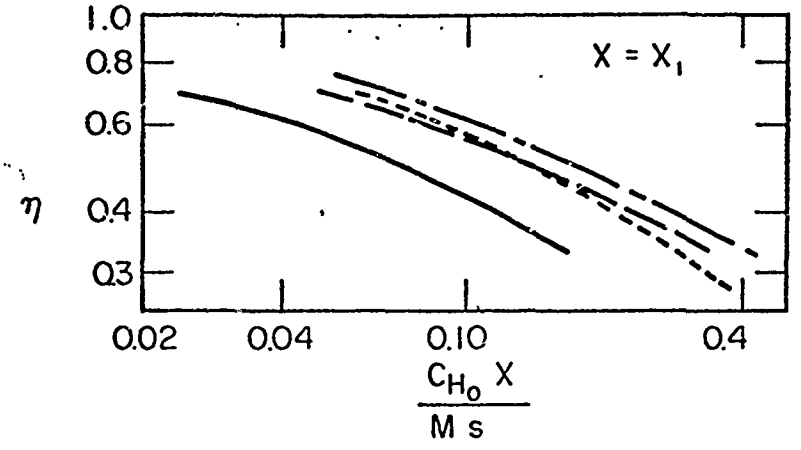

a) $x = x_1$

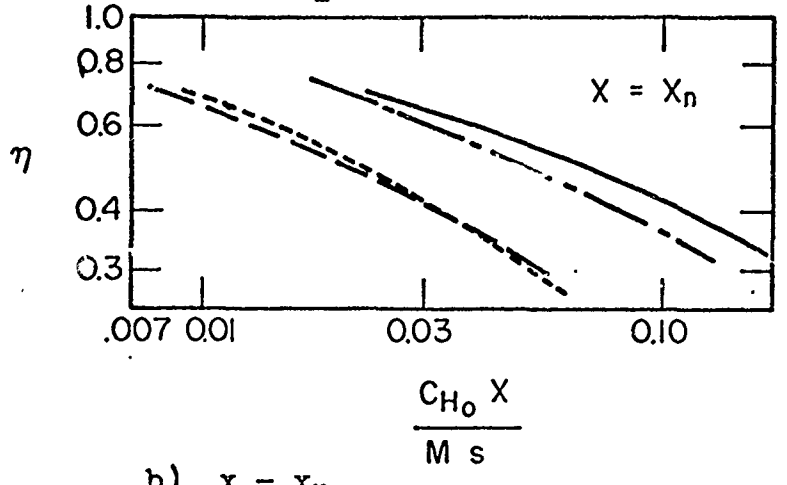

b) $x = x_n$

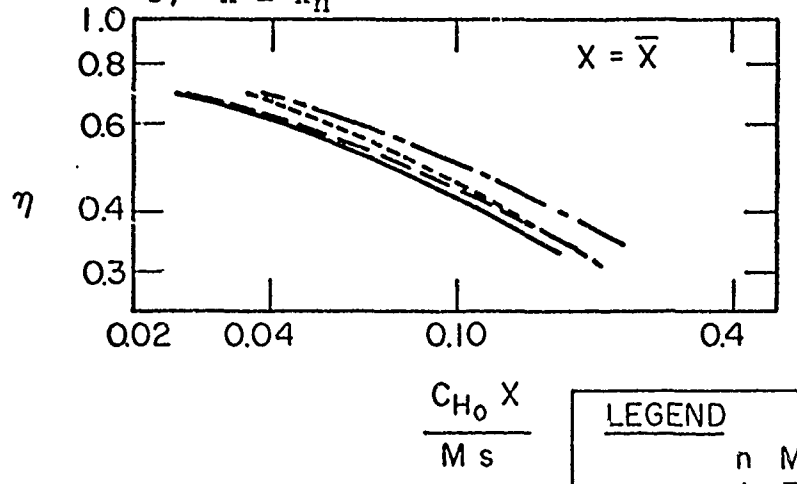

c) $x = \bar{\bar{x}}$

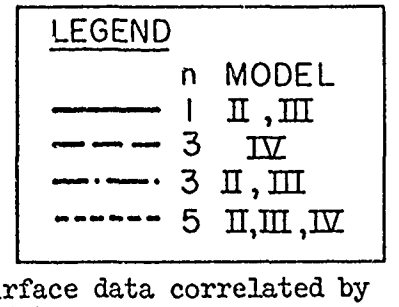

Fig. 52 - Present S + P suction surface data correlated by (a) $x = x_1$, (b) $x = x_n$, (c) $x = \bar{x}$

replaces the multiple rows (or slots) with a single row (or slot) located midway in the row or slot distribution. At large distances downstream from the rows, any of the three choices of x appears appropriate, but for measurement points within the rows, such as the present case, $\bar{x}$ appears to be preferable.

Figures 53 and 54 show the present suction surface effectiveness data compared with the single slot correlation of Haering,[16] using $\bar{x}$ as the characteristic length. Hearing's correlation is typical of the numerous single slot correlations, as is shown in Reference 16. The present S blowing data contain considerable scatter since these data were affected by heat conduction through the model in varying amounts because of the variation of model thickness. Furthermore, as noted earlier they can be expected to represent only a lower bound on the true film-cooling effectiveness. The S + P results, shown in Fig. 54, represent a more true measure of cooling effectiveness as would be encountered in an actual turbine airfoil, although these results probably overestimate the film-cooling effectiveness due to internal cooling effects. The figure shows that they correlate reasonably well using $\bar{x}$. A curve may be faired through these results which falls within ± 15% of over 80% of the data points. This curve, represented by

$$\eta = \frac{1}{1 + 3.6 \frac{C_{H_o}\bar{x}}{Ms}} - 0.25 \quad , \tag{15}$$

is merely Haering's result minus the term 0.25. Although admittedly empirical, this provides at least an estimate of the cooling effectiveness which could be expected by the use of multiple rows of discrete holes.

The cooling effectiveness data measured behind the first blowing row on the suction surface are shown in Fig. 55, along with the single slot correlation of Haering,[16] the empirical Eq. (15), and the transpiration-cooling correlation of Bartle and Leadon,[18] where the latter has been calculated using the assumption that the coolant emitted from the first row of holes is instead transpired from the surface uniformly over the same distance x.

Since the present S blowing data are felt to represent a lower bound on the film cooling attained by the present cooling schemes, a curve has also been faired through it such that, when taken with Eq. (15), the two curves represent the upper and lower limits of all single-row discrete hole data obtained in this study. The S blowing curve may be represented by

$$\eta = \frac{1}{1 + 3.6 \frac{C_{H_o}x}{Ms}} - 0.45 \quad , \tag{16}$$

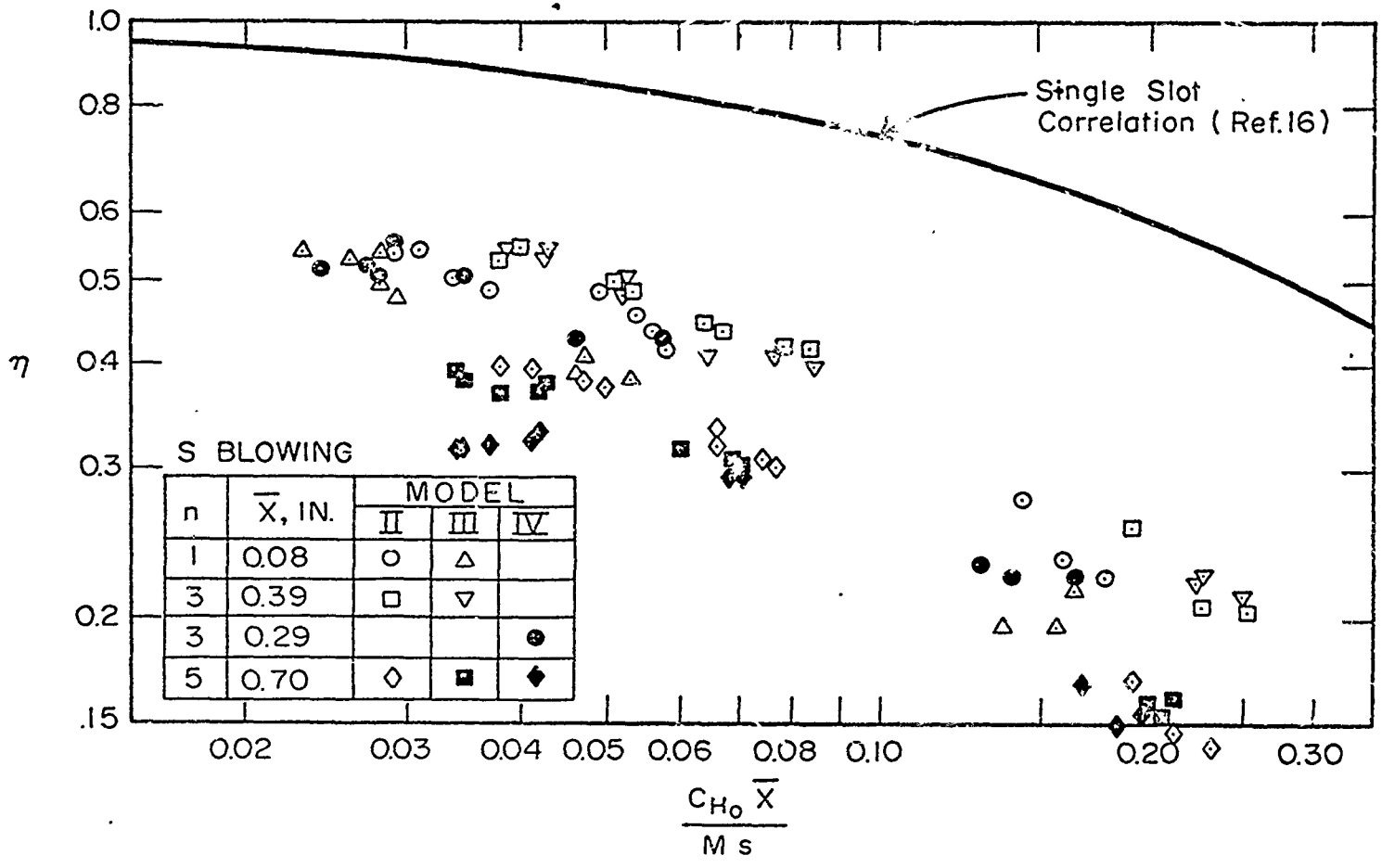

Fig. 53 - Suction surface cooling effectiveness data for S blowing correlated by $\bar{x}$

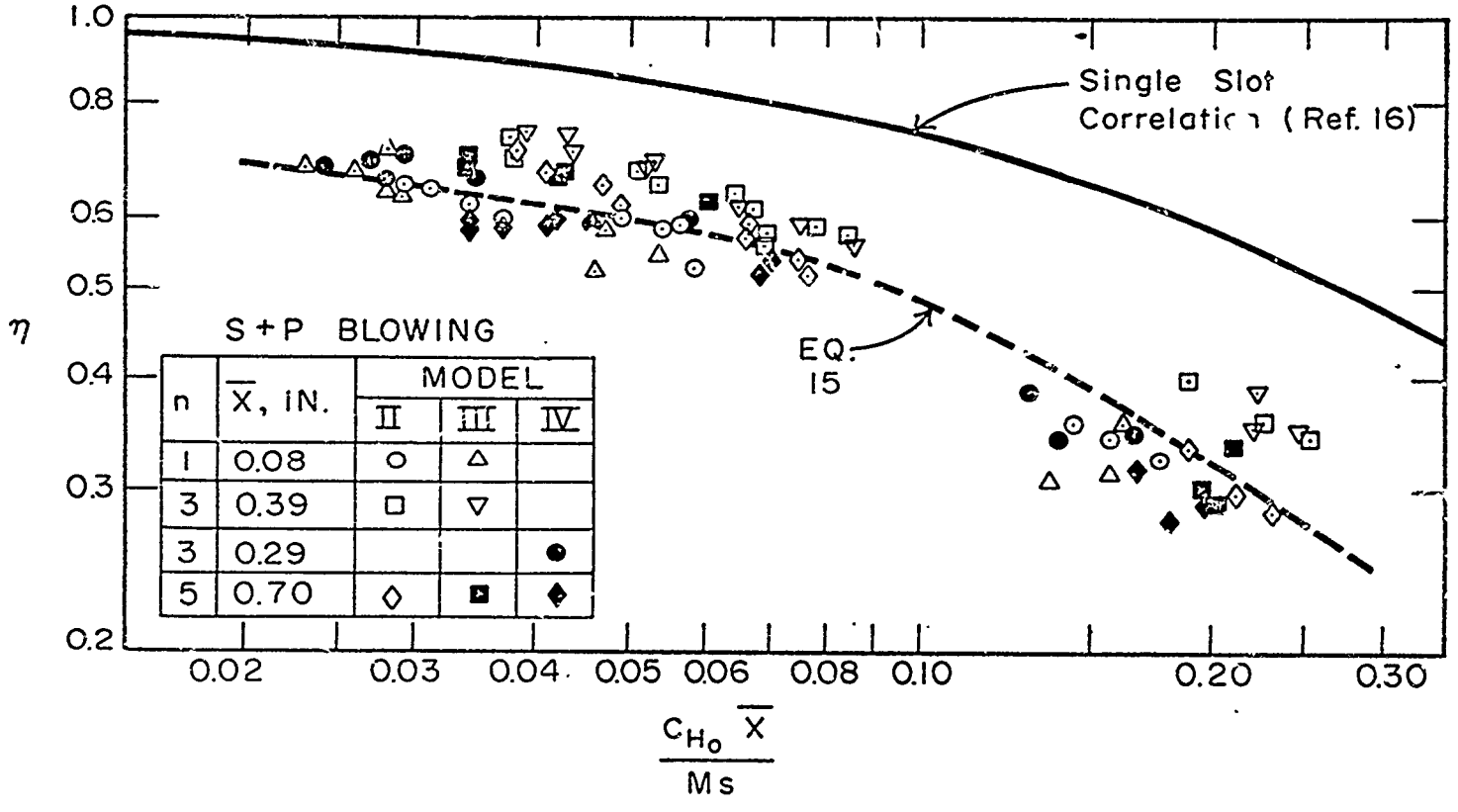

Fig. 54 - Suction surface cooling effectiveness date for S.+ P blowing correlated by $\bar{x}$

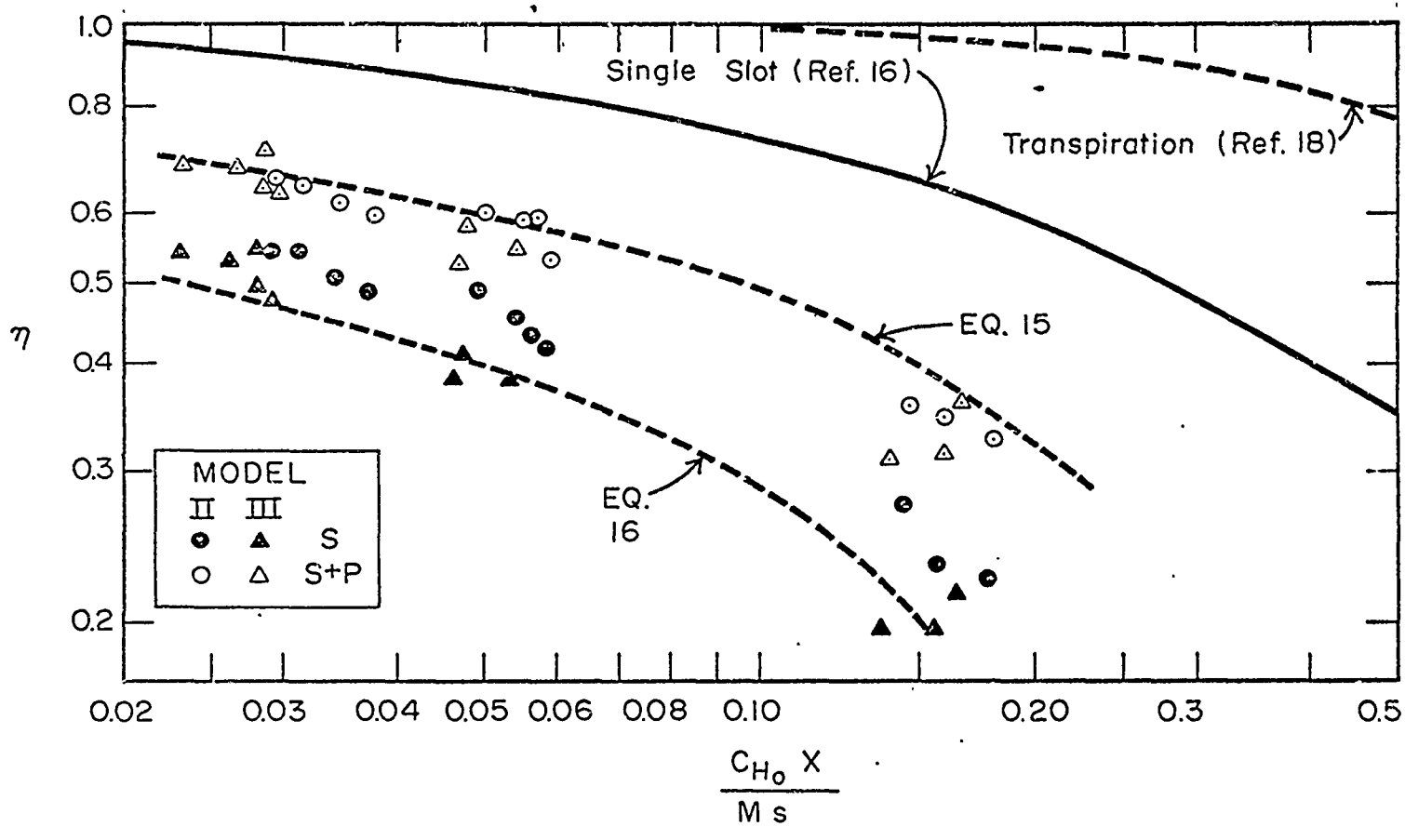

Fig. 55 - Suction surface single row cooling effectiveness data compared with single slot and transpiration cooling correlations

Unlike the situation for multiple-row hole data, some single-row data are available in the literature; namely, that of Metzger and Fletcher[12] who examined chordwise injection into a turbulent boundary layer using holes angled at $\varphi \approx 20°$ and 60° from the surface. No-blowing Stanton numbers have been calculated for their data under the assumption that the turbulent boundary layer began at the sandpaper strip which was located upstream of their blowing rows. Using these values and the faired curves representing their ± 10% accuracy correlations of each condition tested, upper and lower bounds for the effectiveness of their two injection angles have been shown in Fig. 56 along with Eqs. (15) and (16) for the present results. The variation in η within a single geometry for the data of Reference 12 is due to differing values of the hole spacing and the mass flux ratio, M. This variation points out the complexity of the dependence of η for discrete hole blowing on parameters in addition to $C_{H_O}x/Ms$ and φ. Goldstein et al.[11] have also found an apparently secondary dependence on M alone, particularly for the lateral spreading of the coolant with downstream distance. However, their results show that a vertical injection geometry enjoys generally better lateral spreading over a considerable range of M than does a geometry angled at $\varphi = 35°$ in the chordwise direction, so the dependence cannot be attributed to M alone. Examination of the present results for both multiple and single rows has revealed no apparent correlation with either M or hole spacing, although the present study made no attempt to vary the latter within geometries.

The most significant result of the present effectiveness results is the fact that discrete hole blowing, as applied to a typical airfoil in the present study, does not show a strong secondary dependence on geometry or mass flux ratio M alone, but does exhibit a primary dependence on $C_{H_O}x/Ms$, the same parameter which governs continuous slot film cooling.

E. CONCLUDING DISCUSSION

The experimentally measured static pressure distributions show that the aerodynamic effects of the present film-cooling technique were confined to the suction surface where coolant was injected through discrete holes into a region having an initially unfavorable pressure gradient and a turbulent boundary layer. This would be expected to increase the turbulent boundary layer thickness, particularly when the coolant added possessed no momentum component in the flow direction. Verification of this was found by Shaw,[20] whose Schlieren photographs of the suction surface of Models I and II show a rapid enlargement of the boundary layer with increasing blowing. This is also verified by the present wake survey measurements, such as shown in Fig. 30, where the wake width is greatly enlarged toward the suction surface. (See Appendix D, Summary of Schlieren Data.)

The results also indicate that separation occurs for non-chordwise injection in the vicinity of the rounded trailing edge but no evidence

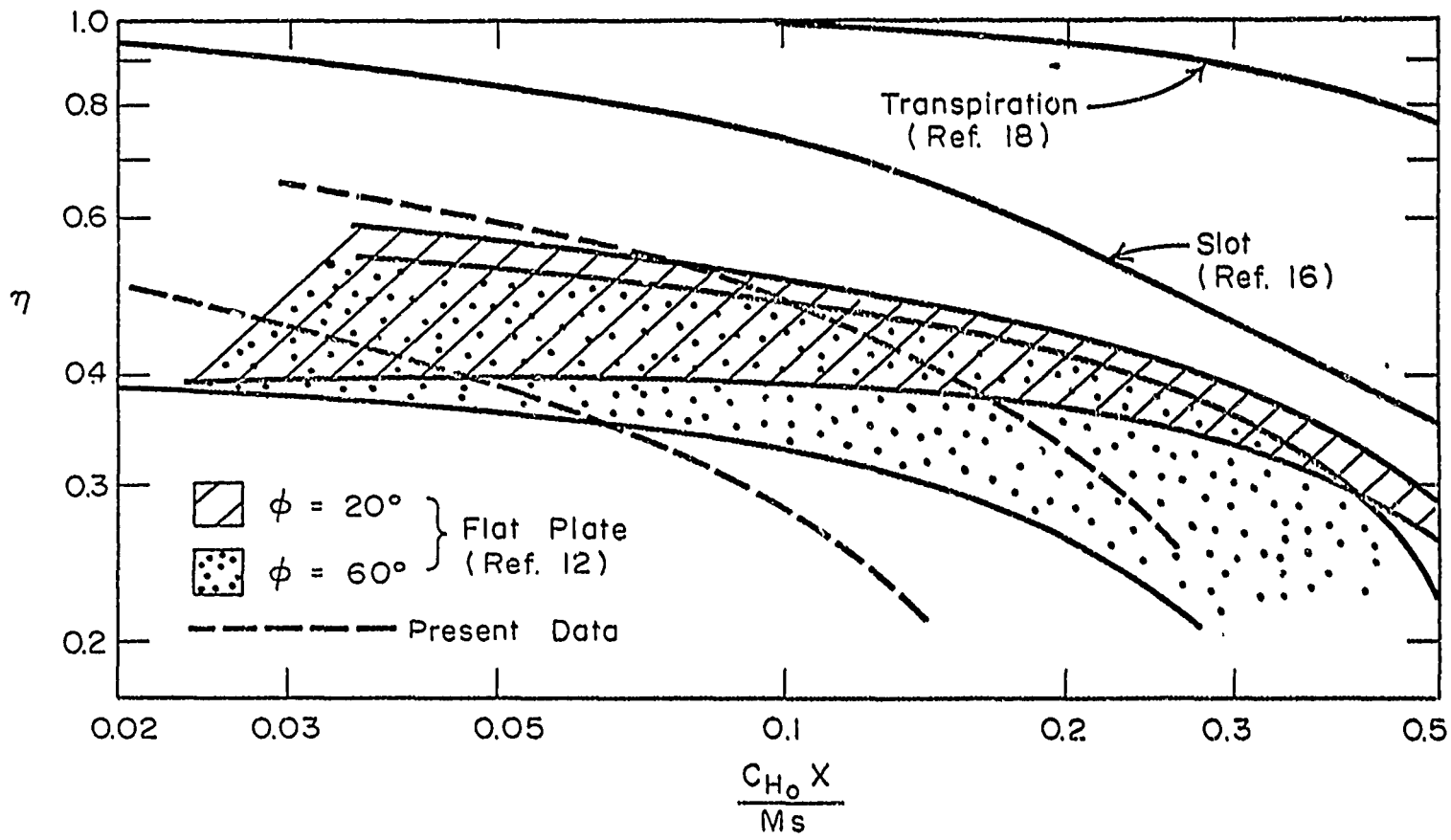

Fig. 56 - Comparison of available single-row discrete hole cooling effectiveness data bands

was found that this extended further upstream on the suction surface, not discounting the possibility of local r ions of separation near points of injection. The lack of massive aration is verified by the measured wake total pressure loss coefficients, which show no sudden increase with blowing, such as would be expected for a separated layer. Instead, the losses increased at a nearly constant rate with increasing blowing for 12° spanwise and 90° blowing, and at decreasing rates for 30° spanwise and chordwise injection. The fact that the simple ideal mixing analysis also predicts both the proper trends for ω and actual values which are reasonable indicates that a great amount of the measured loss phenomenon is due to effects apart from any large scale boundary layer separation. The intense thickening of the suction surface turbulent boundary layer for the non-chordwise blowing geometries is caused by the entrainment of the cool, low-momentum coolant in the layer. This layer receives more coolant at each succeeding row of holes and thus growth is stimulated by both mass addition and the positive pressure gradient.

The large loss of lift observed on the suction surface for non-chordwise blowing geometries can be attributed to the thickening of the effective airfoil profile in the blown region by the enlarging turbulent boundary layer, causing a pressure rise which feeds forward on the suction surface, as shown by the increase in suction surface pressure a considerable distance ahead of the injection region. The pressure rise ahead of the injection region is also seen for the transonic suction surface, where shock waves have been seen originating from the increase in effective body thickness occurring at the location of a hole row for non-chordwise injection.[20]

The cooling effectiveness data show that the amount of coolant, and not the method by which it was injected, was the primary factor in the cooling of the suction surface. This is in contrast to the results of Papell,[9] obtained using angled slots, in which a significant dependence on angle of injection was found. The continuous nature of slot injection, however, reduces the penetration height of the slot-injected coolant into the primary flow for equal values of the blowing parameter B when compared to the jet-like nature of discrete hole blowing. This implies that considerable lateral effectiveness variation must occur in discrete hole cooling, which has been verified by Goldstein et al.[11] using a single circular hole in an insulated flat plate. Such variations undoubtedly existed in the present experiment, but the conductive nature of the airfoil surface makes the present effectiveness data in reality averages over a finite area.

The discrete hole data of Metzger and Fletcher[12] also show a considerable dependence of effectiveness on blowing geometry (both angularity and spacing) and the mass flux ratio M. This latter parameter would be expected to play a more important role in discrete hole cooling than for slot cooling since M is an indication of the penetrating ability of an individual coolant jet. The fact that the present results

show no discernable dependence on M (other than the expected trend with $C_{H_O}x/Ms$) or on blowing geometry indicates that the rapid growth of the suction surface boundary layer accelerates mixing and thus the coolant injected through various hole geometries is more evenly distributed.

Although the differences in the effect of chordwise and vertical injection on the suction surface boundary layer and the ensuing losses can be explained in the basis of streamwise momentum conservation, it is not obvious what mechanism caused the reduction in momentum losses for the 30° spanwise S blowing at higher values of B. Significant spanwise velocity components in the boundary layer must be induced by such injection, particularly nearer the surface where chordwise velocity is lower. The overall penetration of the spanwise angled injection into the boundary layer would appear to be the same as that of vertical injection since the total amount of coolant stream crossing the airfoil surface for each case will, by virtue of the matching of $(\rho u)_{cy}$, possess the same vertical component of the mass flux ratio M. A coolant jet emitted from the surface in a spanwise angular orientation may begin chordwise turning within the elliptical "trench" near the surface and thus acquire a chordwise velocity component prior to crossing the surface plane. This is a possible explanation of the reduction in momentum losses for the 30° spanwise S blowing at large blowing rates, but a detailed description of the complex three-dimensional flow field induced by discrete hole blowing must await a detailed probing of the blown layer to obtain both chordwise and lateral velocity profiles over the entire region.

The present results show that the significant variations in discrete hole film cooling which have been measured in flat plate experimental studies are not present in the actual application of this cooling technique to the suction surface region of a typical turbine airfoil. Instead, the observed variations in lift and momentum losses due to blowing geometry differences are, at the massive blowing rates, a more important consideration in an application such as has been examined here.

VI. SUMMARY AND CONCLUSIONS

The aerodynamic effects of film cooling through multiple rows of discrete holes located in the region aft of midchord on both surfaces of a typical turbine airfoil have been studied experimentally at conditions simulating those found in actual turbines. Tests were performed with a single blade in a contoured channel using electrically heated air as the primary flow. Air at a nominal temperature of 75°F was used as coolant to investigate the effects of coolant-to-primary flow rates as high as 0.05, based on blowing from the single blade.

Heat transfer rates in the absence of blowing were also measured over the injection region of both surfaces to determine both the state of the unblown boundary layer and to determine no-blowing Stanton numbers for use in the correlation of film-cooling effectiveness. The results of these tests show that a turbulent boundary layer exists over the injection region of both surfaces for the conditions of the film cooling testing.

Four film-cooling models were tested, each having differing angular hole geometries with respect to the chordwise and spanwise directions. Surface-to-hole axis angles tested were 12° spanwise, 30° spanwise, 90° (vertical), 30° chordwise (suction surface), and 20° spanwise (pressure surface). Measurements were made of suction surface cooling effectiveness, static pressure distributions, and integrated wake momentum losses in the form of the total pressure loss coefficient, ω. Two inlet-to-exit pressure ratios of 1.5 and 1.7 were used to enable suction surface blowing into subsonic and transonic regions, respectively.

No significant effect of pressure surface blowing was found on either the lift distribution or the wake total pressure losses. Significant effects, however, were noted for suction surface blowing, particularly for non-chordwise injection. Large loss of lift and greatly increased flow losses were found for suction surface blowing which was angled in the spanwise direction or at 90° to the surface. This is due to the greatly thickened turbulent boundary layer which is induced by blowing in a region of positive pressure gradient. Some reduction of losses was observed for 30° spanwise blowing at higher blowing rates when compared to losses measured for vertical injection. Losses measured for 12° spanwise blowing were approximately the same as those for the vertical case, but any conclusion regarding the aerodynamic efficiency of the 12° geometry would be premature, since evidence now exists showing that the actual coolant injection angle for the 12° spanwise blowing was considerably larger. The reduction of losses by spanwise injection for the 30° case was quite apparent at high blowing rates, but at the lowest rates tested all geometries showed approximately equal momentum losses.

The lowest losses and least affected lift distributions for the higher blowing rates were measured for the 30° chordwise blowing.

Aerodynamic superiority of this geometry improved as coolant flow rate was increased, a fact which is predicted by simple momentum conservation.

No evidence was found of boundary layer separation on the suction surface other than in the immediate vicinity of the trailing edge, downstream of the final row of discrete holes.

Suction surface temperatures measured during film cooling of both airfoil surfaces provide the best indication of cooling effectiveness which such an airfoil would enjoy in actual operation. A comparison of measured effectiveness shows no apparent dependence on blowing geometry within the accuracy of the measurements. It is found that the present effectiveness results, obtained using multiple rows of nearly equal spacing, are best correlated in the standard film cooling manner using as the downstream coordinate an average of the distances to each of the upstream rows. The present data, based on this parameter, fall an average of $\Delta\eta = 0.25$ below the predicted effectiveness of continuous slot injection. These results should be interpreted as an upper bound on the actual film cooling effectiveness which was achieved, since internal conduction effects could not be eliminated in the present investigation. The effectiveness results show that for the conditions of this investigation, the overall cooling effectiveness achieved by massive discrete hole blowing is primarily dependent on the amount of coolant injected and that blowing geometry, within the extremes tested, plays a secondary role.

It is concluded that because of the large reduction in flow losses achieved by chordwise injection on the suction surface and the apparent relative independence of cooling effectiveness on injection geometry, the chordwise injection at 30° from the surface is the optimum choice among the geometries tested.

APPENDIX A

CALCULATION OF THE IDEAL MIXING TOTAL PRESSURE LOSS COEFFICIENT

The injection of coolant into a confined flow, such as the passage between airfoils in a cascade or the passage in which the present film-cooled airfoils were tested, will introduce a change in fluid properties at the channel exit for most conditions. This effect, although influenced by boundary layers and viscous effects, will also occur in their absence. It is helpful in interpreting the experimental values of ω to examine the flow through the test region in this manner, treating the flow around the airfoil as a channel flow.

Figure 57 shows the assumed physical model chosen for the calculation. Stations 1 and 2 correspond to the like-numbered stations in the test facility, the simulated turbine inlet and exit, respectively. The j and k stations correspond to points upstream and downstream of the region of blowing, defining a region within which all mixing of the coolant and primary flow is assumed to occur. The flow is isentropically expanded from the inlet station 1 to station j. Between j and k the mixing occurs in a constant area, insulated channel. This assumption is reasonable for the present experiment since the total flow area changes very little in the region of blowing. The conditions at j are chosen to represent the average flow properties of the channel in the injection region. Between stations j and k the equations of continuity, momentum, energy, and state are used to obtain conditions at k, including the total pressure. The flow at k is then expanded isentropically to the selected downstream static pressure, based on the chosen P_{t_1}/P_2.

The equations for conservation of mass, momentum, and energy for the mixing of like gases are

$$\dot{m}_j + \dot{m}_c = \dot{m}_k \quad , \tag{17}$$

$$P_j A_j + \dot{m}_j u_j + \dot{m}_c u_c \cos \varphi = \dot{m}_k u_k + P_k A_k \quad , \text{ and} \tag{18}$$

$$\dot{m}_j c_p T_{t_j} + \dot{m}_c c_p T_{t_c} = \dot{m}_k c_p T_{t_k} \quad . \tag{19}$$

The momentum Eq. (18) is written for the assumption that the coolant enters the primary flow at the local static pressure of the injection region, while the energy Eq. (19) assumes that both gases are calorically perfect. Defining $\dot{m}_c/\dot{m}_1 \equiv \xi$, the energy equation is solved as

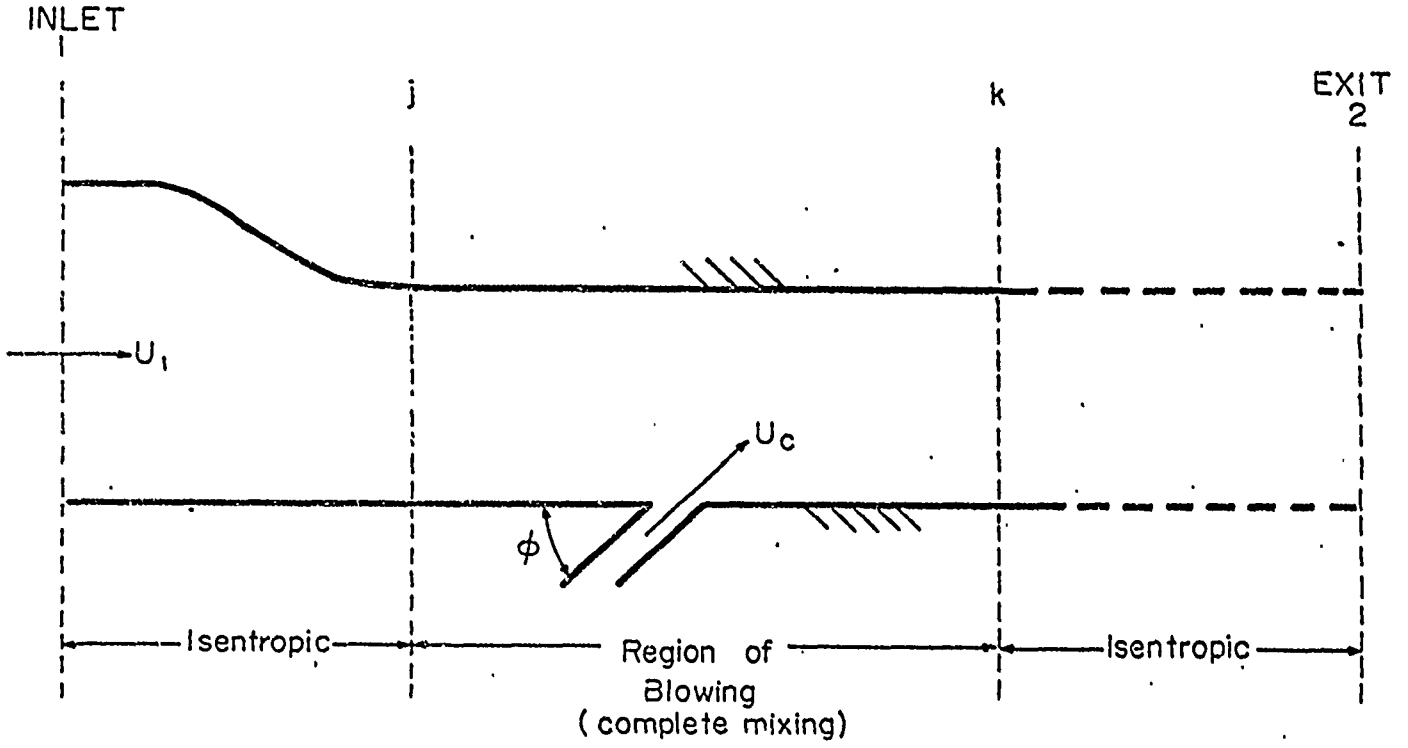

Fig. 57 - Physical model assumed for calculation of ideal mixing total pressure loss coefficient ω

$$T_{t_k} = \frac{T_{t_1} + \xi T_{t_c}}{1 + \xi} \quad , \tag{20}$$

and the momentum equation becomes

$$\frac{P_j}{\rho_j u_j^2} + 1 + \xi \frac{u_c}{u_j} \cos \varphi = (1+\xi) \left(\frac{u_k}{u_j} + \frac{P_k}{\rho_k u_k u_j} \right) \quad . \tag{21}$$

Employing the perfect gas relationships

$$u_k = a_{t_k} \frac{M_k}{\sqrt{1 + \frac{\gamma-1}{2} M_k^2}}$$

and

$$\frac{P_k}{\rho_k u_k^2} = \frac{1}{\gamma M_k^2} \quad ,$$

the right hand side of Eq. (21) becomes

$$(1+\xi) \left(\frac{a_{t_k}}{u_j} \right) \left[\left(M_k + \frac{1}{\gamma M_k} \right) \left(\frac{1}{\sqrt{1 + \frac{\gamma-1}{2} M_k^2}} \right) \right] \quad .$$

The momentum Eq. (21) is thus written

$$\frac{P_j}{\rho_j u_j^2} + 1 + \xi \frac{u_c}{u_j} \cos \varphi = \Lambda \chi \quad , \tag{22}$$

where

$$\Lambda = (1+\xi) \frac{a_{t_k}}{u_j}$$

and

$$\chi = \frac{M_k + \frac{1}{\gamma M_k}}{\sqrt{1 + \frac{\gamma-1}{2} M_k^2}} \quad .$$

This allows an implcit solution for M_k since all other quantities in the momentum Eq. (22) may either be calculated or are known. Using

the perfect gas equation of state

$$P_k = \rho_k R T_k$$

and the relationship

$$\rho_k = \frac{(1+\xi)\ \dot{m}_1}{M_k A_k \sqrt{\gamma R T_k}} ,$$

we obtain

$$\frac{P_{t_1}}{P_{t_k}} = \underbrace{\left(\frac{P_{t_1} \gamma A_k}{(1+\xi)\ \dot{m}_1 a_{t_k}} \right)}_{P(\xi)} \underbrace{\left(\frac{M_k (P_k/P_{t_k})}{\sqrt{T_k/T_{t_k}}} \right)}_{Q(M_k)} \qquad (23)$$

The term $P(\xi)$ in Eq. (23) is a function only of ξ and the prescribed total temperatures of the inlet and coolant flows, while $Q(M_k)$ is a function of M_k only. Thus the calculation of P_{t_1}/P_{t_k} (equal to P_{t_1}/P_{t_2}) may be made graphically with the use of $\chi = \chi(M_k)$ and $Q = Q(M_k)$ curves. M_k is used as an intermediate parameter since the value of P_k/P_{t_k} must be found in order to expand the flow to P_2 and this is most easily done by using M_k, which determines P_k/P_{t_k} for constant γ.

The parameters which are important in determining the total pressure changes (or ω) are evident from the solution, which, it must be remembered, assumes that the same perfect gas is used for coolant and primary flows. The major parameters are M_j, T_{t_c}, T_{t_1}, ξ, u_c, P_{t_1}/P_2, and φ.

Solutions for ω have been obtained for assumed conditions which approximate those of the present experiments. These solutions are plotted in Figs. 58 and 59 for

$$T_{t_1} = 500°F,\ 1000°F ,$$

$$T_{t_c} = 75°F ,$$

$$M_j = 0.65 ,$$

$$M_1 = 0.35 ,$$

$$P_{t_1} = 45 \text{ psia, and}$$

$$\varphi = 0°,\ 30°,\ 90° .$$

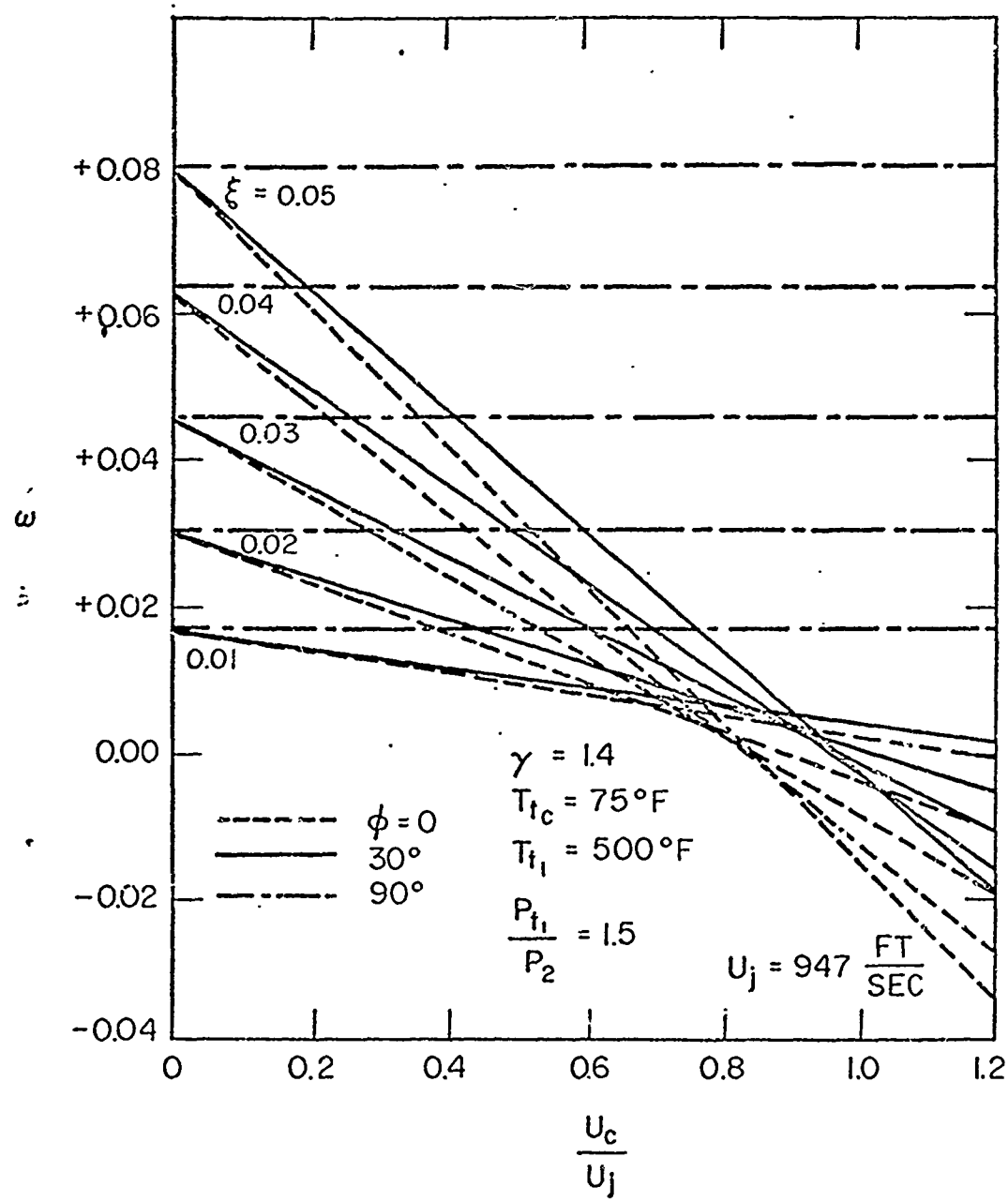

Fig. 58 - Ideal mixing solution for total pressure loss coefficient ω at T_{t_1} = 500°F

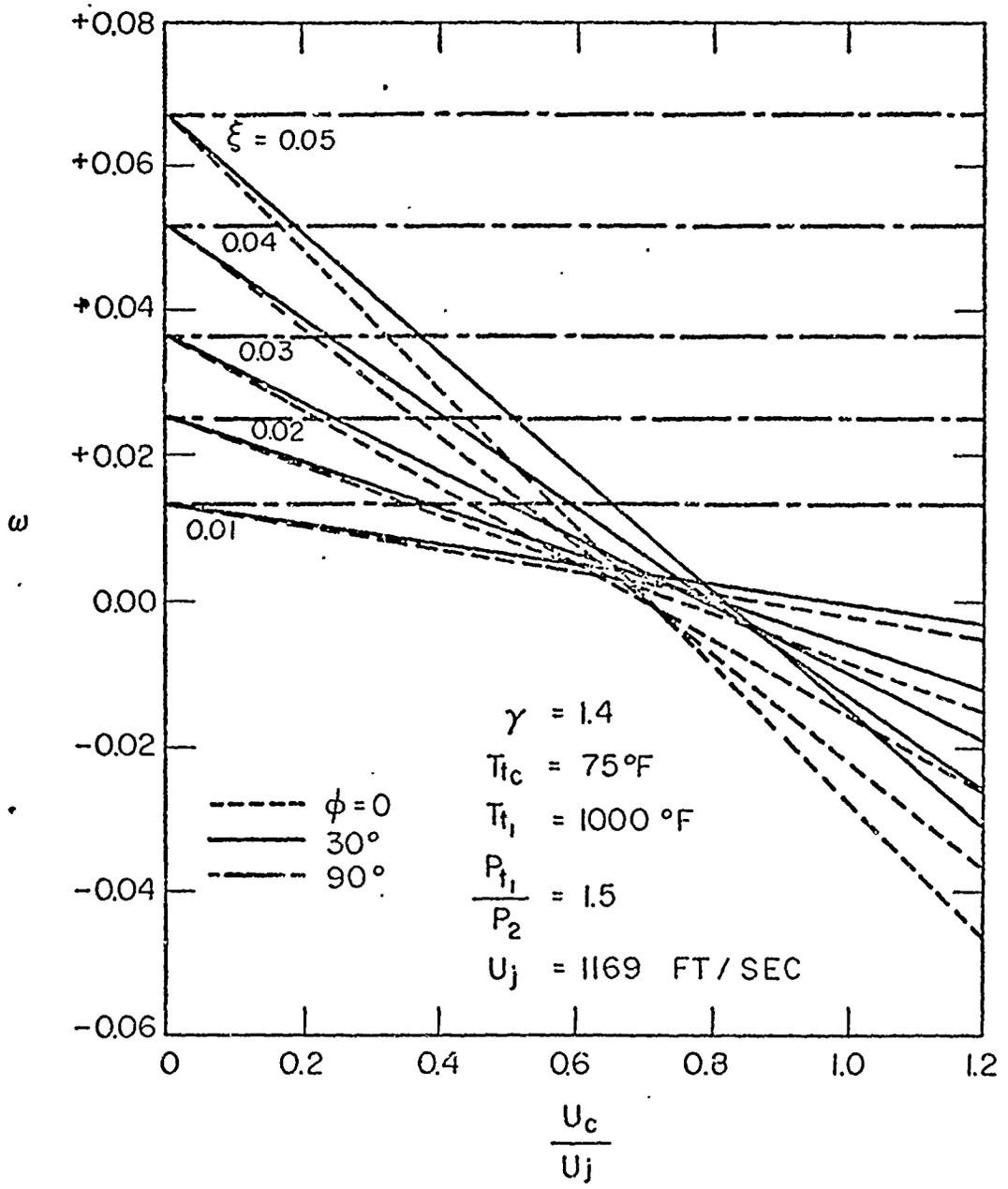

Fig. 59 - Ideal mixing solution for total pressure loss coefficient ω at T_{t_1} = 1000°F

The solutions for $\varphi = 90°$ are horizontal lines for each ξ value, independent of u_c/u_j. This may be seen from Eq. (22) which, for $\varphi = 90°$, becomes

$$\chi = \left(\frac{P_j}{P_j u_j^2} + 1\right) \Bigg/ \left((1+\xi)\,\frac{a t_k}{u_j}\right),$$

and thus ω for this case is a function of ξ only. A family of constant ξ straight lines is generated for each φ, each line intercepting the $u_c/u_j = 0$ axis at the value of ω for $\varphi = 90°$ and the particular ξ.

Several general conclusions may be drawn from Figs. 58 and 59. The clear superiority of injection in the streamwise direction is quite obvious, as is the fact that $\varphi = 30°$ injection in the chordwise direction is very close to the optimum tangential case from the standpoint of momentum losses. Another significant point is the fact that at sufficiently high velocities the flow is energized by the coolant injection and negative values of ω are achieved. This is of interest in considering massive blowing rates, where high velocities are more apt to be achieved in practical applications. Achieving such velocities in the actual engine application is a problem, however, since compressor outlet total pressure is generally the highest pressure available in the engine for coolant supply. Another conclusion gained from the solutions is the decrease of losses with increasing T_{t_1}/T_{t_c}, although care must be exercised in comparing the solutions to account for the difference in u_j. Thus equal values of u_c require entering the plots of two different values of u_c/u_j.

The two-dimensional analysis does not distinguish between geometries angled in the spanwise direction, thus for the present study the 12°, 20°, and 30° spanwise angled geometries are all considered $\varphi = 90°$ cases. The three angular cases ($\varphi = 0°$, 30°, and 90°, chordwise angles) are compared for typical conditions of this experiment in Fig. 45.

APPENDIX B

ESTIMATION OF THE MAXIMUM ERROR IN η DUE TO UNCERTAINTY IN T_c

In this section an estimate is made of the maximum possible error in η because of the assumption that $T_c = 75°F$ for all film-cooling data obtained in the present experiment. Air initially at a temperature of 40°F (± 5°F) was used as the coolant, but internal heating of this air as it passed through the blade interior raised the coolant temperature in amounts depending on the coolant flow rate and internal blade temperature. The following analysis estimates the error introduced by the assumption that $T_c = 75°F$ by considering the extremes of internal coolant heating. The extreme condition of no coolant heating may be easily calculated. The condition of maximum possible heat transfer to the coolant is treated in the following analysis.

Consider the turbine airfoil to be represented by a flat plate having a total surface area equal to the surface area of the airfoil, $A = 8$ in.^{2}. Assuming that during film cooling of the model there is heat transferred to the model rather than the adiabatic condition normally assumed, an energy balance equation may be written as

$$\dot{m}_c C_p \Delta T_c = \bar{\dot{q}} A \quad , \tag{24}$$

where c_p = specific heat of air and $\bar{\dot{q}}$ = average heat transfer to a unit surface area of the model. This balance assumes that all heat transferred to the model is in turn transferred to the coolant as it passes through the model interior. Equation (24) may be written

$$\dot{m}_c C_p \Delta T_c = C_H \rho_1 u_1 c_p (T_{t_1} - T_w) A$$

or

$$\Delta T_c = \frac{C_H \rho_1 u_1 (T_{t_1} - T_w) A}{\dot{m}_c} \quad , \tag{25}$$

where it is assumed that the entire model is at temperature T_w. Using the fact that $\dot{m}_1 = \rho_1 u_1 A_1$ and $\xi \equiv \dot{m}_c / \dot{m}_1$, Eq. (25) becomes

$$\Delta T_c = \frac{C_H}{\xi} \frac{A}{A_1} (T_{t_1} - T_w) \quad . \tag{26}$$

A turbulent boundary layer is assumed to exist over the entire surface to provide the maximum heating possible. The turbulent Stanton number for the f at plate may be expressed as $C_H = .029/Re_x^{0.2}$

Reynolds number values typical of the midchord of the airfoil for the present experimental conditions are

$$Re_x = \begin{cases} 460{,}000 \text{ for } T_{t_1} = 500°F \\ 283{,}000 \text{ for } T_{t_1} = 1000°F. \end{cases}$$

Values of the Stanton number thus calculated are

$$C_H = \begin{cases} 0.0021 \text{ for } T_{t_1} = 500°F \\ 0.0024 \text{ for } T_{t_1} = 1000°F. \end{cases}$$

If $C_H = 0.0023$ is taken as an average value, Eq. (26) becomes

$$\Delta T_c = 0.0056 \frac{T_{t_1} - T_w}{\xi} \quad , \tag{27}$$

where $A/A_1 = 2.42$. Using the fact that

$$\eta = \frac{T_{w_o} - T_w}{T_{w_o} - T_c} \approx \frac{T_{t_1} - T_w}{T_{t_1} - T_c} \quad ,$$

the "true" η may be calculated using

$$\eta_{TRUE} = \eta_{MEASURED} \left[\frac{T_{t_1} - 75°F}{T_{t_1} - (40°F + \Delta T_c)} \right]$$

or

$$\eta_{TRUE} = \eta_{MEASURED} \left[\frac{T_{t_1} - 75°F}{T_{t_1} - (40°F + .0056/\xi)} \right] . \tag{28}$$

The bracketed term in Eq. (28) may be considered the correction factor which will tend to a value of 1 as T_{t_1} is increased. Equation (28) has been solved for the case of $T_{t_1} = 500°F$ since this is the experimental condition which will possess the greatest error in η due to internal coolant heating.

The solutions for various values of $\eta_{measured}$ are shown in Fig. 60 as solid lines, and the dashed lines in the same figure are for the condition of no coolant heating. The actual error in η lies somewhere between the solid and dashed lines for the same measured η. The solution shows that for the blowing rates and resulting η values of this

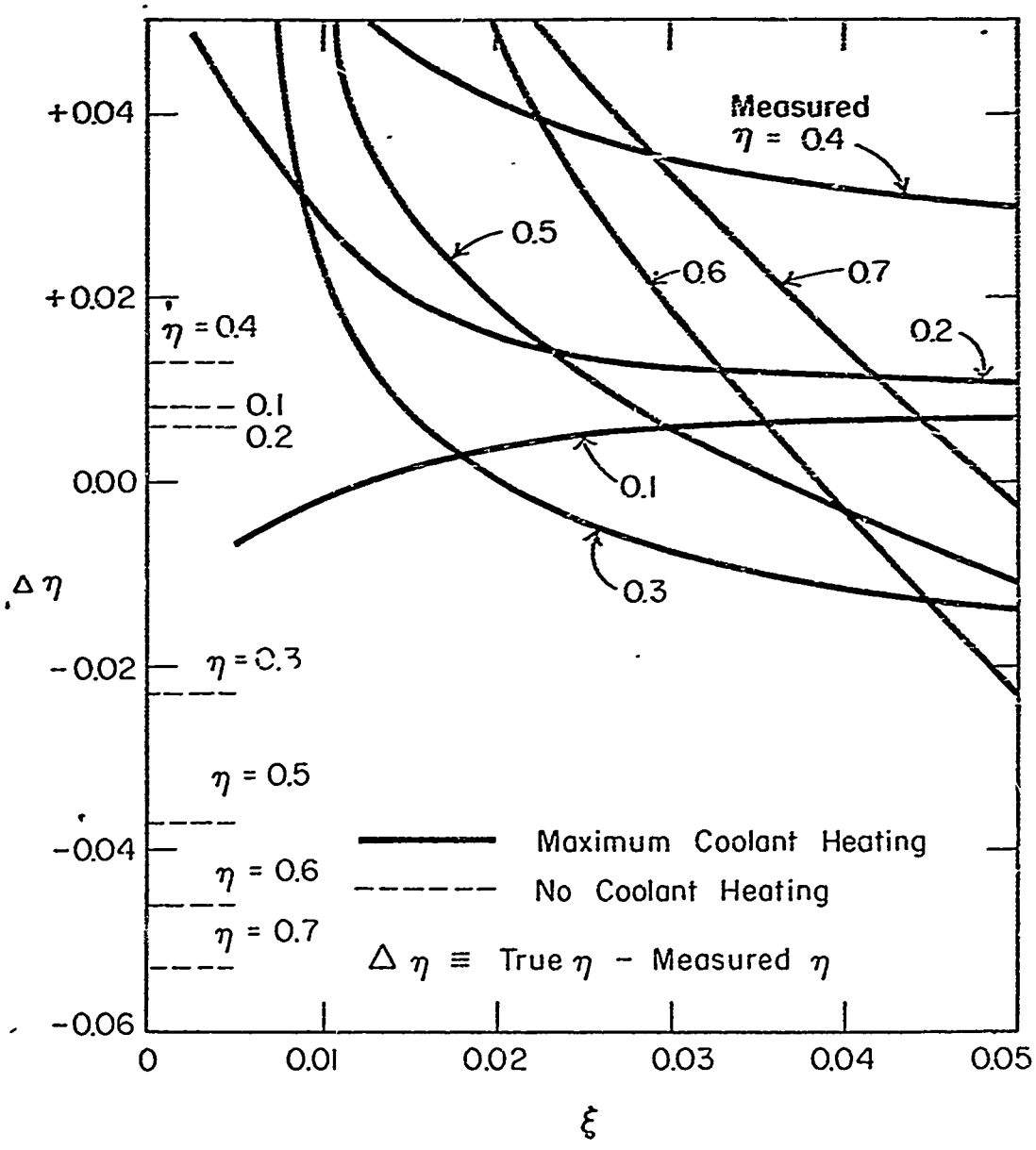

Fig. 60 - Maximum error in η measurements due to assumption $T_c = 75°F$ for the case $T_{t_1} = 500°F$

investigation, the error in η is generally less than 0.03. It should be also pointed out that a similar solution for $T_{t_1} = 1000°F$ will resemble Fig. 60, however both the solid and dashed curves for the $T_{t_1} = 1000°F$ case will be located approximately 50% nearer the $\Delta\eta = 0$ abcissa than shown in Fig. 60.

APPENDIX C

DATA TABLES

Table III - Static Pressure Data for Model I, T_{t_1} = 500°F, P_{t_1}/P_2 = 1.5

Blowing	$10^2\xi$	B	P_{t_1} psia	$\frac{P_1}{P_{t_1}}$	Suction surface x, inches						Pressure surface x, inches				
					.408	.790	1.037	1.241	1.522	2.079	.366	.600	.806	1.032	1.513
					P/P_{t_1}										
-	0.00	0.0	44.61	0.916	.742	.586	0.609	0.605	0.618	0.643	.943	.936	.925	0.903	0.858
S	0.44	1.87	45.00	.916	.749	.605	.631	.623	.641	.659	.941	.933	.921	.900	.856
P	0.44	1.87	44.65	.916	.742	.589	.613	.607	.621	.647	.945	.937	.924	.904	.857
S+P	0.90	1.91	45.08	.917	.749	.605	.631	.623	.643	.660	.942	.937	.924	.902	.854
a	0.91	-	44.83	.918	.747	.592	.614	.608	.621	.649	.945	.937	.927	.907	.862
b	1.79	1.89	45.38	.919	.753	.607	.631	.622	.640	.659	.945	.939	.926	.905	.857
S	1.29	5.48	45.26	.919	-	.633	.662	.636	.664	.666	.942	.934	.923	.902	.858
P	1.29	5.48	44.99	.918	.742	.588	.611	.606	.620	.648	.947	.943	.927	.906	.854
S+P	2.54	5.39	45.86	.919	.760	.631	.658	.633	.661	.666	.943	.940	.924	.903	.850
a	2.56	-	45.52	.919	.752	.596	.612	.603	.616	.641	.946	.940	.929	.909	.864
b	5.10	5.41	46.80	.923	.767	.633	.653	.627	.655	.661	.948	.945	.929	.910	.856
S	2.21	9.39	45.84	.919	.771	.655	.685	.631	.676	.670	.940	.933	.921	.899	.855
P	2.23	9.47	45.31	.918	.741	.587	.609	.605	.619	.647	.948	.946	.928	.912	.849
S+P	4.42	9.39	46.70	.922	.770	.653	.682	.637	.676	.674	.946	.944	.925	.909	.846
a	4.46	-	46.26	.921	.758	.600	.611	.602	.616	.641	.947	.941	.931	.913	.866
b	8.77	9.37	48.23	.929	.783	.659	.678	.632	.671	.671	.954	.952	.935	.921	.860

a Denotes blowing from test cabin walls only.
b Denotes blowing from test cabin walls and both model surfaces.

Table IV - Static Pressure Data for Model I, T_{t_1} = 1000°F, P_{t_1}/P_s = 1.5

Blowing	$10^2 f$	B	P_{t_1} psia	$\frac{P_1}{P_{t_1}}$	Suction surface x, inches						Pressure surface x, inches				
					.480	.790	1.037	1.241	1.522	2.079	.366	.600	.806	1.032	1.513
					P/P_{t_1}										
-	0.00	0.0	44.65	0.919	.747	.600	0.626	0.636	0.641	0.670	.945	.938	.927	0.907	0.856
S	1.30	5.52	45.05	.914	.757	.624	.655	.631	.658	.662	.937	.929	.919	.897	.852
P	1.34	5.69	44.67	.918	.740	.585	.609	.606	.618	.646	.945	.942	.926	.906	.854
S+P	2.67	5.67	45.32	.919	.756	.624	.654	.629	.657	.666	.943	.940	.925	.903	.850
a	2.66	-	45.16	.919	.752	.598	.615	.610	.621	.643	.944	.938	.927	.908	.873
b	5.36	5.69	46.25	.923	.764	.630	.654	.627	.656	.664	.947	.944	.930	.909	.858
S	2.12	9.00	45.33	.919	.766	.649	.679	.641	.673	.670	.928	.932	.920	.900	.855
P	2.13	9.04	45.10	.919	.739	.582	.607	.602	.615	.645	.947	.945	.926	.910	.850
S+P	4.23	8.99	46.00	.922	.766	.646	.674	.639	.670	.674	.950	.942	.926	.905	.849
a	4.35	-	45.43	.922	.758	.604	.616	.610	.621	.644	.947	.941	.931	.912	.868
b	8.70	9.22	47.18	.930	.780	.656	.677	.636	.671	.672	.954	.952	.936	.918	.860
S	2.77	11.76	45.17	.926	.780	.669	.697	.645	.687	.679	.947	.938	.925	.900	.861
P	2.72	11.55	44.65	.922	.742	.587	.608	.604	.619	.651	.950	.947	.929	.914	.870
S+P	5.39	11.43	46.21	.927	.776	.663	.691	.640	.682	.679	.952	.951	.931	.916	.851
a	5.62	-	45.52	.932	.771	.612	.618	.612	.625	.651	.957	.950	.941	.922	.876
b	10.31	10.97	48.33	.929	.785	.664	.683	.631	.674	.672	.950	.951	.934	.919	.856

a Denotes blowing from test cabin walls only.
b Denotes blowing from test cabin walls and both model surfaces.

Table V - Static Pressure Data for Model II, T_{t_1} = 500°F, P_{t_1}/P_2 = 1.5

Blowing	$10^2\xi$	B	P_{t_1} psia	$\frac{P_1}{P_{t_1}}$	Suction surface x, inches						Pressure surface x, inches				
					.408	.790	1.037	1.241	1.522	2.079	.366	.600	.806	1.032	1.513
					P/P_{t_1}										
-	0.0	0.0	44.78	0.905	.720	.569	0.574	0.574	0.586	0.624	.936	.927	.916	0.897	0.853
S	1.22	4.27	45.60	.911	.744	.631	.632	.628	.633	.653	.936	.928	.916	.896	.851
S+P	2.41	4.21	46.08	.912	.743	.631	.634	.626	.634	.655	.940	.936	.917	.902	.845
S	2.09	7.31	46.24	.912	.762	.677	.663	.658	.647	.649	.923	.925	.914	.894	.847
P	2.10	7.34	45.64	.910	.717	.566	.572	.572	.585	.623	.942	.939	.916	.910	.844
S+P	4.18	7.31	47.02	.914	.760	.672	.659	.655	.646	.651	.941	.938	.914	.902	.837

Table VI - Static Pressure Data for Model II, T_{t_1} = 1000°F, P_{t_1}/P_2 = 1.5

Blowing	$10^2\xi$	B	P_{t1} psia	$\frac{P_1}{P_{t1}}$	Suction surface x, inches						Pressure surface x, inches				
					.408	.790	1.037	1.241	1.522	2.079	.366	.600	.806	1.032	1.513
					P/P_{t1}										
-	0.00	0.00	44.34	0.909	.722	.571	0.570	0.580	0.590	0.626	.938	.929	.918	0.899	0.854
S	0.43	1.50	44.68	.909	.730	.591	.594	.603	.613	.646	.937	.929	.917	.897	.853
P	0.43	1.51	44.54	.910	.722	.569	.573	.579	.590	.627	.939	.932	.921	.901	.854
S+P	0.88	1.53	44.68	.900	.730	.589	.596	.600	.611	.647	.939	.931	.920	.902	.853
S	1.28	4.48	45.12	.919	.744	.630	.635	.638	.643	.663	.946	.936	.929	.905	.859
P	1.24	4.34	44.77	.910	.721	.568	.574	.576	.588	.626	.942	.938	.920	.905	.851
S+P	2.49	4.35	45.41	.914	.743	.628	.628	.626	.633	.659	.943	.938	.921	.906	.849
S	2.01	7.03	45.57	.911	.760	.671	.661	.660	.656	.657	.936	.926	.915	.895	.848
P	2.04	7.14	45.10	.912	.721	.568	.577	.574	.586	.626	.945	.941	.921	.908	.847
S+P	4.07	7.12	46.16	.919	.757	.662	.655	.654	.653	.659	.944	.942	.890	.907	.842

Table VII - Static Pressure Data for Model II, T_{t_1} = 500°F, P_{t_1}/P_2 = 1.7

Blowing	$10^2\bar{\xi}$	B	P_{t_1} psia	$\frac{P_1}{P_{t_1}}$	Suction surface x, inches						Pressure surface x, inches				
					.408	.790	1.037	1.241	1.522	2.079	.366	.600	.806	1.032	1.513
					P/P_{t_1}										
-	0.00	0.00	42.85	0.901	.703	.531	0.513	0.466	0.427	0.504	.930	.919	.906	0.882	0.826
S	.43	1.51	42.83	.911	.726	.567	.557	.544	.559	.622	.952	.943	.930	.908	.857
P	.43	1.52	42.46	.901	.703	.533	.517	.469	.445	.524	.932	.924	.910	.886	.829
S+P	.87	1.52	42.60	.902	.708	.546	.529	.512	.494	.560	.932	.924	.910	.887	.828
S	1.26	4.41	42.98	.904	.724	.592	.571	.558	.556	.576	.930	.921	.907	-	.830
P	1.27	4.45	42.55	.905	.704	.534	.518	.470	.442	.522	.938	.933	.911	.895	.823
S+P	2.56	4.48	43.26	.909	.724	.588	.568	.553	.553	.579	.939	.934	.913	.896	.825
S	2.21	7.73	43.47	.908	.741	.639	.609	.596	.572	.577	.932	.922	.916	.886	.830
P	2.20	7.70	42.85	.907	.689	.522	.506	.458	.433	.511	.920	.946	.891	.877	.803
S+P	4.42	7.73	44.21	.911	.740	.635	.605	.591	.571	.578	.939	.938	.910	.896	.818

Table VIII - Static Pressure Data for Model II, T_{t_1} = 1000°F, P_{t_1}/P_2 = 1.7

Blowing	$10^2\xi$	B	P_{t_1} psia	$\frac{P_1}{P_{t_1}}$	Suction surface x, inches						Pressure surface x, inches				
					.408	.790	1.037	1.241	1.522	2.079	.366	.600	.806	1.032	1.513
					P/P_{t_1}										
-	0.00	0.00	41.96	0.907	.707	.535	0.502	0.473	0.447	0.521	.933	.925	.910	0.887	0.833
S	.44	1.55	42.12	.906	.710	.549	.512	.511	.514	.566	.933	.923	.910	.886	.834
P	.44	1.55	42.21	.904	.705	.533	.500	.472	.449	.524	.934	.926	.912	.890	.832
S+P	.89	1.55	43.32	.905	.709	.545	.510	.503	.507	.563	.935	.925	.913	.890	.831
S	1.28	4.48	42.71	.906	.722	.588	.570	.558	.556	.585	.932	.922	.909	.886	.832
P	1.27	4.46	42.88	.905	.706	.532	.503	.472	.441	.521	.936	.933	.912	.894	.827
S+P	2.53	4.42	43.39	.908	.704	.568	.547	.525	.478	.569	.915	.910	.891	.873	.807
S	2.11	7.39	43.46	.909	.737	.624	.623	.593	.580	.587	.933	.922	.909	.886	.831
P	2.12	7.42	43.10	.908	.706	.532	.506	.473	.443	.524	.940	.937	.912	.898	.824
S+P	4.20	7.35	44.17	.912	.736	.621	.597	.589	.575	.588	.939	.939	.911	.896	.820

Table IX - Static Pressure Data for Model III, $T_{t_1} = 500°F$, $P_{t_1}/P_2 = 1.5$

Blowing	$10^2\xi$	B	P_{t_1} psia	$\frac{P_1}{P_{t_1}}$	Suction surface x, inches						Pressure surface x, inches				
					.408	.790	1.037	1.241	1.522	2.079	.366	.600	.806	1.032	1.513
					P/P_{t_1}										
-	0.00	0.00	41.08	0.924	.715	.569	0.574	0.569	0.582	0.621	.929	.921	.909	0.889	0.845
S	.42	1.55	43.06	.926	.725	.587	.595	.589	.604	.636	.931	.922	.911	.892	.845
P	.47	1.72	42.82	.926	.718	.570	.574	.569	.582	.622	.936	.929	.916	.897	.848
S+P	.91	1.69	43.08	.928	.725	.587	.595	.589	.604	.638	.936	.928	.916	.896	.848
S	1.44	5.33	43.42	.931	.737	.615	.624	.620	.640	.643	.930	.921	.910	.891	.843
P	1.44	5.32	43.12	.930	.717	.568	.573	.564	.580	.622	.937	.930	.918	.897	.844
S+P	2.89	5.34	43.90	.932	.733	.613	.622	.617	.629	.651	.934	.927	.913	.893	.841
S	2.37	8.77	43.80	.932	.751	.642	.651	.653	.655	.653	.932	.922	.911	.890	.842
P	2.36	8.71	43.50	.930	.715	.566	.570	.563	.579	.621	.938	.933	.922	.894	.844
S+P	4.73	8.73	45.00	.935	.749	.640	.649	.651	.653	.656	.940	.933	.920	.896	.842

Table X - Static Pressure Data for Model III, T_{t_1} = 1000°F, P_{t_1}/P_2 = 1.5

Blowing	$10^2 f$	B	P_{t_1} psia	$\frac{P_1}{P_{t_1}}$	Suction surface x, inches						Pressure surface x, inches				
					.408	.790	1.037	1.241	1.522	2.079	.366	.600	.806	1.032	1.513
					P/P_{t_1}										
-	0.00	0.00	42.38	0.933	.722	.576	0.573	0.573	0.585	0.625	.937	.927	.913	0.902	0.849
S	.52	1.92	42.56	.933	.731	.592	.597	.597	.611	.665	.938	.926	.916	.898	.851
P	.52	1.92	42.59	.933	.721	.571	.571	.568	.582	.625	.937	.930	.916	.899	.850
S+P	1.04	1.92	42.72	.934	.728	.588	.592	.592	.604	.641	.939	.929	.918	.899	.850
S	1.51	5.56	43.03	.935	.739	.614	.623	.623	.634	.653	.934	.925	.913	.892	.846
P	1.51	5.56	43.08	.935	.731	.566	.566	.562	.578	.620	.935	.929	.917	.898	.845
S+P	2.95	5.45	43.55	.935	.735	.608	.615	.615	.629	.652	.935	.928	.909	.893	.840
S	2.44	9.02	43.48	.935	.747	.635	.642	.644	.653	.660	.931	.922	.908	.890	.844
P	2.48	9.17	43.12	.935	.717	.566	.564	.561	.575	.619	.935	.932	.921	.900	.844
S+P	4.94	9.11	44.31	.939	.745	.630	.639	.639	.648	.661	.934	.934	.919	.896	.835
S	3.05	11.25	43.69	.937	.753	.650	.655	.657	.659	.655	.929	.920	.909	.888	.842
P	3.09	11.40	43.26	.937	.714	.564	.564	.560	.576	.620	.939	.929	.922	.897	.846
S+P	6.10	11.26	44.52	.940	.750	.645	.654	.654	.645	.647	.937	.932	.921	.896	.838

Table XI - Static Pressure Data for Model III, T_{t_1} = 1000°F, P_{t_1}/P_2 = 1.7

Blowing	$10^2\xi$	B	P_{t_1} psia	$\frac{P_1}{P_{t_1}}$	Suction surface x, inches						Pressure surface x, inches				
					.408	.790	1.037	1.241	1.522	2.079	.366	.600	.806	1.032	1.513
					P/P_{t_1}										
-	0.00	0.00	41.10	0.906	.693	.530	0.509	0.466	0.443	0.517	.914	.907	.890	0.868	0.816
S	.47	1.72	40.78	.910	.705	.547	.528	.505	.519	.564	.923	.913	.900	.877	.824
P	.45	1.68	40.95	.907	.697	.532	.510	.466	.442	.522	.923	.913	.900	.877	.820
S+P	.97	1.79	40.84	.919	.706	.547	.526	.501	.517	.564	.928	.919	.906	.883	.826
S	1.37	5.05	41.47	.915	.710	.569	.561	.549	.562	.583	.913	.907	.894	.871	.820
P	1.45	5.36	41.09	.923	.699	.534	.512	.467	.443	.526	.929	.920	.906	.887	.824
S+P	2.85	5.26	41.61	.922	.712	.567	.556	.543	.556	.584	.927	.919	.903	.881	.821
S	2.33	8.61	41.64	.921	.725	.599	.594	.588	.594	.599	.924	.912	.899	.877	.825
P	2.32	8.56	41.48	.920	.702	.530	.511	.465	.441	.526	.928	.923	.909	.885	.817
S+P	4.81	8.88	41.60	.925	.738	.608	.601	.596	.600	.613	.947	.942	.930	.904	.834
S	2.95	10.89	41.91	.926	.730	.613	.606	.606	.606	.594	.923	.911	.900	.876	.823
P	2.81	10.38	41.54	.917	.698	.532	.510	.465	.440	.525	.932	.927	.912	.883	.823
S+P	5.91	10.91	42.77	.927	.727	.608	.601	.599	.596	.570	.928	.924	.909	.884	.821

Table XII - Static Pressure Data for Model IV, T_{t_1} = 1000°F, P_{t_1}/P_2 = 1.5

Blowing	$10^2 \xi$	B	P_{t_1} psia	$\frac{P_1}{P_{t_1}}$	Suction surface x, ins.				Pressure surface x, inches					
					0.408	0.570	1.427	2.177	0.366	0.600	0.806	1.043	1.343	1.805
					P/P_{t_1}									
-	0.00	0.00	42.63	0.920	0.723	0.652	0.584	0.647	0.936	0.927	0.916	0.893	0.869	0.798
S	.48	1.77	42.60	.922	.729	-	.595	.658	.937	.928	.916	.893	.868	.799
P	.48	1.87	42.70	.922	.723	.651	.582	.646	.938	.930	.919	.895	.871	.804
S+P	.95	1.76*	43.11	.924	.727	.670	.591	.656	.938	.930	.918	.895	.870	.796
S	1.40	5.16	43.19	.924	.735	.671	.605	.660	.938	.929	.917	.895	.871	.800
P	1.42	5.55	42.96	.926	.721	.649	.578	.640	.941	.935	.918	.897	.876	.787
S+P	2.88	5.32*	43.65	.930	.733	.670	.600	.659	.943	.936	.920	.898	.877	.789
S	2.44	9.00	43.29	.933	.740	.678	.608	.654	.940	.931	.921	898	.873	.806
P	2.43	9.46	43.21	.932	.723	.650	.577	.638	.945	.941	.913	.906	.880	.793
S+P	4.97	9.18*	44.04	.938	.739	.676	.603	.650	.946	.945	.932	.909	.881	.793
S	3.03	11.19	43.38	.935	.741	.679	.607	.648	.942	.932	.921	.899	.876	.809
P	3.03	11.80	43.38	.935	.721	.647	.574	.634	.946	.943	.936	.903	.883	.786
S+P	6.18	11.40*	44.25	.940	.738	.675	.599	.641	.949	.945	.939	.908	.887	.796

*Denotes value for S blowing. Multiply by 1.055 for pressure surface value of B.

Table XIII - Static Pressure Data for Model IV, T_{t_1} = 1000°F, P_{t_1}/P_2 = 1.7

Blowing	$10^2\xi$	B	P_{t_1} psia	$\frac{P_1}{P_{t_1}}$	Suction surface x, ins.				Pressure surface x, inches					
					0.408	0.570	1.427	2.177	0.366	0.600	0.806	1.043	1.343	1.805
					P/P_{t_1}									
-	0.00	0.00	40.22	0.921	0.710	0.631	0.471	0.566	0.935	0.925	0.912	0.885	0.854	0.767
S	.49	1.79	40.36	.917	.707	.631	.476	.584	.929	.917	.903	.878	.849	.763
P	.48	1.86	40.58	.915	.703	.625	.468	.562	.941	.920	.907	.879	.850	.758
S+P	.98	1.81*	40.25	.920	.709	.633	.468	.585	.933	.923	.910	.883	.854	.761
S	1.44	5.33	41.20	.922	.717	.642	.512	.594	.933	.923	.910	.883	.830	.771
P	1.42	5.55	40.22	.918	.751	.627	.471	.561	.936	.930	.910	.879	.859	.753
S+P	2.78	5.13*	41.08	.915	.715	.641	.504	.591	.938	.930	.911	.889	.862	.759
S	2.41	8.88	40.85	.925	.718	.646	.515	.584	.931	.921	.908	.883	.854	.772
P	2.41	9.37	41.14	.925	.706	.627	.474	.557	.939	.933	.922	.894	.861	.758
S+P	4.97	9.17*	41.41	.930	.718	.647	.507	.581	.943	.937	.927	.900	.866	.766
S	3.05	11.25	40.84	.928	.723	.652	.517	.580	.936	.926	.914	.888	.860	.779
P	3.00	11.68	40.94	.929	.708	.629	.474	.557	.947	.943	.935	.897	.873	.752
S+P	6.14	11.33*	42.33	.933	.718	.649	.504	.570	.944	.940	.931	.897	.872	.762

*Denotes value for S blowing. Multiply by 1.055 for pressure surface value of B.

Table XIV - Wake Total Pressure Survey Data for Model I, T_{t_1} = 500°F, P_{t_1}/P_2 = 1.5

Blowing	$10^2 \xi$	B	P_{t_1} psia	$\frac{P_1}{P_{t_1}}$	$\int_{-0.3}^{+0.3} \frac{P_{t_1}-P_{t_2}}{P_{t_1}} dy$ inches	$\left(\frac{P_{t_1}-P_{t_2}}{P_{t_1}}\right)_{max}$	ω
-	0.00	0.0	44.61	0.916	0.0188	0.085	0.0582
S	0.44	1.87	45.00	.916	.0192	.109	.0598
P	0.44	1.87	44.65	.916	.0170	.083	.0590
S+P	0.90	1.91	45.03	.917	.0206	.109	.0646
a	0.91	-	44.83	.918	.0173	.085	.0541
b	1.79	1.89	45.38	.919	.0207	.103	.0649
S	1.29	5.48	45.26	.919	.0322	.165	.1003
P	1.29	5.48	44.99	.918	.0208	.087	.0650
S+P	2.54	5.39	45.86	.919	.0343	.169	.1065
a	2.56	-	45.52	.919	.0164	.085	.0509
b	5.10	5.41	46.80	.923	.0319	.168	.0985
S	2.21	9.39	45.84	.919	.0460	.188	.1429
P	2.23	9.47	45.31	.918	.0223	.102	.0693
S+P	4.42	9.39	46.70	.922	.0461	.186	.1427
a	4.46	-	46.26	.921	.0173	.088	.0541
b	8.77	9.37	48.23	.929	.0417	.178	.1303

a Denotes blowing from test cabin walls only.
b Denotes blowing from test cabin walls and both model surfaces.

Table XV - Wake Total Pressure Survey Data for Model I, T_{t_1} = 1000°F, P_{t_1}/P_2 = 1.5

Blowing	$10^2 \xi$	B	P_{t_1} psia	$\frac{P_1}{P_{t_1}}$	$\int_{-0.3}^{+0.3} \frac{P_{t_1}-P_{t_2}}{P_{t_1}} dy$ inches	$\left(\frac{P_{t_1}-P_{t_2}}{P_{t_1}}\right)_{max}$	ω
-	0.00	0.0	44.65	0.919	0.0196	0.091	0.0616
S	1.30	5.52	45.05	.914	.0308	.147	.0951
P	1.34	5.69	44.67	.918	.0205	.098	.0639
S+P	2.67	5.67	45.32	.919	.0323	.162	.1005
a	2.66	-	45.16	.919	.0200	.090	.0625
b	5.36	5.69	46.25	.923	.0292	.112	.0907
S	2.12	9.00	45.33	.919	.0395	.131	.1227
P	2.13	9.04	45.10	.919	.0231	.099	.0717
S+P	4.23	8.99	46.00	.922	.0390	.172	.1287
a	4.35	-	45.43	.922	.0188	.089	.0593
b	8.70	9.22	47.18	.930	.0393	.175	.1236
S	2.77	11.76	45.17	.926	.0420	.180	.1329
P	2.72	11.55	44.65	.922	.0193	.102	.0605
S+P	5.39	11.43	46.21	.927	.0478	.185	.1503
a	5.62	-	45.52	.932	.0163	.090	.0529
b	10.31	10.97	48.33	.929	.0450	.178	.1402

a Denotes blowing from test cabin walls only.
b Denotes blowing from test cabin walls and both model surfaces.

Table XVI - Wake Total Pressure Survey Data for Model II, T_{t_1} = 500°F, P_{t_1}/P_2 = 1.5

Blowing	$10^2 \xi$	B	P_{t_1} psia	$\frac{P_1}{P_{t_1}}$	$\int_{-0.3}^{+0.3} \frac{P_{t_1}-P_{t_2}}{P_{t_1}} dy$ inches	$\left(\frac{P_{t_1}-P_{t_2}}{P_{t_1}}\right)_{max}$	ω
-	0.0	0.0	44.78	0.905	0.0208	0.089	0.0615
S	1.22	4.27	45.60	.911	.0341	.170	.1018
S+P	2.41	4.21	46.08	.912	.0339	.165	.1015
S	2.09	7.31	46.24	.912	.0445	.142	.1320
P	2.10	7.34	45.64	.910	.0220	.091	.0651
S+P	4.18	7.31	47.02	.914	.0476	.200	.1408

Table XVII - Wake Total Pressure Survey Data for Model II, T_{t_1} = 1000°F, P_{t_1}/P_2 = 1.5

Blowing	$10^2 \bar{E}$	B	P_{t_1} psia	$\frac{P_1}{P_{t1}}$	$\int_{-0.3}^{+0.3} \frac{P_{t_1}-P_{t_2}}{P_{t_1}} dy$ inches	$\left(\frac{P_{t_1}-P_{t_2}}{P_{t_1}}\right)_{max}$	ω
-	0.00	0.00	44.34	0.909	0.0205	0.093	0.0610
S	0.43	1.50	44.68	.909	.0216	.114	.0653
P	0.43	1.51	44.54	.910	.0202	.080	.0607
S+P	0.88	1.53	44.68	.900	.0224	.063	.0681
S	1.28	4.48	45.12	.919	.0319	.159	.0982
P	1.24	4.34	44.77	.910	.0219	.095	.0654
S+P	2.49	4.35	45.41	.914	.0318	.157	.0964
S	2.01	7.03	45.57	.911	.0400	.188	.1227
P	2.04	7.14	45.10	.912	.0216	.090	.0645
S+P	4.07	7.12	46.16	.919	.0397	.182	.1192

Table XVIII - Wake Total Pressure Survey Data for Model II, T_{t_1} = 500°F, P_{t_1}/P_2 = 1.7

Blowing	$10^2 \xi$	B	P_{t_1} psia	$\frac{P_1}{P_{t_1}}$	$\frac{P_{t_1}-P_{t_{2dy}}}{P_{t_1}}$ (+0.3 / -0.3) inches	$\left(\frac{P_{t_1}-P_{t_2}}{P_{t_1}}\right)_{max}$	ω
-	0.00	0.00	42.85	0.901	0.0280	0.119	0.0635
S	.43	1.51	42.83	.911	.0315	.153	.0797
P	.43	1.52	42.46	.901	.0283	.115	.0661
S+P	.87	1.52	42.60	.902	.0308	.148	.0735
S	1.26	4.41	42.98	.904	.0432	.212	.1046
P	1.27	4.45	42.55	.905	.0285	.115	.0667
S+P	2.56	4.48	43.26	.909	.0429	.208	.1041
S	2.21	7.73	43.47	.908	.0565	.293	.1368
P	2.20	7.70	42.85	.907	.0262	.198	.0595
S+P	4.42	7.73	44.21	.911	.0558	.245	.1348

Table XIX - Wake Total Pressure Survey Data for Model II, T_{t_1} = 1000°F, P_{t_1}/P_2 = 1.7

Blowing	$10^2\xi$	B	P_{t_1} psia	$\frac{P_1}{P_{t_1}}$	$\int_{-0.3}^{+0.3} \frac{P_{t_1}-P_{t_2}}{P_{t_1}} dy$ inches	$\left(\frac{P_{t_1}-P_{t_2}}{P_{t_1}}\right)_{max}$	ω
-	0.00	0.00	41.96	0.907	0.0221	0.111	0.0520
S	.44	1.55	42.12	.906	.0270	.143	.0657
P	.44	1.55	42.21	.904	.0251	.112	.0593
S+P	.89	1.55	43.32	.905	.0267	.140	.0648
S	1.28	4.48	42.71	.906	.0395	.200	.0968
P	1.27	4.46	42.88	.905	.0230	.108	.0541
S+P	2.53	4.42	43.39	.908	.0411	.193	.0972
S	2.11	7.39	43.46	.909	.0471	.145	.1160
P	2.12	7.42	43.10	.908	.0256	.113	.0604
S+P	4.20	7.35	44.17	.912	.0507	.225	.1246

Table XX - Wake Total Pressure Survey Data for Model III, T_{t_1} = 500°F, P_{t_1}/P_2 = 1.5

Blowing	$10^2 \xi$	B	P_{t_1} psia	$\frac{P_1}{P_{t_1}}$	$\int_{-0.3}^{+0.3} \frac{P_{t_1}-P_{t_2}}{P_{t_1}} dy$ inches	$\left(\frac{P_{t_1}-P_{t_2}}{P_{t_1}}\right)_{max}$	ω
-	0.00.	0.00	41.08	0.924	0.0203	0.088	0.0588
S	.42	1.55	43.06	.926	.0228	.110	.0669
P	.47	1.72	42.82	.926	.0200	.087	.0585
S+P	.91	1.69	43.08	.928	.0220	.112	.0649
S	1.44	5.33	43.42	.931	.0320	.168	.0938
P	1.44	5.32	43.12	.930	.0229	.100	.0662
S+P	2.89	5.34	43.90	.932	.0360	.182	.1068
S	2.37	8.77	43.80	.932	.0348	.173	.1018
P	2.36	8.71	43.50	.930	.0224	.093	.0649
S+P	4.73	8.73	45.00	.935	.0366	.175	.1070

Table XXI - Wake Total Pressure Survey Data for Model III, T_{t_1} = 1000°F, P_{t_1}/P_2 = 1.5

Blowing	$10^2 \xi$	B	P_{t_1} psia	$\frac{P_1}{P_{t_1}}$	$\int_{-0.3}^{+0.3} \frac{P_{t_1}-P_{t_2}}{P_{t_1}} dy$ inches	$\left(\frac{P_{t_1}-P_{t_2}}{P_{t_1}}\right)_{max}$	ω
-	0.00	0.00	42.38	0.933	0.0185	0.088	0.0541
S	.52	1.92	42.56	.933	.0207	.113	.0614
P	.52	1.92	42.59	.933	.0180	.088	.0525
S+P	1.04	1.92	42.72	.934	.0216	.113	.0639
S	1.51	5.56	43.03	.935	.0300	.158	.0858
P	1.51	5.56	43.08	.935	.0212	.099	.0614
S+P	2.95	5.45	43.55	.935	.0317	.173	.0930
S	2.44	9.02	43.48	.935	.0375	.191	.1096
P	2.48	9.17	43.12	.935	.0220	.100	.0636
S+P	4.94	9.11	44.31	.939	.0395	.195	.1152
S	3.05	11.25	43.69	.937	.0348	.175	.1015
P	3.09	11.40	43.26	.937	.0218	.098	.0626
S+P	6.10	11.26	44.52	.940	.0395	.180	.1148

Table XXII - Wake Total Pressure Survey Data for Model III, T_{t_1} = 1000°F, P_{t_1}/P_2 = 1.7

Blowing	$10^2\zeta$	B	P_{t_1} psia	$\frac{P_1}{P_{t_1}}$	$\int_{-0.3}^{+0.3} \frac{P_{t_1}-P_{t_2}}{P_{t_1}} dy$ inches	$\left(\frac{P_{t_1}-P_{t_2}}{P_{t_1}}\right)_{max}$	ω
-	0.00	0.00	41.10	0.906	0.0217	0.100	0.0502
P	.45	1.68	40.95	.907	--	.100	--
S+P	.97	1.79	40.84	.919	.0255	.132	.0619
S	1.37	5.05	41.47	.915	.0325	.182	.0789
S+P	2.85	5.26	41.61	.922	.0330	.189	.0801
S	2.33	8.61	41.64	.921	.0373	.214	.0914
P	2.32	8.56	41.48	.920	--	.108	--
S+P	4.81	8.88	41.60	.925	.0379	.215	.0955
S	2.95	10.89	41.91	.926	.0335	.194	.083[illegible]
P	2.81	10.38	41.54	.917	--	.102	--
S+P	5.91	10.91	42.77	.927	.0379	.205	.0922

Table XXIII - Wake Total Pressure Survey Data for Model IV, T_{t_1} = 500°F, P_{t_1}/P_2 = 1.5

Blowing	$10^2 \bar{f}$	B	P_{t_1} psia	$\frac{P_1}{P_{t_1}}$	$\int_{-0.3}^{+0.3} \frac{P_{t_1}-P_{t_2}}{P_{t_1}} dy$ inches	$\left(\frac{P_{t_1}-P_{t_2}}{P_{t_1}}\right)_{max}$	ω
-	0.00	0.00	42.44	0.935	0.0193	0.091	0.0573
S	.52	1.92	42.45	.932	.0203	.119	.0602
P	.53	2.05	42.14	.933	.0205	.095	.0608
S+P	1.04	1.92*	42.99	.934	.0240	.120	.0712
S	2.45	9.04	43.42	.935	.0225	.117	.0669
P	2.49	9.67	43.53	.938	.0213	.088	.0632
S+P	4.95	9.14*	44.20	.940	.0240	.117	.0712

*Denotes value for S blowing. Multiply by 1.055 for pressure surface value of B.

Table XXIV - Wake Total Pressure Survey Data for Model IV, T_{t_1} = 1000°F, P_{t_1}/P_2 = 1.5

Blowing	$10^2 \xi$	B	P_{t_1} psia	$\frac{P_1}{P_{t_1}}$	$\int_{-0.3}^{+0.3} \frac{P_{t_1}-P_{t_2}}{P_{t_1}} dy$ inches	$\left(\frac{P_{t_1}-P_{t_2}}{P_{t_1}}\right)_{max}$	ω
-	0.00	0.00	42.63	0.920	0.0213	0.100	0.0628
S	.48	1.77	42.60	.922	.0249	.125	.0741
P	.48	1.87	42.70	.922	.0228	.100	.0673
S+P	.95	1.76*	43.11	.924	.0255	.125	.0757
S	1.40	5.16	43.19	.924	.0266	.139	.0796
P	1.42	5.55	42.96	.926	.0237	.102	.0651
S+P	2.88	5.32*	43.65	.930	.0280	.143	.0836
S	2.44	9.00	43.29	.933	.0249	.132	.0752
P	2.43	9.46	43.21	.932	.0217	.096	.0638
S+P	4.97	9.18*	44.04	.938	.0278	.135	.0837
S	3.03	11.19	43.38	.935	.0258	.125	.0796
P	3.03	11.80	43.38	.935	.0219	.093	.0640
S+P	6.18	11.40*	44.25	.940	.0255	.124	.0766

*Denotes value for S blowing. Multiply by 1.055 for pressure surface value of B.

Table XXV - Wake Total Pressure Survey Data for Model IV, $T_{t_1} \approx 1000°F$, $P_{t_1}/P_2 = 1.7$

Blowing	$10^2 \xi$	B	P_{t_1} psia	$\frac{P_1}{P_{t_1}}$	$\int_{-0.3}^{+0.3} \frac{P_{t_1}-P_{t_2}}{P_{t_1}} dy$ inches	$(\frac{P_{t_1}-P_{t_2}}{P_{t_1}})_{max}$	ω
-	0.00	0.00	40.22	0.921	0.0212	0.112	0.0506
S	.49	1.79	40.36	.917	.0256	.146	.0617
P	.48	1.86	40.58	.915	.0225	.110	.0529
S+P	.98	1.81*	40.25	.920	.0255	.143	.0614
S	1.44	5.33	41.20	.922	.0288	.162	.0709
P	1.42	5.55	40.22	.918	.0249	.118	.0590
S+P	2.78	5.13*	41.08	.915	.0309	.170	.0761
S	2.41	8.88	40.85	.925	.0277	.155	.0686
P	2.41	9.37	41.14	.925	.0260	.118	.0613
S+P	4.97	9.17*	41.41	.930	.0310	.165	.0767
S	3.05	11.25	40.84	.928	.0272	.147	.0682
P	3.00	11.68	40.94	.929	.0265	.117	.0631
S+P	6.14	11.33*	42.33	.933	.0305	.151	.0755

*Denotes value for S blowing. Multiply by 1.055 for pressure surface value of B.

Table XXVI - Temperature Data for Model I, T_{t_1} = 500°F, P_{t_1}/P_2 = 1.5

Blowing	$10^2 f$	B	P_{t_1} psia	$\frac{P_1}{P_{t_1}}$	Distance from leading edge along camber line, inches						
					0.298	0.638	0.867	1.066	1.330	1.600	1.886
					T, °F						
-	0.00	0.0	44.61	0.916	480	475	475	475	475	468	460
S	0.44	1.87	45.00	.916	468	443	422	408	402	395	398
P	0.44	1.87	44.65	.916	462	438	415	410	413	402	403
S+P	0.90	1.91	45.08	.917	455	413	365	346	345	338	345
a	0.91	-	44.83	.918	470	465	465	465	465	458	450
b	1.79	1.89	45.38	.919	452	411	362	342	340	334	341
S	1.29	5.48	45.26	.919	451	410	366	342	336	334	342
P	1.29	5.48	44.99	.918	446	405	362	358	366	352	347
S+P	2.54	5.39	45.86	.919	436	365	289	265	272	268	274
a	2.56	-	45.52	.919	471	468	468	468	468	458	449
b	5.10	5.41	46.80	.923	437	365	290	266	273	270	275
S	2.21	9.39	45.84	.919	452	400	345	318	312	312	319
P	2.23	9.47	45.31	.918	452	390	332	330	395	325	318
S+P	4.42	9.39	46.70	.922	431	341	252	233	242	240	241
a	4.46	-	46.26	.921	472	470	469	469	469	460	449
b	8.77	9.37	48.23	.929	432	342	252	232	248	242	246

a Denotes blowing from test cabin walls only.
b Denotes blowing from test cabin walls and both model surfaces.

Table XXVII - Temperature Data for Model I, T_{t_1} = 1000°F, P_{t_1}/P_2 = 1.5

Blowing	$10^2 f$	B	P_{t_1} psia	$\frac{P_1}{P_{t_1}}$	Distance from leading edge along camber line, inches						
					0.298	0.638	0.867	1.066	1.330	1.600	1.886
					T, °F						
-	0.00	0.0	44.65	0.919	955	945	942	948	952	935	916
S	1.30	5.52	45.05	.914	878	792	713	667	652	645	662
P	1.34	5.69	44.67	.918	872	791	712	708	722	695	687
S+P	2.67	5.67	45.32	.919	839	698	560	514	516	505	520
a	2.66	-	45.16	.919	929	920	919	920	922	900	885
b	5.36	5.69	46.25	.923	835	694	555	512	515	502	521
S	2.12	9.00	45.33	.919	860	754	662	609	595	592	612
P	2.13	9.04	45.10	.919	852	748	645	642	665	632	622
S+P	4.23	8.99	46.00	.922	815	652	492	455	465	458	470
a	4.35	-	45.43	.922	925	915	912	915	916	898	878
b	8.70	9.22	47.18	.930	826	651	491	450	465	458	470
S	2.77	11.76	45.17	.926	874	758	652	592	584	580	600
P	2.72	11.55	44.65	.922	846	730	618	616	643	605	590
S+P	5.39	11.43	46.21	.927	810	632	462	421	442	432	435
a	5.62	-	45.52	.932	928	918	918	918	918	898	877
b	10.31	10.97	48.33	.929	809	630	456	420	445	435	440

a Denotes blowing from test cabin walls only.
b Denotes blowing from test cabin walls and both model surfaces.

Table XXVIII - Temperature Data for Model II, T_{t_1} = 500°F, P_{t_1}/P_2 = 1.5

Blowing	$10^2\xi$	B	P_{t1} psia	$\frac{P_1}{P_{t1}}$	Distance from leading edge along camber line, inches				Suction surface x, inches		
					0.292	0.638	0.867	1.066	1.013	1.533	2.093
					T, °F						
-	0.0	0.0	44.78	0.905	492	490	470	491	488	491	490
S	1.22	4.27	45.60	.911	465	330	312	339	300	311	358
S+P	2.41	4.21	46.08	.912	443	242	225	231	248	237	252
S	2.09	7.31	46.24	.912	459	298	272	303	265	265	327
P	2.10	7.34	45.64	.910	451	312	281	274	365	325	310
S+P	4.18	7.31	47.02	.914	435	213	190	193	223	197	212

Table XXIX - Temperature Data for Model II, T_{t_1} = 1000°F, P_{t_1}/P_2 = 1.5

Blowing	$10^2\xi$	B	P_{t_1} psia	$\frac{P_1}{P_{t_1}}$	Distance from leading edge along camber line, inches: 0.292	0.638	0.867	1.066	Suction surface x, inches: 1.013	1.533	2.093
					T, °F						
-	0.00	0.00	44.34	0.909	962	948	908	959	951	956	951
S	0.43	1.50	44.68	.909	927	771	734	798	756	777	756
P	0.43	1.51	44.54	.910	912	777	731	753	827	804	827
S+P	0.88	1.53	44.68	.900	888	639	603	635	665	650	665
S	1.28	4.48	45.12	.919	890	627	602	631	585	592	585
P	1.24	4.34	44.77	.910	883	666	618	622	748	691	748
S+P	2.49	4.35	45.41	.914	842	468	442	442	488	453	488
S	2.01	7.03	45.57	.911	878	570	550	583	525	525	525
P	2.04	7.14	45.10	.912	869	612	562	553	705	630	705
S+P	4.07	7.12	46.16	.919	828	413	377	377	432	382	432

Table XXX - Temperature Data for Model II, T_{t_1} = 500°F, P_{t_1}/P_2 = 1.7

Blowing	$10^2 \xi$	B	P_{t1} psia	$\frac{P_1}{P_{t_1}}$	Distance from leading edge along camber line, inches: 0.292	0.638	0.867	1.066	Suction surface x, inches: 1.013	1.533	2.093
					T, °F						
-	0.00	0.00	42.85	0.901	492	481	470	483	483	483	482
S	.43	1.51	42.83	.911	483	380	370	379	371	380	414
P	.43	1.52	42.46	.901	468	393	380	382	420	401	403
S+P	.87	1.52	42.60	.902	459	313	305	308	325	320	345
S	1.26	4.41	42.98	.904	455	305	305	311	285	302	347
P	1.27	4.45	42.55	.905	451	331	311	311	376	341	335
S+P	2.56	4.48	43.26	.909	435	228	221	221	239	224	241
S	2.21	7.73	43.47	.908	453	275	278	285	257	267	321
P	2.20	7.70	42.85	.907	445	308	285	273	359	312	300
S+P	4.42	7.73	44.21	.911	430	195	185	182	219	188	195

Table XXXI - Temperature Data for Model II, T_{t_1} = 1000°F, P_{t_1}/P_2 = 1.7

Blowing	$10^2\mathcal{F}$	B	P_{t_1} psia	$\frac{P_1}{P_{t_1}}$	Distance from leading edge along camber line, inches				Suction surface x, inches		
					0.292	0.638	0.867	1.066	1.013	1.533	2.093
					T, °F						
-	0.00	0.00	41.96	0.907	969	940	912	950	950	950	951
S	.44	1.55	42.12	.906	928	745	721	770	745	770	821
P	.44	1.55	42.21	.904	920	758	735	743	805	782	810
S+P	.89	1.55	43.32	.905	882	613	594	610	647	635	691
S	1.28	4.48	42.71	.906	890	599	600	615	572	586	681
P	1.27	4.46	42.88	.905	877	645	610	610	723	668	662
S+P	2.53	4.42	43.39	.908	838	443	435	432	437	438	482
S	2.11	7.39	43.46	.909	875	539	547	559	512	517	618
P	2.12	7.42	43.10	.908	865	595	553	541	685	605	592
S+P	4.20	7.35	44.17	.912	821	389	371	365	415	361	388

Table XXXII - Temperature Data for Model III, $T_{t_1} = 500°F$, $P_{t_1}/P_2 = 1.5$

Blowing	$10^2\xi$	B	P_{t_1} psia	$\frac{P_1}{P_{t_1}}$	Distance from leading edge along camber line, inches			Suction surface x, inches		
					0.292	0.867	1.066	1.013	1.533	2.093
					T, °F					
-	0.00	0.00	41.08	0.924	479	478	477	475	479	475
S	.42	1.55	43.06	.926	465	411	388	389	386	411
P	.47	1.72	42.82	.926	459	405	401	412	405	405
S+P	.91	1.69	43.08	.928	448	348	318	331	319	340
S	1.44	5.33	43.42	.931	452	352	315	312	311	349
P	1.44	5.32	43.12	.930	448	351	342	365	346	312
S+P	2.89	5.34	43.90	.932	433	270	230	242	228	227
S	2.37	8.77	43.80	.932	446	312	261	260	262	328
P	2.36	8.71	43.50	.930	440	318	312	336	314	262
S+P	4.73	8.73	45.00	.935	424	225	178	191	178	198

Table XXXIII - Temperature Data for Model III, T_{t_1} = 1000°F, P_{t_1}/P_2 = 1.5

Blowing	$10^2 F$	B	P_{t_1} psia	$\frac{P_1}{P_{t_1}}$	Distance from leading edge along camber line, inches: 0.292	0.867	1.066	Suction surface x, inches: 1.013	1.533	2.093
					T, °F					
-	0.00	0.00	42.38	0.933	962	956	955	953	959	950
S	.52	1.92	42.56	.933	929	820	778	782	765	812
P	.52	1.92	42.59	.933	918	799	787	811	805	811
S+P	1.04	1.92	42.72	.934	893	699	652	678	645	698
S	1.51	5.56	43.03	.935	897	692	619	618	600	682
P	1.51	5.56	43.08	.935	885	682	660	696	676	630
S+P	2.95	5.45	43.55	.935	852	531	451	479	441	451
S	2.44	9.02	43.48	.935	880	630	540	538	529	620
P	2.48	9.17	43.12	.935	818	612	590	635	611	546
S+P	4.94	9.11	44.31	.939	835	452	370	400	367	368
S	3.05	11.25	43.69	.937	878	600	487	490	480	610
P	3.09	11.40	43.26	.937	868	594	573	620	590	512
S+P	6.10	11.26	44.52	.940	830	430	331	364	332	360

Table XXXIV - Temperature Data for Model III, $T_{t_1} = 1000°F$, $P_{t_1}/P_2 = 1.7$

Blowing	$10^2\xi$	B	P_{t_1} psia	$\frac{P_1}{P_{t_1}}$	Distance from leading edge along camber line, inches			Suction surface x, inches		
					0.292	0.867	1.066	1.013	1.533	2.093
					T, °F					
-	0.00	0.00	41.10	0.906	968	958	949	949	943	943
S	.47	1.72	40.78	.910	932	818	772	779	759	810
P	.45	1.68	40.95	.907	921	792	754	783	743	803
S+P	.97	1.79	40.84	.919	894	691	648	678	642	688
S	1.37	5.05	41.47	.915	895	694	617	614	599	680
P	1.45	5.36	41.09	.923	890	676	619	668	602	635
S+P	2.85	5.26	41.61	.922	857	532	459	490	448	454
S	2.33	8.61	41.64	.921	885	529	521	523	512	622
P	2.32	8.56	41.48	.920	872	610	552	605	542	533
S+P	4.81	8.88	41.60	.925	838	450	355	395	352	362
S	2.95	10.89	41.91	.926	875	597	478	480	471	611
P	2.81	10.38	41.54	.917	865	588	530	584	522	494
S+P	5.91	10.91	42.77	.927	824	320	318	358	317	342

Table XXXV - Temperature Data for Model IV, $T_{t_1} = 500°F$, $P_{t_1}/P_2 = 1.5$

Blowing	$10^2 F$	B	P_{t_1} psia	$\frac{P_1}{P_{t_1}}$	Distance from leading edge along camber line, inches					Suction surface x, inches	
					0.292	0.775	0.850[b]	1.100[b]	1.962	1.427	2.093
					T, °F						
-	0.00	0.00	42.44	0.935	485	480	479	482	479	482	476
S	.52	1.92	42.45	.932	468	396	406	394	422	388	409
P	.53	2.05	42.14	.933	469	419	404	405	429	418	412
S+P	1.04	1.92[a]	42.99	.934	452	342	333	323	378	324	349
S	2.45	9.04	43.48	.935	431	263	295	270	370	260	348
P	2.49	9.67	43.53	.938	442	330	283	301	324	330	302
S+P	4.95	9.14[a]	44.20	.940	415	282	285	293	209	287	234

a Denotes value for S blowing. Multiply by 1.055 for pressure surface value of B.
b Offset from camber line to 0.040 inch from pressure surface.

Table XXXVI - Temperature Data for Model IV, $T_{t_1} = 1000^{\circ}F$, $P_{t_1}/P_2 = 1.5$

Blowing	$10^2\xi$	B	P_{t_1} psia	$\frac{P_1}{P_{t_1}}$	Distance from leading edge along camber line, inches					Suction surface x, inches	
					0.292	0.775	0.850[b]	1.100[b]	1.962	1.427	2.093
					T, $^{\circ}F$						
-	0.00	0.00	42.63	0.920	960	950	953	958	952	959	948
S	.48	1.77	42.60	.922	904	764	782	770	734	762	817
P	.48	1.87	42.70	.922	912	818	793	802	848	828	822
S+P	.95	1.76[a]	43.11	.924	871	661	653	644	743	653	704
S	1.40	5.16	43.19	.924	859	606	641	602	719	581	692
P	1.42	5.55	42.96	.926	825	704	651	660	708	702	658
S+P	2.88	5.32[a]	43.65	.930	824	479	465	438	550	443	493
S	2.44	9.00	43.29	.933	842	532	579	533	704	518	668
P	2.43	9.46	43.21	.932	866	642	570	590	650	643	584
S+P	4.97	9.18[a]	44.04	.938	800	400	384	362	501	379	435
S	3.03	11.19	43.38	.935	840	518	565	516	710	503	670
P	3.03	11.80	43.38	.935	858	617	542	564	610	620	568
S+P	6.18	11.40[a]	44.25	.940	790	373	360	341	486	361	438

a Denotes value for S blowing. Multiply by 1.055 for pressure surface value of B.
b Offset from camber line to 0.040 inch from pressure surface.

Table XXXVII - Temperature Data for Model IV, T_{t_1} = 1000°F, P_{t_1}/P_2 = 1.7

Blowing	$10^2 \xi$	B	P_{t1} psia	$\frac{P_1}{P_{t1}}$	Distance from leading edge along camber line, inches: 0.292	0.775	0.850[b]	1.100[b]	1.962	Suction surface x, inches: 1.427	2.093
					T, °F						
-	0.00	0.00	40.22	0.921	964	958	954	952	946	950	935
S	.49	1.79	40.36	.917	905	761	781	764	825	754	801
P	.48	1.86	40.58	.915	920	821	793	780	841	793	800
S+P	.98	1.81[a]	40.25	.920	874	659	651	638	731	642	681
S	1.44	5.33	41.20	.922	864	606	642	600	709	577	681
P	1.42	5.55	40.22	.918	883	708	652	634	707	661	640
S+P	2.78	5.13[a]	41.08	.915	821	472	463	430	534	434	470
S	2.41	8.88	40.85	.925	841	535	581	530	686	512	651
P	2.41	9.37	41.14	.925	863	638	565	555	638	590	570
S+P	4.97	9.17[a]	41.41	.930	776	400	384	358	488	369	426
S	3.05	11.25	40.84	.928	831	502	556	507	690	491	663
P	3.00	11.68	40.94	.929	853	608	528	529	612	569	544
S+P	6.14	11.33[a]	42.33	.933	782	356	[illegible]2	328	480	344	421

a Denotes value for S blowing. Multiply by 1.055 for pressure surface value of B.
b Offset from camber line to 0.040 inch from pressure surface.

Table XXXVIII - Heat Transfer Data for Pressure Surface, $P_{t_1}/P_2 = 1.5$

P_{t1} psia	P_1/P_{t1}	T_{t_1} °F	x inches	$10^{-6}Re_x$	T_w °F	T_{aw} °F	h BTU/ft²-sec-°F	C_H
33.9	0.925	200	0.82	0.248	107	189	0.0274	0.00219
			1.05	.363	109	195	.0295	.00209
			1.31	.519	111	196	.0275	.00170
			1.65	.742	110	196	.0235	.00130
36.0	.926	400	0.82	.191	-	377	-	-
			1.05	.280	155	380	.0286	.00212
			1.31	.396	161	390	.0243	.00161
			1.65	.576	155	395	.0265	.00153
29.0	.924	400	0.82	.154	155	382	.0210	.00221
			1.05	.226	153	384	.0225	.00207
			1.31	.319	153	393	.0211	.00173
			1.65	.464	149	399	.0229	.00165
25.1	.925	400	0.82	.133	154	379	.0187	.00227
			1.05	.196	152	382	.0195	.00208
			1.31	.276	157	391	.0166	.00157
			1.65	.402	149	406	.0199	.00165
23.5	.927	400	0.82	.125	159	382	.0181	.00234
			1.05	.183	157	385	.0199	.00227
			1.31	.259	157	394	.0167	.00169
			1.65	.376	153	399	.0193	.00171

Table XXXIX - Heat Transfer Data for Suction Surface, $P_{t_1}/P_2 = 1.5$

P_{t1} psia	P_1/P_{t1}	T_{t1} °F	x inches	$10^{-6}R_{ex}$	T_w °F	T_{aw} °F	h BTU/ft²-sec-°F	C_H
43.2	0.902	200	0.89	0.744	132	196	0.0468	0.00150
			1.22	1.018	132	194	.0446	.00144
			1.55	1.282	134	195	.0333	.00107
			1.88	1.526	135	197	.0337	.00110
37.0	.899	200	0.89	.637	132	197	.0372	.00139
			1.22	.872	131	194	.0448	.00169
			1.55	1.098	132	195	.0285	.00107
			1.88	1.307	133	199	.0288	.00110
30.3	.897	200	0.89	.522	130	203	.0335	.00153
			1.22	.714	128	201	.0391	.00179
			1.55	.899	129	203	.0294	.00135
			1.88	1.070	130	206	.0270	.00126
30.0	.900	300	0.89	.434	146	300	.0296	.00147
			1.22	.591	145	300	.0333	.00167
			1.55	.743	148	291	.0272	.00136
			1.88	.895	150	306	.0266	.00134
25.8	.899	300	0.89	.373	149	299	.0228	.00131
			1.22	.508	147	300	.0298	.00173
			1.55	.639	149	291	.0269	.00156
			1.88	.770	150	316	.0237	.00134
32.6	.898	300	0.89	.472	160	300	.0339	.00155
			1.22	.642	160	299	.0333	.00157
			1.55	.807	163	289	.0297	.00137
			1.88	.973	165	305	.0295	.00137

Table XXXIX - (Continued)

P_{t_1} psia	P_1/P_{t_1}	T_{t_1} °F	x inches	$10^{-6}Re_x$	T_w °F	T_{aw} °F	h BTU/ft²-sec-°F	C_H
38.8	.901	300	0.89	.561	190	304	.0388	.00149
			1.22	.764	186	302	.0308	.00119
			1.55	.961	186	291	.0317	.00123
			1.88	1.157	-	306	-	-
38.5	.901	400	0.89	.480	222	397	.0412	.00169
			1.22	.652	222	396	.0320	.00132
			1.55	.820	221	398	.0274	.00113
			1.88	.985	227	402	.0313	.00130
34.5	.900	400	0.89	.430	230	390	.0377	.00172
			1.22	.584	229	391	.0361	.00166
			1.55	.734	228	398	.0243	.00112
			1.88	.883	230	398	.0300	.00139
43.0	.899	400	0.89	.539	202	390	.0521	.00190
			1.22	.736	202	387	.0486	.00178
			1.55	.921	202	391	.0398	.00147
			1.88	1.100	207	394	.0370	.00138
37.0	.896	400	0.89	.464	215	393	.0433	.00183
			1.22	.634	214	393	.0448	.00191
			1.55	.792	214	396	.0347	.00148
			1.88	.947	216	400	.0327	.00141
33.0	.894	400	0.89	.414	219	396	.0339	.00161
			1.22	.565	220	398	.0368	.00176
			1.55	.707	220	400	.0304	.00146
			1.88	.845	221	395	.0331	.00160

Table XXXIX - (Continued)

P_{t_1} psia	P_1/P_{t_1}	T_{t_1} °F	x inches	$10^{-6}Re_x$	T_w °F	T_{aw} °F	h - BTU / ft²-sec-°F	C_H
29.2	.894	400	0.89	.366	213	392	.0265	.00142
			1.22	.501	212	394	.0338	.00182
			1.55	.626	215	397	.0317	.00172
			1.88	.747	219	402	.0285	.00156
26.4	.895	400	0.89	.331	226	383	.0200	.00119
			1.22	.452	224	386	.0315	.00188
			1.55	.565	224	387	.0281	.00169
			1.88	.675	225	393	.0263	.00160
26.3	.894	400	0.89	.329	229	385	.0192	.00115
			1.22	.451	228	387	.0315	.00188
			1.55	.564	227	390	.0271	.00163
			1.88	.674	227	395	.0266	.00161
24.6	.897	400	0.89	.309	221	386	.0177	.00112
			1.22	.421	221	385	.0302	.00194
			1.55	.526	221	392	.0263	.00170
			1.88	.630	223	399	.0260	.00139
23.4	.901	400	0.89	.293	220	380	.0161	.00108
			1.22	.401	220	378	.0302	.00203
			1.55	.501	220	385	.0244	.00165
			1.88	.598	221	392	.0238	.00163
22.7	.903	400	0.89	.284	229	380	.0135	.00093
			1.22	.389	228	378	.0282	.00196
			1.55	.486	226	385	.0238	.00166
			1.88	.581	227	391	.0240	.00169

Table XXXIX - (Continued)

P_{t_1} psia	P_1/P_{t_1}	T_{t_1} °F	x inches	$10^{-6}Re_x$	T_w °F	T_{aw} °F	h BTU/ft²-sec-°F	C_H
21.0	.911	400	0.89	.263	217	384	.0121	.00090
			1.22	.360	213	382	.0260	.00195
			1.55	.450	213	389	.0211	.00159
			1.88	.537	217	397	.0214	.00163

Table XL - Heat Transfer Data for Pressure Surface, $P_{t_1}/P_2 = 1.7$

P_{t_1} psia	P_1/P_{t_1}	T_{t_1} °F	x inches	$10^{-6}Re_x$	T_w °F	T_{aw} °F	h BTU/ft²-sec-°F	C_H
40.6	0.921	200	0.82	0.321	131	187	0.0324	0.00201
			1.05	.476	131	187	.0383	.00206
			1.31	.663	-	192	-	-
			65	.932	135	193	.0341	.00150
37.1	.920	200	.82	.294	124	193	.0298	.00202
			- 5	.435	123	192	.0373	.00220
			1.3	.608	129	200	.0305	.00161
			1.65	.853	124	202	.0358	.00172
32.7	.918	200	0.82	.259	122	192	.0291	.00224
			1.05	.384	121	191	.0343	.00229
			1.31	.536	127	199	.0340	.00205
			1.65	.752	122	201	.0327	.00178
30.8	.917	400	0.82	.177	145	357	.0267	.00246
			1.05	.261	145	354	.0329	.00265
			1.31	.367	149	374	.0353	.00254
			1.65	.508	140	386	.0321	.00212
26.2	.915	400	0.82	.150	163	363	.0273	.00296
			1.05	.222	159	359	.0290	.00274
			1.31	.312	162	380	.0299	.00253
			1.65	.432	153	392	.0322	.00250
24.4	.918	400	0.82	.140	170	365	.0203	.00236
			1.05	.207	168	362	.0272	.00276
			1.31	.290	-	369	-	-
			1.65	.403	162	379	-	-

Table XL - (Continued)

P_{t_1} psia	P_1/P_{t_1}	T_{t_1} °F	x inches	$10^{-6}Re_x$	T_w °F	T_{aw} °F	h BTU / ft²-sec-°F	C_H
23.2	.919	400	0.82	.133	166	359	.0219	.00268
			1.05	.197	163	357	.0249	.00265
			1.31	.276	-	369	-	-
			1.65	.383	159	380	-	-

Table XLI - Heat Transfer Data for Suction Surface, $P_{t_1}/P_2 = 1.7$

P_{t_1} psia	P_1/P_{t_1}	T_{t_1} °F	x inches	$10^{-6}Re_x$	T_w °F	T_{aw} °F	h BTU/ft²-sec-°F	C_H
41.4	0.899	200	0.89	0.731	138	195	0.0439	0.00146
			1.22	1.018	137	190	.0425	.00142
			1.55	1.308	138	191	.0407	.00137
			1.88	1.560	139	195	.0340	.00113
35.2	.895	200	0.89	.622	134	205	.0371	.00145
			1.22	.860	133	199	.0393	.00156
			1.55	1.112	134	200	.0374	.00147
			1.88	1.326	136	205	.0334	.00131
29.8	.895	200	0.89	.526	129	205	.0327	.00148
			1.22	.733	127	201	.0323	.00150
			1.55	.942	130	203	.0293	.00136
			1.88	1.123	131	207	.0286	.00132
26.3	.895	250	0.89	.424	130	255	.0249	.00136
			1.22	.593	139	252	.0259	.00141
			1.55	.763	131	253	.0260	.00142
			1.88	.908	132	256	.0263	.00143
24.2	.898	250	0.89	.390	132	255	.0208	.00123
			1.22	.546	130	253	.0203	.00120
			1.55	.702	132	254	.0225	.00133
			1.83	.836	134	256	.0242	.00143
29.5	.894	250	0.89	.475	139	256	.0310	.00151
			1.22	.665	138	252	-	-
			1.55	.856	141	252	.0266	.00129
			1.88	1.019	143	256	.0285	.00138

Table XLI - (Continued)

P_{t_1} psia	P_1/P_{t_1}	T_{t_1} °F	x inches	$10^{-6}Re_x$	T_w °F	T_{aw} °F	h BTU / ft²-sec-°F	C_H
41.0	.901	250	0.89	.660	161	253	.0436	.00153
			1.22	.924	161	248	-	-
			1.55	1.190	162	247	.0309	.00108
			1.88	1.416	164	254	.0325	.00114
40.2	.901	250	0.89	.647	167	255	.0397	.00142
			1.22	.906	166	251	-	-
			1.55	1.167	167	250	.0293	.00105
			1.88	1.389	168	256	.0315	.00112
24.8	.900	400	0.89	.317	178	392	.0099	.00063
			1.22	.443	178	393	.0263	.00167
			1.55	.569	179	382	.0233	.00148
			1.88	.674	179	406	.0236	.00151
28.6	.898	400	0.89	.365	183	382	.0174	.00096
			1.22	.511	181	375	.0317	.00174
			1.55	.657	185	382	.0241	.00133
			1.88	.777	186	389	.0261	.00144
32.8	.897	400	0.89	.419	202	390	.0263	.00126
			1.22	.586	200	379	.0327	.00157
			1.55	.753	204	382	.0281	.00135
			1.88	.891	208	392	.0300	.00145
37.1	.900	400	0.89	.474	216	389	.0332	.00141
			1.22	.662	215	379	.0341	.00144
			1.55	.852	218	382	.0288	.00122
			1.88	1.008	221	388	.0308	.00131

APPENDIX D

SUMMARY OF SCHLIEREN DATA

The Schlieren investigation of Shaw[20] shows clearly the enlarged turbulent boundary layer over the suction surface which was found to be characteristic of massive non-chordwise S blowing. Similar results were obtained for Models I and II (12° spanwise and vertical injection, respectively), although transition during blowing appeared to occur further forward on the suction surface for Model II than for Model I. This is not surprising, since Model II possessed a greater number of holes per row and would be expected to cause a greater disturbance of the laminar boundary layer during equivalent rates of blowing than would Model I. The photographs for Model I show evidence of considerable spanwise variation in the boundary layer during blowing, while those taken of the flow about Model II more closely approximate the two-dimensional situation.

Figures 61 and 62 show the marked contrast between no-blowing and massive suction surface blowing for Model II (vertical injection). Figure 61 shows the boundary layer enlargement for the wholly subsonic suction surface ($P_{t_1}/P_2 = 1.5$) and Fig. 62 shows the similar effect for the transonic suction surface ($P_{t_1}/P_2 = 1.7$). The mottled appearance of the flow in Fig. 61 is due to sound waves travelling upstream from the choked exit nozzle of the facility, while shock waves are clearly visible in the transonic flow field shown in Fig. 62. The location of the blowing rows may be seen from the apparent surface bumps caused by chipping of the quartz glass where coolant feed lines passed through the windows. The region of the first row of holes was completely hidden by a large chip, appearing as a black bulge near the left of each photograph. As may be seen from the photographs for massive blowing, separation does not extend a significant distance upstream, although some local separation may exist upstream of the last blowing row in Fig. 62a. Also of interest is the reduction of Mach number caused by suction surface injection, as seen by the reduction of the number and intensity of the shock waves in Fig. 62a. The first shock wave in this photograph appears to be at the transition point, which was generally found to be in the near vicinity of the first blowing row.

The author is indebted to Mr. R. J. Shaw for his permission to use these photographs in this Appendix.

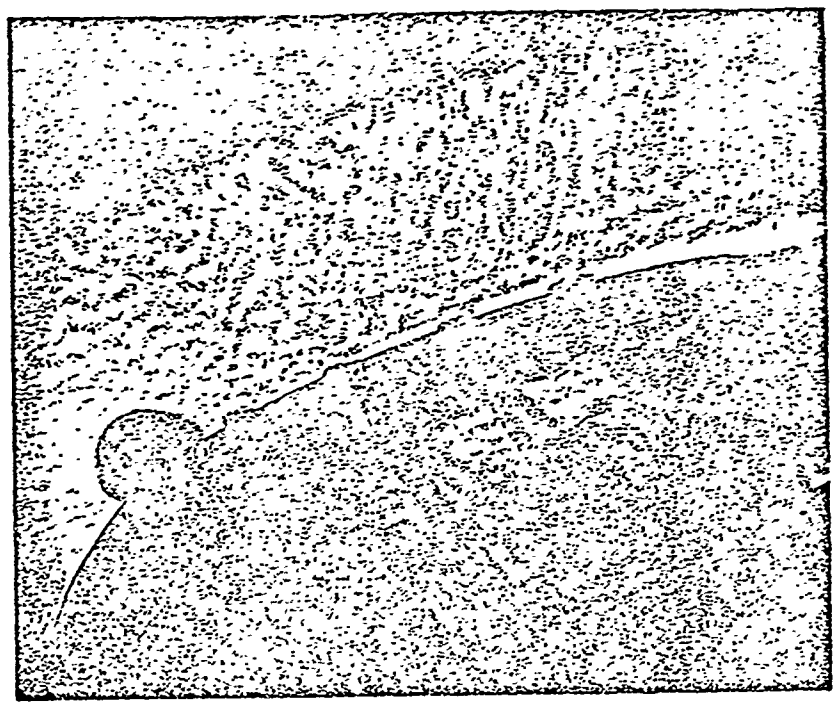

(a) No Blowing

(b) S Blowing, $\xi = 0.013$

Fig. 61 - Schlieren photographs of suction surface flow over Model II (vertical blowing) at $P_{t_1}/P_2 = 1.5$

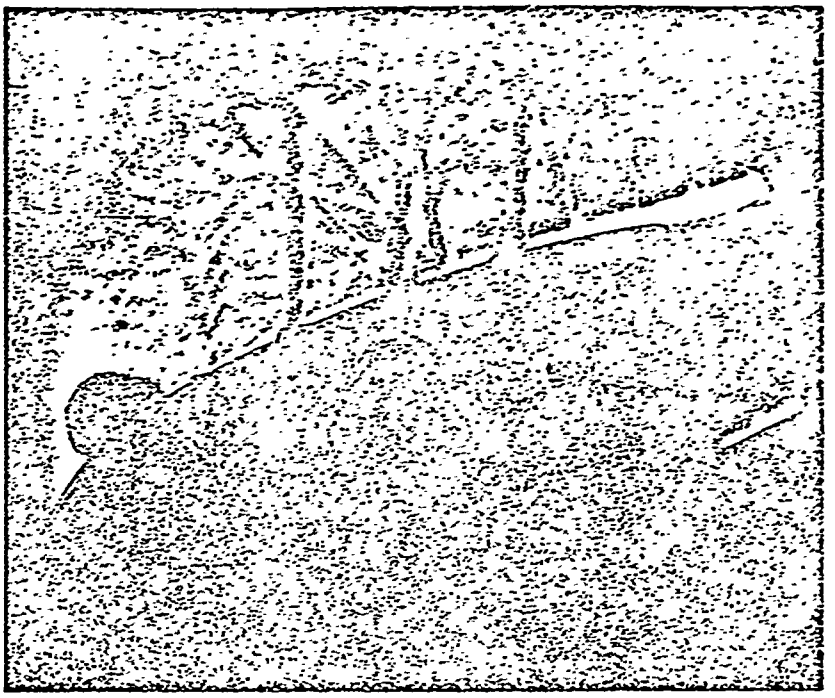

(a) No Blowing

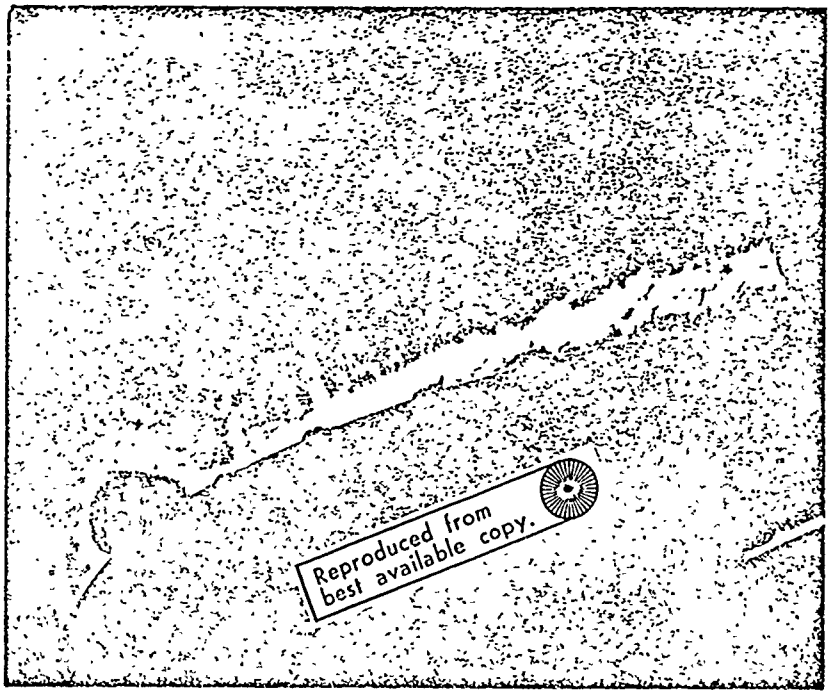

(b) S Blowing, ξ = .010

Fig. 62 - Schlieren photographs of suction surface flow over Model II (vertical blowing) at P_{t_1}/P_2 = 1.7

REFERENCES

1. Eckert, E. R. G., and Livingood, J. N. B., "Comparison of Effectiveness of Convection-Transpiration, and Film Cooling Methods with Air as Coolant," NACA TN-3010, Washington, D.C., (October, 1953).

2. Hatch, J. E., and Papell, S. S., "Use of a Theoretical Flow Model to Correlate Data for Film Cooling or Heating an Adiabatic Wall by Tangential Injection of Gases of Different Fluid Properties," NASA TN-130, Washington, D.C., (November, 1959).

3. Rubesin, M. W., and Inouye, M., "A Theoretical Study of the Effect of Upstream Transpiration Cooling on the Heat Transfer and Skin Friction Characteristics of a Compressible Laminar Boundary Layer, NACA TN-3969, Washington, D.C., (1957).

4. Howe, J. T., "Some Finite Difference Solutions of the Laminar Compressible Boundary Layer Showing the Effect of Upstream Transpiration Cooling," NASA Memorandum 2-26-59A, Washington, D.C., (February, 1959).

5. Weighardt, K., "Hot-Air Discharge for De-Icing," AFF Translation No. F-TS-919-RE, (December, 1945).

6. Papell, S. S., and Trout, A. M., "Experimental Investigation of Air Film Cooling Applied to an Adiabatic Wall by Menas of an Axially Discharging Slot," NASA TN D-9, (1959).

7. Seban, R. A., "Heat Transfer and Effectiveness for a Turbulent Boundary Layer with Tangential Fluid Injection," Journal of Heat Transfer, Trans. ASME, Series C, V 82:4 (November, 1960), 303-312.

8. Hartnett, J. P.; Birkebak, R. C.; and Eckert, E. R. G., "Velocity Distributions, Temperature Distributions, Effectiveness, and Heat Transfer for Air Injected through a Tangential Slot into a Turbulent Boundary Layer," Journal of Heat Transfer, Trans. ASME, Series C, V 83:3, (August, 1961), 293-306.

9. Papell, S. S., "Effect on Gaseous Film Cooling of Coolant Injection through Angled Slots and Normal Holes," NASA TN D-299, Washington, D.C., (September, 1960).

10. Hearing, G. W., "Gas Film Cooling of a Transonic Nozzle," AFAPL-TR-66-40, Air Force Aero Propulsion Laboratory, Wright-Patterson Air Force Aero Propulsion Laboratory, Wright-Patterson Air Force Base, Ohio, (June, 1965).

11. Goldstein, R. J.; Eckert, E. R. G.; and Ramsey, J. W., "Film Cooling with Injection through Holes: Adiabatic Wall Temperatures Downstream of a Circular Hole," Jour. of Engr. for Power, Trans. ASME, Series A, V 90:4, (October, 1968), 384-395.

12. Metzger, D. E., and Fletcher, D. D., "Surface Heat Transfer Immediately Downstream of Flush, Non-Tangential Injection Holes and Slots," AIAA Paper No. 69-523, (June, 1969).

13. Langanelli, A. L., "A Comparison between Film Cooling and Transpiration Cooling Systems in High Speed Flow," AIAA Paper No. 70-153, (January, 1970).

14. Barnes, J. F., and Came, P. M., "Some Aerodynamic Aspects of Turbine Blade Cooling," ASME Paper 69-GT-15, (March, 1969).

15. Provenzale, G. E., and Thirumalaisamy, S. N., "Experimental Investigation of the Effects of Transpiration Cooling on Turbine Stator Blade Aerodynamics," ASME Paper No. 69-GT-39, (March, 1969).

16. Haering, G. M., "A Proposed Correlation Scheme for Gas-Film Cooling Data," AFAPL-TR-66-56, Air Force Aero Propulsion Laboratory, Wright-Patterson AFB, Ohio, (August, 1966).

17. Quick, D. H.; Henderson, R. E.; and Tall, W. A., "Experimental Cold-Flow Investigation of Chordwise Static Pressure Distribution around a Turbine Airfoil," AFAPL-TR-67-147, Air Force Aero Propulsion Laboratory, Wright-Patterson AFB, Ohio, (March, 1968).

18. Bartle, E. R., and Leadon, B. M., "The Effectiveness as a Universal Measure of Mass Transfer Cooling for a Turbulent Boundary Layer," Proc. 1962 Heat Transfer and Fluid Mechanics Institute, (June, 1962), 27-41.

19. Gregorek, G. M., "Viscous Effects of Blunt Cones at Low Reynolds Numbc and Hypersonic Speeds," ARL 69-0006, Aerospace Research Labor, ories, Wright-Patterson AFB, Ohio, (January, 1969).

20 Shaw, R. J., "A Schlieren Study of Airflow over a Film Cooled Turbine Blade," M.Sc. Thesis, The Ohio State University, Columbus, Ohio, (1970).